High frequency magnetic field-induced strain of ferromagnetic shape memory alloys

Shaobin Zhang

université PARIS-SACLAY

NNT : 2018SACLY011

Thèse de doctorat

High Frequency Magnetic Field-induced Strain of Ferromagnetic Shape Memory Alloys

Thèse de doctorat de l'Université Paris-Saclay

préparée à l'Ecole Nationale Supérieure de Techniques Avancées

École doctorale n°579 sciences mécaniques et énergétiques, matériaux et géosciences (SMEMAG)

Spécialité de doctorat : Mécanique des solides

Thèse présentée et soutenue à Palaiseau, le 07 septembre 2018, par

M. Shaobin ZHANG

Composition du Jury :

M. Etienne PATOOR Professeur, Georgia Tech-Lorraine	Président
M. Günay ANLAS Professeur, Boğaziçi University	Rapporteur
M. Mohamed HABOUSSI Professeur, Université Paris 13	Rapporteur
M. Tarak BEN ZINEB Professeur, Université de Lorraine	Examinateur
M. Laurent DANIEL Professeur, CentraleSupelec	Examinateur
M. Olivier HUBERT Professeur, ENS Paris-Saclay	Examinateur
M. Yongjun HE Maître de Conférences (HDR), ENSTA ParisTech	Directeur de thèse
M. Ziad MOUMNI Professeur, ENSTA ParisTech	Co-Directeur de thèse

THÈSE DE DOCTORAT

DE

L'UNIVERSITÉ PARIS-SACLAY

PRÉPARÉE À

L'ECOLE NATIONALE SUPÉRIEURE DE TECHNIQUES AVANCÉES

ÉCOLE DOCTORALE N°579

Sciences mécaniques et énergétiques, matériaux et géosciences (SMEMaG)

Spécialité de doctorat : Mécanique des solides

Par

Shaobin ZHANG

High Frequency Magnetic Field-induced Strain of Ferromagnetic Shape Memory Alloys

Thèse présentée et soutenue à Palaiseau, le 07 septembre 2018;

Composition du Jury :

M. Etienne PATOOR	Professeur, Georgia Tech-Lorraine	Président
M. Günay ANLAS	Professeur, Boğaziçi University	Rapporteur
M. Mohamed HABOUSSI	Professeur, Université Paris 13	Rapporteur
M. Tarak BEN ZINEB	Professeur, Université de Lorraine	Examinateur
M. Laurent DANIEL	Professeur, CentraleSupelec	Examinateur
M. Olivier HUBERT	Professeur, ENS Paris-Saclay	Examinateur
M. Yongjun HE,	Maître de Conférences (HDR), ENSTA ParisTech	Directeur de thèse
M. Ziad MOUMNI,	Professeur, ENSTA ParisTech	Co-Directeur de thèse

Dedicated to my late grandfather

And my beloved family,

Especially to my wife Wenjun BAI.

Acknowledgements

I would like to take this opportunity to sincerely express the gratitude to my supervisors, Dr. Yongjun He and Prof. Ziad Moumni for their guidance through these three years at ENSTA-ParisTech. Yongjun is always willing to spend his precious time discussing my ideas and works. His good tastes, keen senses and critical thinking to the scientific problems help me improve my work a lot. He is generous in sharing his personal research experience which inspire me to constantly exploring the unknown world with persistence. Ziad always concerns my research progress and help me overcome the difficulties. His encouragement and support give me confidence to step forward. Both supervisors have given me a great freedom to pursue the research in my own way, which helps me gain the ability of doing scientific research independently. I am very grateful for I have worked with Yongjun and Ziad.

Many thanks to all my thesis committee members, Prof. Anlas, Prof. Ben Zineb, Prof. Daniel, Prof. Haboussi, Prof. Hubert, Prof. Patoor, for their comments, fruitful discussions and useful suggestions.

I would also like to thank all my colleagues in our lab of Unité de Mécanique (UME). Particularly, Prof. Habibou Maitournam is acknowledged for his help and concern in my work. Lahcène Cherfa, Nicolas Baudet, Oana-Zenaida Pascan, Lin Zheng, Nicolas Thurieau, Quantin Pierron, Thierry Pichon and Alain Van Herpen are appreciated for their kind help on my experimental setup. All the following colleagues, Anne-Lise Gloanec, Fabien Szmytka, Kim Pham, Andres Leon Baldelli, Claude Stolz, Josiane Nguejio Nguimatsia, Xiaojun Gu, Jun Wang, Yinjun Jiang, Yahui Zhang, Marine Bayard

and Masmoudi Moez are also acknowledged for the active research atmosphere.

My intership students, Amine Kirati, Ali Hamieh and Onjatiana Victorain Rakotoarivony from Ecole spéciale militaire de Saint-Cyr, Xianghe Jiang from Ecole Polytechnique, Amine Bettaieb, Marouan Ben Saada, Mourad Jouili and Majed Salhi from Tunisian Military Academy, and Jian Zhang from Polytech Paris-Sud should also be acknowledged for their help and discussions in my experiments.

Thanks to Yongjun, Lin, Xiaojun, Jun, Yinjun and Yahui for our beautiful memories and their delicious dishes, the flavor of hometown. Besides, special acknowledgement to Yahui Zhang, who has been my officemate in UME, schoolmate in Northwestern Polytechnic University (NPU) and classmate in high school. We have been growing up, learning and working together from 15 years old to the present and from Fengxiang (China) to Paris (France). I like to thank Yahui for all the funny and youthful moments and all the supports from him. They will be the most precious and greatest memories in my entire life.

This work was funded by China Scholarship Council (No. 201506280009). I am very appreciative of their financial support.

Finally, I would love to thank my family, my parents, grandparents and elder sisters for their unselfish love and support. As farmers in a developing country, they have sacrificed too much of their own personal lives to accomplish this impossible mission of supporting me to be a Doctor. The most special thanks to my wife Wenjun for her endless love and encouragement. She always gives me confidence to go forward, because I am sure that she will always stay with me for the rest of our life even if I lost the whole world.

Publications

Journals

Zhang, S., Chen, X., Moumni, Z., and He, Y. (2018). Thermal effects on high-frequency magnetic-field-induced martensite reorientation in ferromagnetic shape memory alloys: An experimental and theoretical investigation. ***International Journal of Plasticity***, 108: 1–20.

Zhang, S., Chen, X., Moumni, Z., and He, Y. (2018). Coexistence and compatibility of martensite reorientation and phase transformation in high-frequency magnetic-field-induced deformation of Ni-Mn-Ga single crystal. ***International Journal of Plasticity***, accepted, https://doi.org/10.1016/j.ijplas.2018.06.010

Zhang, S. and He, Y. (2018). Fatigue resistance of branching phase-transformation fronts in pseudoelastic NiTi polycrystalline strips. ***International Journal of Solids and Structures***, 135: 233–244.

Proceeding

Zhang, S., Moumni, Z., and He, Y. (2018). Thermal effects on dynamic magnetic-field-induced martensite reorientation of single crystal Ni-Mn-Ga. In ***European Solid Mechanics Conference***, Bologna, Italy.

Zhang, S. and He, Y. (2017). Domain interfaces and fatigue failure of NiTi polycrystalline strips. In ***ECCOMAS Thematic Conference on Smart Structures and Materials (SMART 2017)***, Madrid, Spain.

Abstract

Ferromagnetic Shape Memory Alloys (FSMAs) have ability to provide large high-frequency reversible strain via magnetic field-induced martensite reorientation. But, the high-frequency frictional twin boundary motion of the martensite reorientation can induce a rapid accumulation of dissipation heat and cause a significant temperature rise in the material, which poses instability problems about the dynamic performance of FSMA. Particularly, the output strain amplitude would be reduced significantly when the temperature increases to be high enough to trigger the Martensite-Austenite phase transformation. However, such thermal effect on the dynamic responses of FSMA has not yet been investigated in literature where most existing dynamic experiments were performed only for a short-time period (a few seconds) to avoid the temperature variation. In this thesis, multi-scale experimental and theoretical analyses of the long-time performance of FSMA under high-frequency magnetic actuation are performed. Systematic experiments of the long-time magnetic actuation (> 100 seconds) on a Ni-Mn-Ga single crystal bar are conducted at various levels of magnetic field frequency, initial compressive stress and ambient airflow (ambient heat-exchange efficiency) to investigate their influences on the stable state of the high-frequency FSMA-actuator. A one-dimensional heat-transfer model is developed and the new experimental phenomena of the thermal effects are well understood. Based on the experimental results and theoretical analysis, critical conditions to achieve the large and stable output strain amplitude in the high-frequency actuation are derived. Moreover, to understand the heat-

exchange dependence of the output nominal-strain from a microscopic view, the local strain distribution/evolution and the associated transformation/reorientation among the different phases/variants during the high-frequency actuation under various heat-exchange efficiencies are demonstrated via the in-situ Digital Image Correlation observations. A novel mechanism is revealed: the temperature-driven phase boundary motion (phase transformation) and the magnetic field-driven twin boundary motion (martensite reorientation) can be activated at the same time under the magneto-thermal-mechanical actuation (i.e., the high-frequency magnetic field, the mechanical spring force and the varying ambient airflow) as the material can self-organize its volume fractions of the different phases/variants to satisfy all the thermo-magneto-mechanical boundary conditions. Further, the self-organized morphology/pattern composed of various variants and phases during cyclic deformation (with the moving habit plane and twin boundaries) can be explained by microstructure compatibility analyses.

Keywords: Ferromagnetic shape memory alloy, high-frequency strain, magnetic field-induced martensite reorientation, temperature-induced phase transformation, microstructure compatibility, thermo-magneto-mechanical coupling.

Résumé

Les alliages à mémoire de forme ferromagnétique (FSMAs) possèdent la capacité d'accommoder une large déformation réversible à haute fréquence à l'aide d'une réorientation de la martensite induite par un champ magnétique. Cependant, cette réorientation à haute fréquence induit un frottement au niveau des interfaces entre les variantes de martensite provoquant une dissipation et par suite une élévation significative de la température dans le matériau, ce qui pose des problèmes d'instabilité nuisant à la performance du comportement dynamique des FSMAs. En particulier, l'amplitude de la déformation induite par le champ magnétique est réduite de façon significative lorsque l'augmentation de la température est suffisante pour déclencher la transformation de phase martensite-austénite. Un tel effet thermique sur les réponses dynamiques de FSMA n'a pas encore été étudié dans la littérature où la plupart des expériences dynamiques existantes ont été réalisées sur une courte période de temps (quelques secondes) afin d'éviter la variation de la température. Le but de cette thèse est l'analyse et la modélisation de ce phénomène. Pour ce faire, des analyses expérimentales et théoriques multi-échelles des performances des FSMAs soumis à un champ magnétique de longue durée et à haute fréquence sont réalisées. Tout d'abord, des expériences systématiques d'actionnement magnétique de longue durée (> 100 secondes) sur une éprouvette en monocristal Ni-Mn-Ga sont effectuées à différents niveaux de la fréquence du champ magnétique, de la contrainte de compression initiale et du flux d'air ambiant (échange de chaleur) afin d'étudier leur influence sur la réponse des FSMAs. Par

ailleurs, un modèle unidimensionnel de transfert de chaleur a été est développé permettant d'interpréter les nouveaux phénomènes liés aux effets thermiques mises en lumière expérimentalement. Ainsi, les conditions nécessaires à l'obtention d'une réponse dynamique stable ont été déduites. De plus, afin de comprendre la dépendance de la déformation nominale induite par le champ magnétique par rapport aux échanges thermiques à partir d'une analyse microscopique, la distribution/évolution de la déformation locale ainsi que la transformation/réorientation associée parmi les différentes phases/variantes au cours de l'actionnement à haute fréquence sous divers conditions d'échange de chaleur sont analysées via des observations in-situ à l'aide la corrélation d'images numériques (DIC). Un nouveau mécanisme est ainsi révélé : le mouvement des interphases induit par la variation de température (transformation de phase) et le mouvement des variantes de martensite induit par le champ magnétique (réorientation de martensite) peuvent être activés simultanément, sous l'actionnement magnéto-thermique-mécanique (i.e, le champ magnétique à haute fréquence, la force de ressort mécanique et le flux d'air ambiant) dans la mesure où le matériau peut auto-organiser les fractions volumiques des différentes phases/variantes afin de satisfaire toutes les conditions aux limites thermo-magnéto-mécaniques. En outre, la morphologie des bandes de déformations et des différentes phases/variantes auto-organisées est révélée et expliquée à l'échelle microscopique à l'aide des conditions de compatibilité géométrique.

Mots-clés : alliage à mémoire de forme ferromagnétique, déformation à haute fréquence, réorientation de la martensite induite par un champ magnétique, transformation de phase induite par la température, compatibilité de la microstructure, couplage thermo-magnéto-mécanique.

Contents

List of Figures

List of Tables

Chapter 1

Introduction

1.1 Overview of ferromagnetic shape memory alloys

1.1.1 Development of ferromagnetic shape memory alloys

Smart materials, called also active materials, can have one or more properties responding to external fields such as mechanical, thermal, light, magnetic, electric field, et al. Some traditional well-known smart materials, such as piezoelectric material, magnetostrictive material and shape memory alloys (SMAs), have been investigated comprehensively and well integrated into engineering applications. Generally, piezoelectric (e.g., PZT Ceramic) and magnetostrictive materials (e.g., Terfenol-D) can function at high frequencies (> 10 kHz) and has excellent stability. However, their maximum strains are quite small (< 0.2%) which seriously limits their applications. On the contrary, SMAs (e.g., the most popular one, NiTi) have ability to output/afford a large reversible strain (up to 10 %) while the operating frequency is quite limited (< 1 Hz). The high working frequency and the large output strain can not be obtained at the same time until a new

class of smart materials, namely Ferromagnetic Shape Memory Alloys (FSMAs, e.g., Ni_2MnGa), was developed in 1990s (Webster et al., 1984; Martynov and Kokorin, 1992). Since Ullakko et al. first reported a 0.2% Magnetic Field-Induced Strain (MFIS) in 1996 (Ullakko et al., 1996) and Murray et al. extended the MFIS to 6% in 2000 (Murray et al., 2000) in Ni_2MnGa single crystals, FSMAs have attracted great research interest (Karaca et al., 2007, 2009, 2006; Heczko et al., 2002; Henry et al., 2002; Heczko et al., 2013; Straka et al., 2011b; Chmielus et al., 2008; Chulist et al., 2013; Pinneker et al., 2014; Li et al., 2014; James and Wuttig, 1998) as they have potential ability to provide large strain (up to 10%, comparable with that of traditional SMAs) at a high operating frequency (up to 1 kHz), which gives FSMAs great advantages over other kinds of the smart materials.

Nevertheless, it should be noted that up to now the large reversible strain can only be obtained in single crystals of FSMA materials, which are very brittle and quite expensive. These drawbacks pose difficulties for machining and applications of FSMAs, which encourages some researchers to develop polycrystalline FSMAs (Gaitzsch et al., 2007; Chulist et al., 2014; Liu et al., 2015; Huang et al., 2014; Li et al., 2017; Qian et al., 2013). But so far a large reversible strain has not been achieved in polycrystalline FSMAs. Therefore, now the single crystal FSMAs are still the research emphasis for improving its material properties and make it suitable for the various promising applications. In the next section, its crystal structure and properties are introduced in details.

1.1.2 Material properties of FSMA

Magnetic field-induced strain can be achieved in various alloys such as Ni-based (Ni-Mn-Ga, Ni-Mn-Al, Ni-Mn-In, Ni-Mn-Sn, Ni-Mn-Sb, Ni-Fe-Ga) (Lai et al., 2008; Henry et al., 2002; Techapiesancharoenkij et al., 2009; Karaca et al., 2009; Neudert et al., 2012; Sutou et al., 2004), Co-based (Co-Ni, Co-Ni-Al, Co-Ni-Ga) (Morito et al., 2002, 2009, 2010; Oikawa et al., 2001; Wuttig et al., 2001) and Fe-based (Fe-Pd, Fe-Pt, Fe-Mn-Ga) (James and Wuttig, 1998; Sakamoto et al., 2003; Fukuda et al., 2014) alloys. Ni_2MnGa is the most common and commercialized one of them. Ni_2MnGa is a Heusler Type alloy with a cubic austenite (L21) structure at high temperature and an approximately tetragonal martensite structure (3 variants with a short axis c along different directions) at low temperature as shown in Fig. 1.1. It's noted that, in fact, the martensite structure has a slight monoclinic distortion (12 variants), but its deviation to the tetragonal structure is only $\sim 0.37°$ (Chulist et al., 2013), so generally the martensite structure of Ni_2MnGa is approximately viewed as tetragonal for simplification of analysis. As the traditional SMAs (e.g., NiTi), FSMAs can take phase transformation (between martensite and austenite phases) and martensite reorientation (between different martensite variants), as shown in Fig. 1.2, and thus have properties of shape memory effect and pseudoelasticity. Actually, the deformation mechanisms of SMAs and FSMAs are similar, except that the deformations can also be driven in FSMAs by magnetic field, in addition to temperature and stress in the conventional SMAs.

- **Shape memory effect and pseudoelasticity**

  The shape memory effect can be briefly described by the schematic shown in Fig. 1.3. For the FSMA (and SMA) material with initial state of Austenite

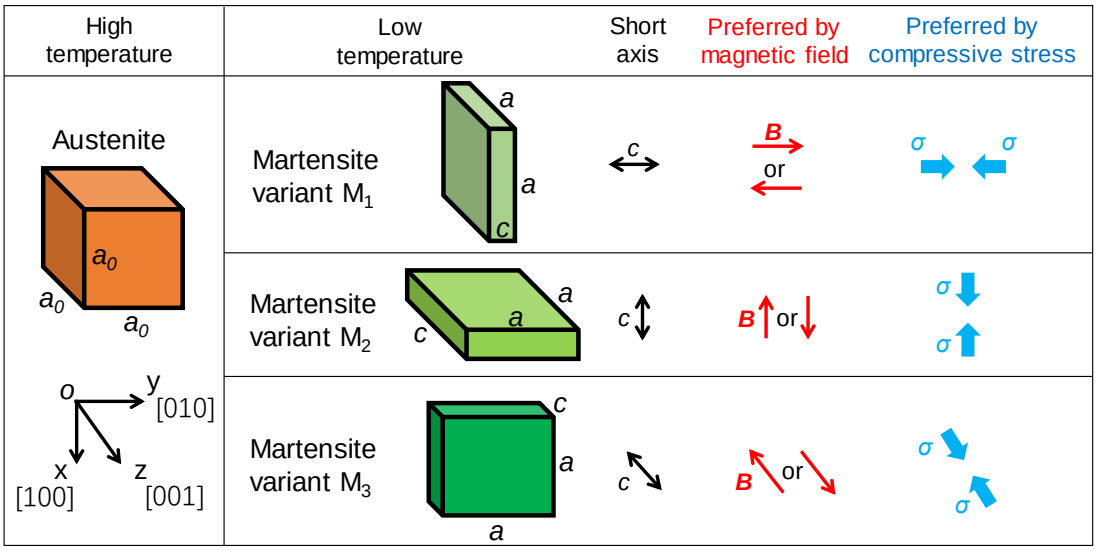

Figure 1.1 Schematic of lattice structures of Ni_2MnGa (the difference between a and c is exaggeratedly shown here) and the energetically preferred directions of the short axis c.

phase (A-phase), the temperature-induced martensite phase transformation occurs upon cooling (below a temperature M_s (Martensite start temperature) and M_f (Martensite finish temperature)), the material transforms to Martensite phase (M-phase) with twinned structure between martensite variants of different orientations (so-called "self-accommodated" structure) without shape change in order to minimize the deformation energy, see the process from (a) to (b) in Fig. 1.3. At this low temperature, when a mechanical load is applied to the twinned martensite structure, the variants with a favorable orientation aligned with the mechanical stress will nucleate and grow by twin boundary motion with expense of other oriented variants, which is the so-called detwinning process by stress-induced martensite reorientation (see the process from (b) to (c) in Fig. 1.3). The detwinning induces a large deformation/strain (shape change) compared to original austenite phase, and this deformation remains after the stress is released

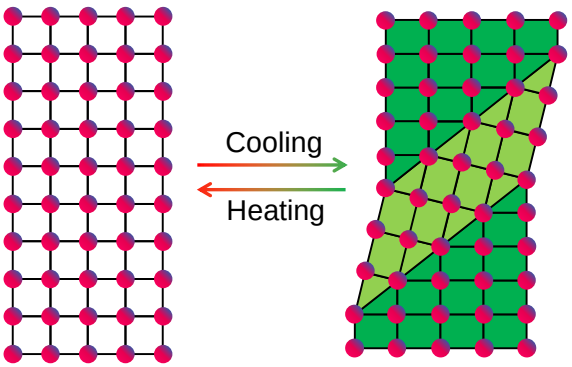

(a) Temperature-induced phase transformation

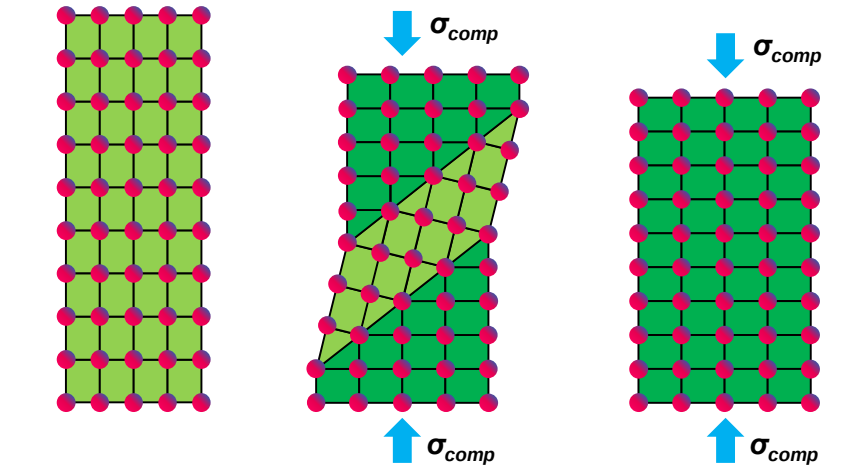

(b) Stress-induced martensite reorientation between different martensite variants

Figure 1.2 Schematics of (a) phase transformation and (b) martensite reorientation.

(see the point (d) in Fig. 1.3) as each martensite variant has the same energy and all the different variants are energetically stable at this low temperature without stress. Then upon heating (to above a temperature A_s (Austenite start temperature)) the A-phase nucleates and grows with the expenses of the detwinned martensite till all the material recovers to A-phase (at a temperature $\geq A_f$ (Austenite finish temperature)) with the original shape (because the austenite has the unique cubic crystal structure) as shown by the process from (d) to (a) in Fig. 1.3.

Another promising property of FSMAs (and SMAs) is pseudoelasticity (also called superelasticity). It presents that, when the temperature is high enough to keep the material at the state of austenite phase, the austenite FSMA/SMA material has ability to deform to the detwinned martensite with a large strain (up to $\sim 10\%$) by applying mechanical load and can totally recover to the original austenite state (with zero strain) with unloading (as shown by the process from point (1) to (2), and back to point (1) Fig. 1.3).

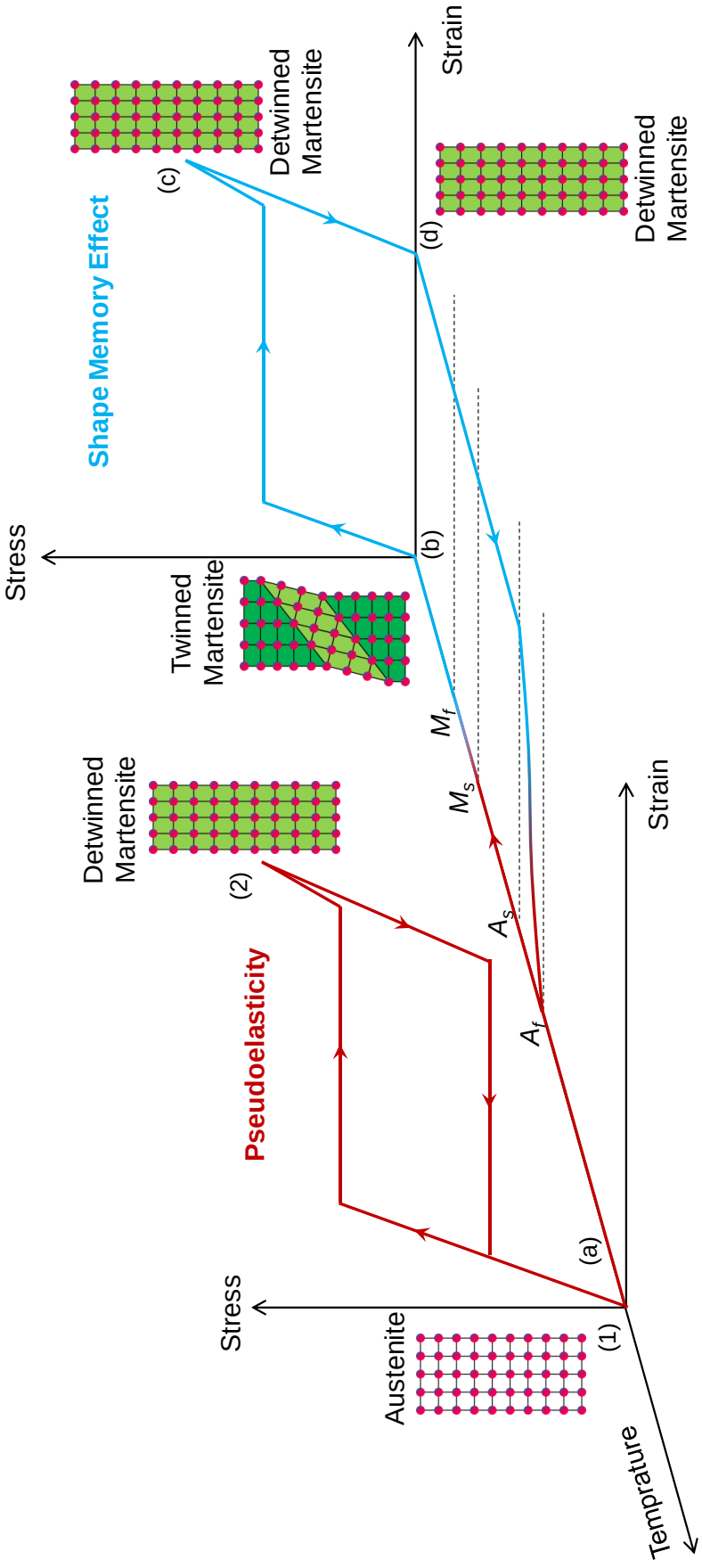

Figure 1.3 Schematics of shape memory effect and pseudoelasticity.

- **Magnetic field-induced strain**

  Besides the classical shape memory effect and the pseudoelasticity, the magnetic properties of FSMAs enable them to achieve magnetic-field-induced strain (MFIS) by two mechanisms: magnetic-field-induced martensite reorientation and magnetic-field-induced phase transformation. The martensite of Ni_2MnGa is ferromagnetic and has high magnetic anisotropy, so that, in the absence of an external magnetic field, the martensite variants are spontaneously magnetized

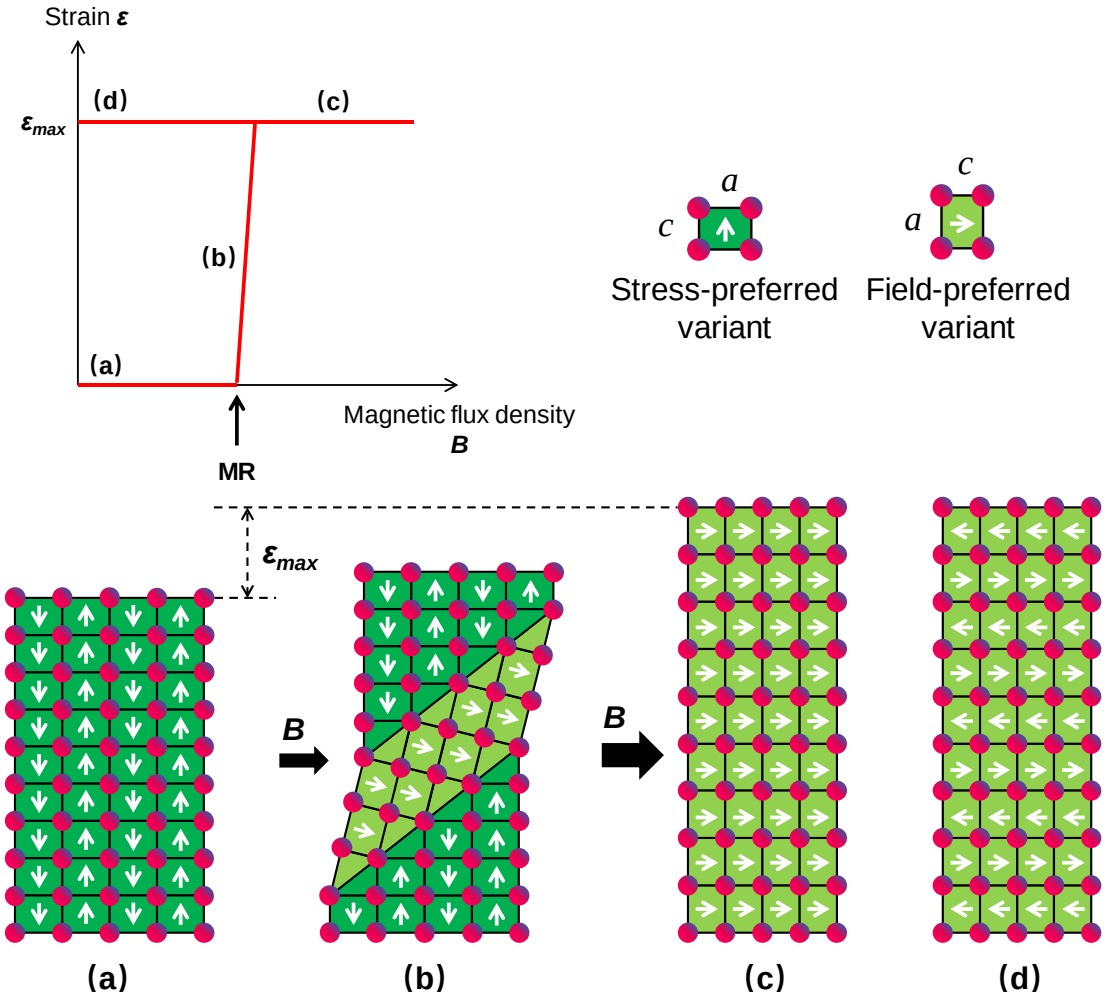

Figure 1.4 Schematic of magnetic field-induced martensite reorientation.

as the local magnetization vector prefers to align with the short axis of the crystal structure, which is so-called easy magnetization axis (as shown by the up and down magnetization vectors (white arrows) in the magnetic domains in Fig. 1.4(a)), to minimize the Magnetocrystalline Anisotropy Energy (MAE). When an external magnetic field is applied perpendicular to the *c*-axis of a martensite variant, the magnetization direction energetically prefers to rotate to align with the applied magnetic field direction (driven by Zeeman energy). However, the derivation of the rotated magnetization direction from the easy magnetization axis *c* will induce a large MAE. If the MAE is larger than the detwinning energy (the energy to drive the twin boundary motion) in Ni_2MnGa, the atoms of the original martensite variant will shift to new sites and the variant will transform to a new variant with the short *c*-axis along the applied magnetic field (so-called field-preferred variant, as shown in Fig. 1.4(b)) in order to minimize the total magnetic energy. This process is so-called magnetic field-induced martensite reorientation. With further increasing of the magnetic field, the martensite reorientation keeps taking place, which is achieved by the twin boundary motion, and finally all the materials transform to be the state of the field-preferred variant (Fig. 1.4(c)). When the external magnetic field is removed, the field-preferred variant with the horizontal *c*-axis remains and the magnetic domains of the spontaneous-magnetization vectors pointing to left or right are formed. Due to the shape of martensite variant is tetragonal, the martensite reorientation (the direction change of the short axis *c*) induces a length change in the material, which produces macroscopic deformation strain (comparing Figs. 1.4(a) and (c)). The maximum strain value ε_{max}, depending on the degree of tetragonality of the martensite variant, can be theoretically calculated by $1 - \frac{c}{a}$. Based on the typical values of

the lattice parameters of Ni_2MnGa have been reported in (Heczko et al., 2002; Murray et al., 2000; Straka et al., 2006) ($a \approx 0.595$ nm and $c \approx 0.561$ nm for 10M martensite and $a_0 \approx 0.584$ nm for cubic austenite at room temperature), the maximum strain of the martensite reorientation for a 10M martensite is around 6%. It should be noted that, in this process, the material properties of the high magnetic anisotropy and the low twinning stress (or detwinning energy) are the important factors. If the MAE of the material is smaller than the detwining energy, the material will only take the magnetization rotation, without the martensite reorientation (without changing the direction of the short axis c). Therefore, for achieving the magnetic field-induced martensite reorientation, large MAE of the material is helpful.

The other mechanism to obtain MFIS is the magnetic field-induced phase transformation (Bruno et al., 2017; Haldar et al., 2014; Kainuma et al., 2006; Karaca et al., 2007, 2009, 2007). When a strong magnetic field is applied on the austenite phase, the magnetic energy (Zeeman energy) can drive the austenite to transform to the martensite phase when the magnetization of martensite is larger than that of the austenite, and vise versa. That means, the field-induced phase transformation depends on the material properties: the difference in the magnetization between the martensite and the austenite. Because the forward/reverse martensitic phase transformation releases/absorbs large latent heat, the field-induced phase transformation can be used to design magneto-caloric refrigerators (Franco and Conde, 2012; Qu et al., 2017; Zhao et al., 2017). But due to the phase transformation needs to be driven by very strong magnetic field (at least several Tesla) (Bruno et al., 2017; Haldar et al., 2014; Kainuma et al., 2006; Karaca et al., 2007, 2009, 2007), the applications are seriously limited up to now. In this thesis, we focus

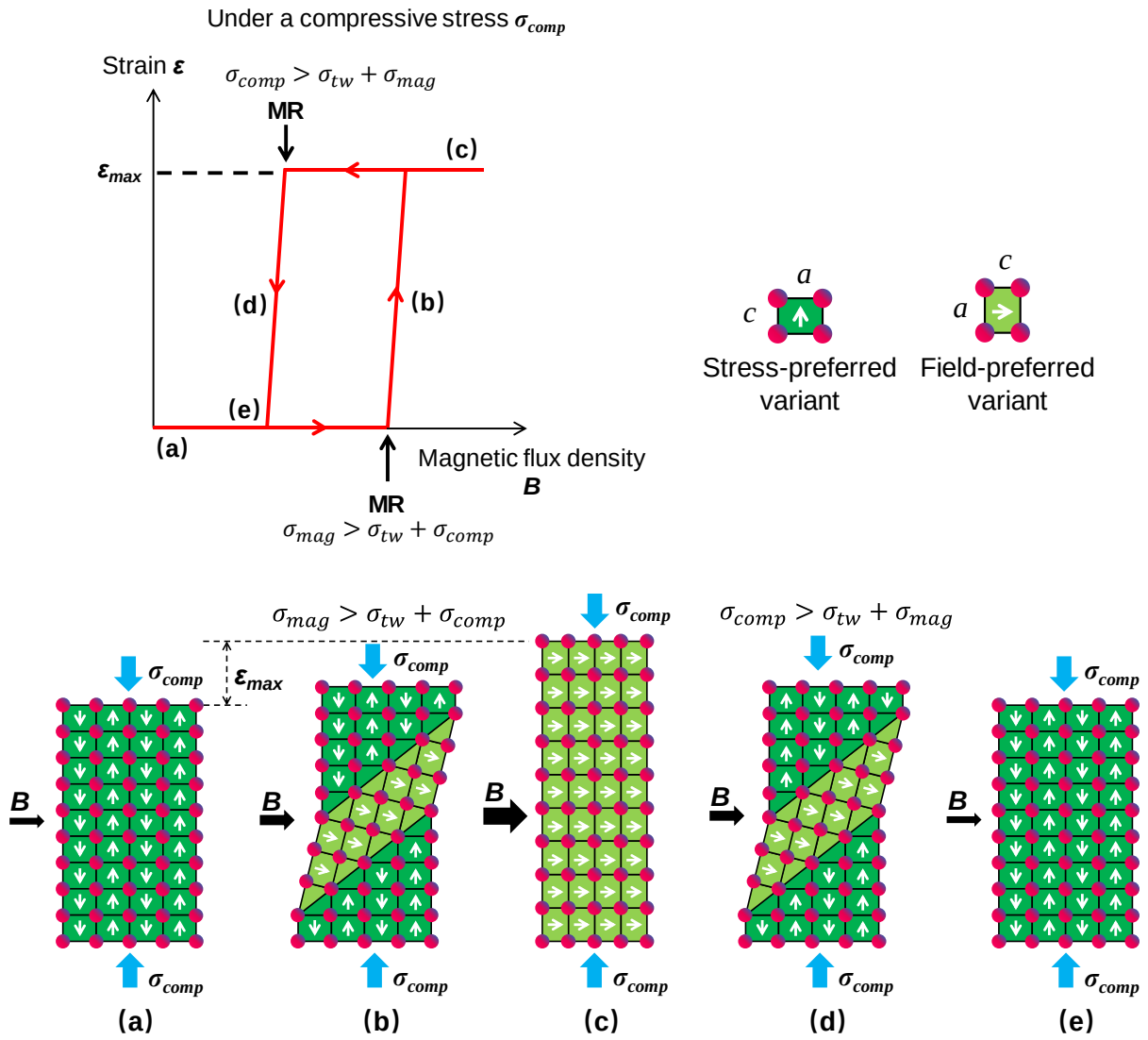

Figure 1.5 Schematic of magneto-mechanical loading-induced reversible martensite reorientation.

our attention on the magnetic field-induced martensite reorientation, due to the twinning stress of Ni_2MnGa is very small (< 2 MPa) so that it is easier to be driven by a weak magnetic field (< 0.8 Tesla) and thus more promising for engineering applications, such as actuators (Asua et al., 2014; Majewska et al., 2010; Smith et al., 2014; Techapiesancharoenkij et al., 2009; Yin et al., 2016).

Considering that a reversible strain is generally required in most of the applications, a rotating magnetic field (Chmielus et al., 2008, 2011; Lawrence et al., 2016) or a magneto-mechanical biaxial load (Henry et al., 2002; Lai et al., 2008; Karaca et al., 2006, 2009; Pascan et al., 2015) can be applied on the material to drive the reversible martensite reorientation, in which the later method (magneto-mechanical biaxial load) is more extensively adopted due to its easier implementation. To obtain the reversible strain by the magneto-mechanical biaxial load, normally a cyclic magnetic field and a constant compressive stress are applied at the same time along perpendicular directions as shown in Fig. 1.5(a). When the horizontal magnetic field is small (e.g., near 0), the material is in the state of the stress-preferred variant with the short axis along the vertical compressive stress σ_{comp} (see Fig. 1.5(a)). When the magnetic field is increased to a value with the effective magnetic stress σ_{mag} larger than the sum of twinning stress σ_{tw} and the mechanical compressive stress σ_{comp} (i.e., satisfying criterion $\sigma_{mag} > \sigma_{tw} + \sigma_{comp}$) (Heczko and Straka, 2004; Straka et al., 2006), the field-induced martensite reorientation takes place (the stress-preferred variant transforms to the magnetic field-induced variant) as shown in Fig. 1.5(b). With the magnetic field further increases, the martensite reorientation will be completed (with all the material transforming to the state of the field-preferred variant) and the largest strain ε_{max} of the material is obtained, see Fig. 1.5(c). Then, when the magnetic field is decreased to a value satisfying criterion $\sigma_{comp} > \sigma_{tw} + \sigma_{mag}$ (Heczko and Straka, 2004; Pascan, 2015; Straka et al., 2006), the reverse martensite reorientation from the field-preferred variant to the stress-preferred variant is activated (see Fig. 1.5(d)). Finally all the materials transform back to the stress-preferred variant when the magnetic field reduces to a very small value

(see Fig. 1.5(e)). In this process (from (a) to (e) in Fig. 1.5), the competition between the mechanical and magnetic stresses governs the material state, and the reversible strain can be achieved in the magnetic actuation cycle. This mechanism gives the FSMA material the ability to obtain the high frequency deformation under the high frequency actuation of magneto-mechanical load.

1.2 Motivations and objectives

Compared to other kinds of smart materials, FSMAs have the most attractive advantages: the large output strain and the high actuation frequency can be obtained at the same time. Although the material properties and the quasi-static behaviors of FSMAs have been investigated comprehensively, the existing studies are not enough to have a profound understanding on the high frequency performance of FSMA and to support their high-frequency applications. The main difficulty in studying the high-frequency performance is the complicated coupling of the dynamic effect and thermal effect. The early experimental studies on the dynamic behaviors of FSMAs revealed loading-frequency effects and the associated resonance phenomena in the cyclic magnetic field-induced strain (via cyclic martensite reorientation). That means, the cyclic strain depends on the actuation frequency, system mass and stiffness and compressive stress level (Henry et al., 2002; Lai et al., 2008; Karaca et al., 2006; Techapiesancharoenkij et al., 2009). In addition, the frequency effects were modeled by a spring-mass-damper oscillator model (Henry, 2002; Sarawate and Dapino, 2008; Tan and Elahinia, 2008) and a discrete twin boundary dynamic model (Faran et al., 2017; Faran and Shilo, 2016). However, most of these early experiments were performed for short actuation times (several seconds) to avoid temperature effects (Henry et al., 2002; Lai et al., 2008; Karaca et al., 2006;

Techapiesancharoenkij et al., 2009). Besides the studies of the short time actuations, long-time performance and stability caused research interest recently (Pascan et al., 2015; Pascan, 2015). It was shown that, during the long time cyclic actuation, the fast frictional twin boundary motion can induce a quick dissipation heat accumulation and increase the specimen temperature ("self-heating") significantly (Pascan et al., 2015), which is generally ignored in the early studies of the quasi-static and short-time actuations. The temperature variation can influence the performances of FSMAs because several physical properties related to martensite reorientation of FSMAs are sensitive to the temperature (Aaltio et al., 2008; Adachi et al., 2017; Glavatska et al., 2002; Heczko et al., 2017, 2002; Okamoto et al., 2008; Soroka et al., 2018; Sozinov et al., 2017; Straka et al., 2011a, 2006, 2015, 2012; Vronka et al., 2017; Zreihan et al., 2015). Moreover, the self-heating can block the magnetic field-induced strain (Pascan et al., 2015; Jugo et al., 2018). That means, the previously reported large output strain amplitude in the quasi-static or the short-time actuation on FSMA in fact can not be guaranteed in a long-time actuation and the self-heating might induce to an instability of magnetic field-induced strain. However, up to now, the long-time performance of FSMAs still lack systematic investigation and understanding, particularly the coupling thermal effect (the influence of the temperature variation) and the dynamic effect during the long-time high-frequency magnetic actuation.

In this work, we focus on the magneto-thermo-mechanical factors influencing the long-time high-frequency performance of FSMA. Systematic experiments of the long-time actuation (> 100 seconds) are performed under different magnetic field frequency, initial compressive stress and ambient heat-exchange efficiency. Based on the experimental results and a 1D heat transfer model, the critical conditions to obtain a large stable high-frequency output strain in the long-time actuation of FSMA are

proposed. Moreover, in-situ Digital Image Correlation (DIC) method is used during the high-frequency actuation to help us understand the nominal high-frequency responses from the microscopic view of the temperature-induced phase transformation and the field-induced martensite reorientation, and their compatibility between different material variants/phases.

The remaining part of this thesis is organized as follows: Chapter 2 introduces the experimental setup for the high-frequency magnetic actuation. In Chapter 3, the systematic long-time actuation tests are reported, particularly the thermal effects on the long-time stable output strain of FSMA are experimentally revealed and theoretically understood based on a 1D heat-transfer model. Based on analyses of local strain evolution and microstructure compatibility, Chapter 4 presents a new mechanism that magnetic field-driven twin boundary motion and temperature-driven phase boundary motion can be simultaneously activated during the high-frequency actuation of FSMA. Finally, the conclusions and perspectives of this thesis are provided in Chapter 5.

Chapter 2

Experimental setup

To drive the high-frequency martensite reorientation of FSMA, an experiment system for the magneto-thermo-mechanical loading and the local strain characterization is developed. This chapter introduces the details of the experimental setup, including systems of electromagnetic actuation, ambient controlling, data acquisition and optical recording.

2.1 Electromagnetic actuation and data acquisition system

The high-frequency actuation system used in this work is shown in Fig. 2.1. The whole system is fixed on a damping grounded frame to prevent system vibrations induced by the high-frequency actuation. The electromagnet system used in our work is developed by *Bouhnik* enterprise. Two cylindrical electromagnet poles (from SIGMAPHI) with a diameter of 25 mm are installed horizontally (along x-direction) with a 5 mm gap

(thus having 25 mm × 25 mm × 5 mm space to install the specimen). To achieve a high frequency and strong magnetic field, an ac-electric current (up to 130 A and 500 Hz) are applied on the electromagnet coils, which is controlled by using LabVIEW with help of a NI USB 6251 device. As the high frequency strong ac-electric current will induce to a quite large heat generation in the coils, a water-cooling system (with a water flow of constant 15 °C) surrounds the coils to avoid the temperature rise in the coils so that a stable magnetic field can be achieved for the long-time actuation. The electromagnet is not completely enclosed as we need some in-situ observations on the specimen surface during the test (see the photo of the experimental setup in Fig. 2.1(c)). With this electromagnet system, a stable cyclic magnetic field with up to ±0.78 Tesla magnetic flux density and 500 Hz frequency can be achieved for a long working time. The specimen is fixed between the magnetic poles by two Plexiglas holders with specimen long side along the vertical direction (y-direction). (The Plexiglas is a non-magnetic material with a low-density and a low thermal conductivity.) A spring (with stiffness of 5.5 kN/m) is installed on the upper Plexiglas holder which can be compressed by a micrometer screw and allows us to apply a compressive force along y-direction. By using this system, the cyclic magnetic field and compressive stress can be perpendicularly applied on the FSMA specimen. The competition between the horizontal magnetic field and the vertical compressive stress can drive cyclic martensite reorientation and achieve high-frequency output strain in the FSMA specimen.

To obtain the specimen responses during the actuation, the specimen strain, stress and temperature are monitored by different sensors. The changing deformation of the specimen along y-direction is measured by a laser displacement sensor (LK-H027 from Keyence) on the upper holder. The force along y-direction is measured by a force sensor (Kistler 9311B) fixed at the lower end of the lower specimen holder. In order

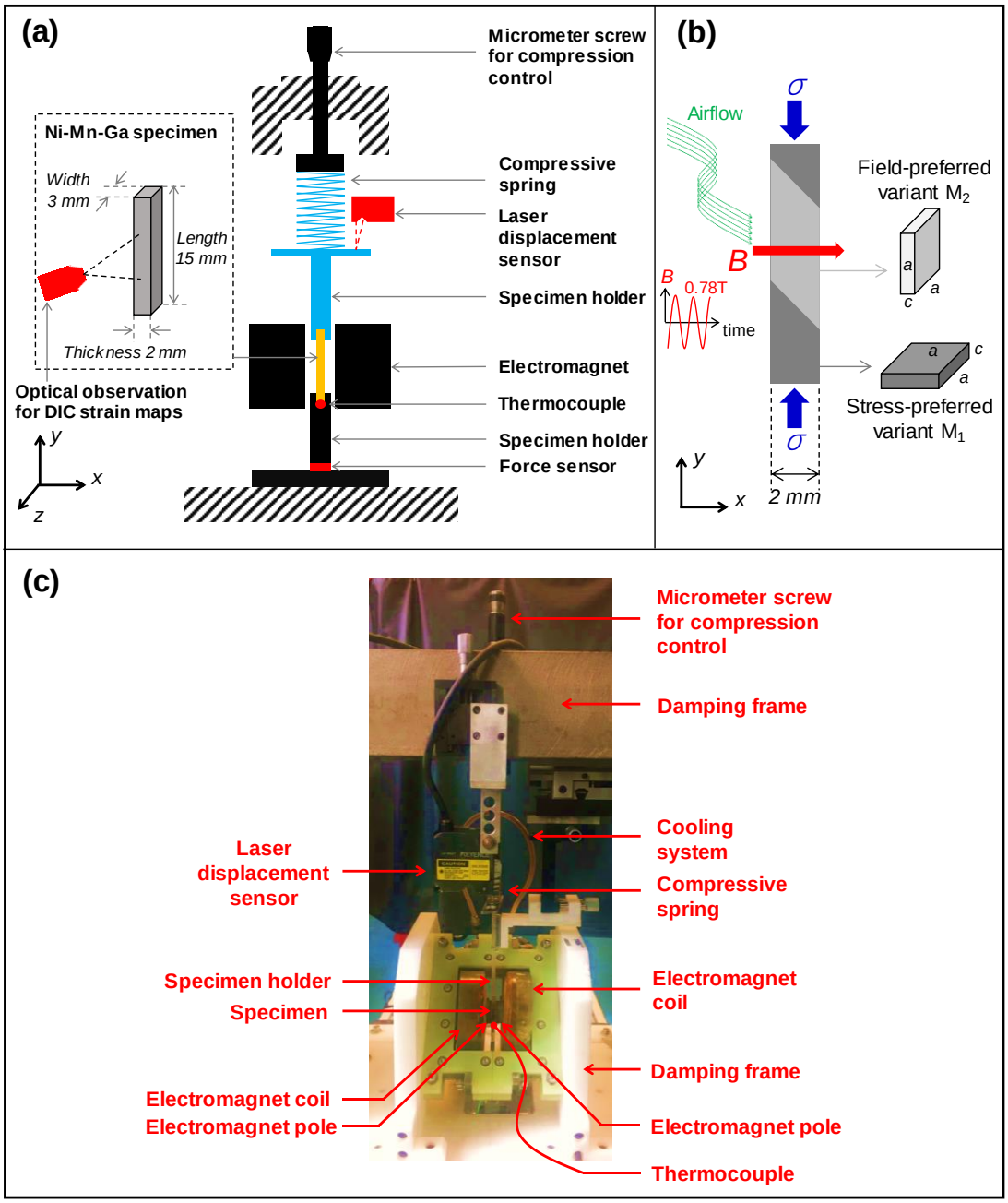

Figure 2.1 (a) Schematic of actuation system to achieve high-frequency cyclic martensite reorientation, where the fixed parts (immobile components) during the dynamic actuation are in black, the moving parts (the spring and the upper sample holder) are in blue and the measuring sensors are in red. (b) Schematic of the martensite reorientation between the stress-preferred martensite variant (M1) and the magnetic-field-preferred martensite variant (M2) in Ni-Mn-Ga specimen under the magneto-mechanical actuation. Approximated tetragonal martensite variant of one short axis (c-axis) and two long axes (a-axis) are adopted and the difference between a and c is shown exaggeratedly here. (c) Photo of the experimental setup for high-frequency magnetic actuation.

to have a precise description on the specimen responses, we acquire 25 data points of deformation and force per strain cycle. The global temperature of the specimen is monitored by a thermocouple (K-type, 0.5 mm sheath diameter) at the lower end of the specimen with the sampling rate of 170 Hz. All the above mentioned data acquisitions are performed on the same computer to guarantee a high time accuracy (10^{-7} second) of data synchronization. In summary, for a test with an input of cyclic magnetic field, the evolutions of strain, stress and temperature of the specimen can be acquired as the typical results shown in Fig. 2.2. It's seen that the acquired data points are enough to provide a good description of the specimen responses respectively.

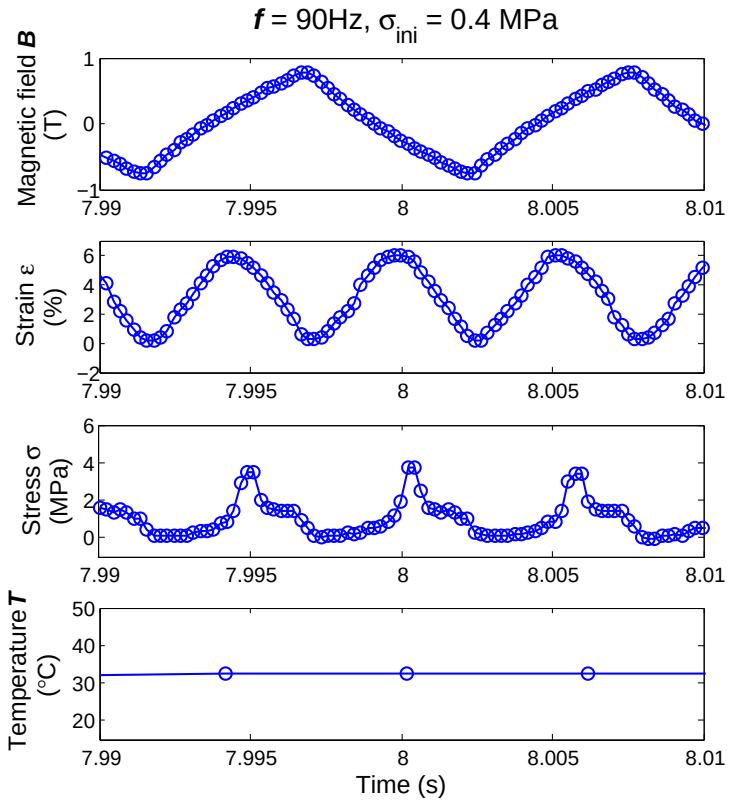

Figure 2.2 Typical acquired data sets of a cyclic dynamic test.

2.2 Ambient controlling during the test

To investigate the ambient effect, an airflow with a constant temperature (around the room temperature) are forced to pass through the specimen to change the heat-exchange efficiency between the specimen and the ambient during the magnetic actuation. The airflow velocity can be controlled by a valve and measured by a portable airflow velocity indicator. The heat–exchange efficiency can be evaluated by a characteristic heat-relaxation time t_h (He et al., 2010; He and Sun, 2010), which is measured as follows:

The specimen is held between two electromagnet poles during the tests and heated

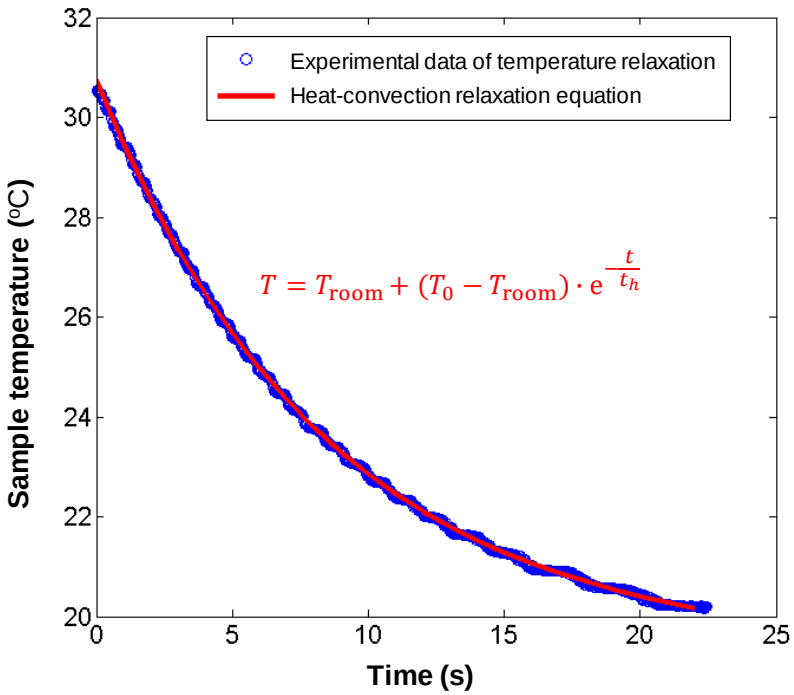

Figure 2.3 Temperature relaxation of Ni-Mn-Ga single crystal sample ($2 \times 3 \times 15$ mm) under the ambient airflow of 15 m/s. The fitted characteristic heat-relaxation time t_h is 8.8 s.

due to the high-frequency frictional twin boundary motion. To determine the characteristic heat−relaxation time t_h, the evolution of the specimen temperature after turning off the magnetic field is measured in a constant ambient airflow. Because there is no heat generation in the specimen, the temperature relaxation is only due to the heat convection from the specimen to the ambient. The value of the heat-relaxation time t_h is determined by fitting the experimental cooling curve with an exponential equation $T = T_{room} + (T_0 - T_{room}) \cdot e^{-\frac{t}{t_h}}$, which describes the heat-convection relaxation (He et al., 2010; He and Sun, 2010). For example, in Fig. 2.3, the value of t_h at the ambient airflow velocity of 15 m/s is determined to be 8.8 s. By using this method, t_h at different ambient conditions can be experimentally measured.

2.3 Optical observation on the specimen surface

During the tests, a CMOS camera of 2048×1088 pixels (Basler ac A2000-340 km) with Nikkor lens is used to record the optical images of the specimen surface, so that after the test, the recorded images can be processed by Digital Image Correlation (DIC) software Vic-2D (Correlated Solutions) to obtain the local strain maps. But considering the limitation of recording rate (maximum 100 frames/s) of the imaging system, it is difficult to directly record enough frames (such as 10 frames/cycle) in a single deformation cycle (with a period of 5.56 ms per cycle at an actuation frequency of 180 Hz). To solve this problem, the recording frequency is set as $f_{image} = \frac{n}{n \cdot m + 1} \cdot f_{strain}$, as shown in Fig. 2.4, where f_{strain} is the strain frequency, n represents the number of the images needed to describe a strain cycle ($n \gg 1$) and m represents the number of the strain cycles where an image is recorded). This setting can ensure that the strain frequency is not exactly divisible by the recording frequency so that there is a phase

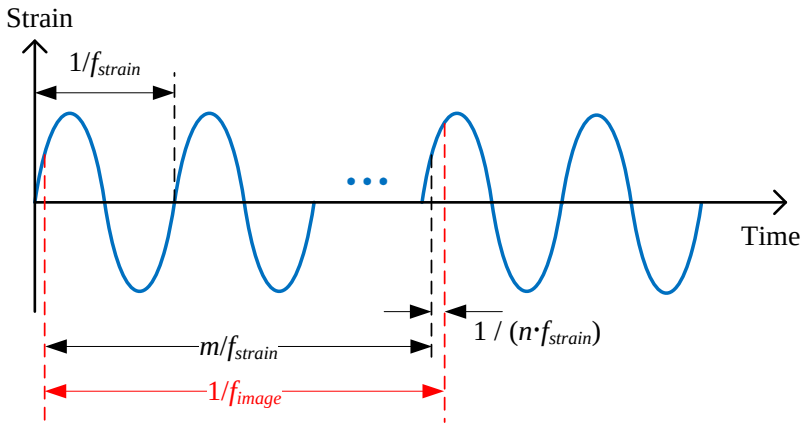

Figure 2.4 Schematic of the optical imaging method during high-frequency deformation.

difference between two adjacently recorded images, see Fig. 2.4. In this way, the phase difference ($\frac{1}{n \cdot f_{strain}}$) is set as $1/n$ of the strain cycle, which means n continuously recorded images with different phases can describe a complete strain cycle. It's noted that although the continuous recorded images are from different strain cycle, they are equivalent to the images from the single strain cycle because the material behaviors are repeated for different cycles at the stable state. By using this recording system and the method, the local strain field evolution during the high-frequency magnetic actuation can be obtained by using the method of Digital Image Correlation (Vic-2D), which helps us understand the mechanism of the macroscopic performance of FSMA from a local view.

Chapter 3

Thermal effects on high-frequency magnetic field-induced martensite reorientation

Ferromagnetic Shape Memory Alloys (FSMAs) exhibit large strains by the magnetic-field-induced martensite reorientation. But, due to the high-frequency field-induced cyclic frictional martensite twin boundary motion in FSMAs, the dissipation heat can cause a large temperature rise. Thus, the output strain amplitude of FSMAs would decrease significantly if the temperature increases to be high enough to trigger the Martensite-Austenite phase transformation. Such thermal effects on the dynamic responses of FSMAs are unclear in literature because most existing dynamic experiments were performed only for a short-time period (a few seconds) to avoid the temperature rise. In this chapter, systematic long-time experiments (> 100 seconds) on a Ni-Mn-Ga single crystal are conducted at various levels of magnetic field frequency, initial

compressive stress and ambient airflow velocity. It is found that, during the long-time actuation, the specimen temperature increases and then saturates at a certain level (stable temperature) while the strain oscillation evolves to a stable cycle; both the stable temperature and the stable strain amplitude depend on the frequency, the stress level and the heat exchange condition (i.e., ambient airflow velocity). Particularly, when the specimen temperature reaches a critical level to partially transform the martensite to the austenite, the output strain amplitude reduces suddenly because of less martensite reorientation. Changing the ambient heat-exchange condition (by the airflow) can modify the specimen temperature evolution to avoid the phase transformation, but it also changes the behaviors of the martensite reorientation that is sensitive to temperature. Eventually, the output strain amplitude depends on the airflow velocity non-monotonically, i.e., there exists a critical heat exchange condition to achieve the maximum stable strain amplitude. Based on the systematic experiments and a simplified one-dimensional heat-transfer model, the critical condition can be determined. The new experimental phenomena of the thermal effects can be well understood and described by the heat-transfer model. Further, instead of avoiding the temperature rise and the phase transformation, we propose to take advantage of the interaction between the temperature-induced phase transformation and the magnetic-field-induced martensite reorientation to develop a special "isothermal" FSMA actuator with a tunable output strain amplitude and a constant working temperature. This chapter provides systematic experimental data and theoretical analysis for understanding the thermo-magneto-mechanical coupling in FSMAs and developing reliable high-frequency long-time running FSMA-actuators.

3.1 Introduction

Ferromagnetic Shape Memory Alloy is a typical smart material with thermo-magneto-mechanical coupling, which can provide a large recoverable deformation (up to 10% strain) by the temperature-, stress- or magnetic-field-induced phase transformation (PT) (Arndt et al., 2006; Bruno et al., 2017; Cisse et al., 2016; Haldar et al., 2014; Kainuma et al., 2006; Karaca et al., 2006; Liu et al., 2014; Rogovoy and Stolbova, 2016; Sehitoglu et al., 2012; Sutou et al., 2004) and the magneto-mechanically-driven martensite reorientation (MR) (Chen et al., 2013a, 2014; Cisse et al., 2016; Dai et al., 2018; He et al., 2011, 2012; Heczko et al., 2016; Karaca et al., 2006; Kiefer and Lagoudas, 2005, 2004; Molnar et al., 2008; Murray et al., 2000; O'Handley et al., 2000), leading to various potential engineering applications. Normally, the martensitic phase transformation of FSMA needs to be triggered by a high-level stress or a strong magnetic field, and is accompanied by large latent heat release/absorption that can be used as energy harvesters (Basaran, 2009; Saren et al., 2015; Sayyaadi and Farsangi, 2015) and magneto-caloric refrigerators (Franco and Conde, 2012; Qu et al., 2017; Zhao et al., 2017). On the other hand, the martensite reorientation can be driven by a low stress ($\sim$ 1 MPa) or a weak magnetic field ($<$ 1 Tesla) and has small hysteresis and energy dissipation, which are suitable for the applications such as actuators (Asua et al., 2014; Majewska et al., 2010; Smith et al., 2014; Techapiesancharoenkij et al., 2009; Yin et al., 2016) and sensors (Hobza et al., 2018; Sarawate and Dapino, 2006; Stephan et al., 2011; Yin et al., 2016). Particularly, there exists a special twin boundary (so-called Type II twin boundary) with ultra-low frictional twinning stress ($\sim$ 0.2 MPa) during the field- and/or stress-driven martensite reorientation in FSMA Ni-Mn-Ga single crystal, due to the monoclinic distortion of its 10M tetragonal martensite phase (although the

deviation is small, e.g., the characteristic angle $\gamma = 90.37°$ is close to 90° of a tetragonal lattice) (Chulist et al., 2013; Heczko et al., 2013; Liu and Xie, 2003; Pascan et al., 2015; Sozinov et al., 2011; Straka et al., 2012, 2011b; Zou et al., 2018; Zreihan et al., 2015). Such low driving force and small dissipation make FSMA a promising candidate for actuators.

Although the temperature rise due to the low energy dissipation of martensite reorientation in FSMA is negligible in the slow or quasi-static loading conditions, it cannot be ignored in high-frequency magnetic loadings (> 100 Hz) because the dissipation due to the frictional twin boundary motion of martensite reorientation (Blanter et al., 2007; Cui et al., 2017; He et al., 2012, 2011; Heczko et al., 2016; Karaca et al., 2006; Kiefer and Lagoudas, 2005, 2004; Molnar et al., 2008; Murray et al., 2000; O'Handley et al., 2000; Pagounis et al., 2014; Yu et al., 2015) and the eddy current inside the material can accumulate quickly to induce significant temperature rise (Henry et al., 2002; Henry, 2002; Lai, 2009; Lai et al., 2008). Moreover, several physical properties related to martensite reorientation of FSMA are sensitive to the temperature (Aaltio et al., 2008; Adachi et al., 2017; Glavatska et al., 2002; Heczko et al., 2017, 2002; Okamoto et al., 2008; Soroka et al., 2018; Sozinov et al., 2017; Straka et al., 2011a, 2006, 2015, 2012; Vronka et al., 2017; Zreihan et al., 2015). That is why most existing high-frequency dynamic experiments on FSMA were performed only for a short-time period to avoid significant temperature rise (Henry et al., 2002; Henry, 2002; Lai, 2009; Lai et al., 2008). In such short-time experiments, although the output strain seems to be stable with nearly constant strain amplitude, the temperature of the specimen keeps increasing without reaching the steady state, e.g., the temperature increasing rate during the short-time actuation of 20 seconds is larger than 0.5 °C/s in (Pascan, 2015) and 0.3 °C/s in (Lai, 2009). Therefore, such short-time actuation

systems are not strictly stable since not all the thermo-magneto-mechanical responses have reached the steady states. Thus, it's still unknown whether the large output strain of FSMA under high-frequency magnetic loadings reported in the literature can be guaranteed for the long-time performance (e.g., > 100 s) or not.

One of the main problems caused by the temperature rise is the temperature-induced Martensite-to-Austenite (M-to-A) phase transformation (Auricchio et al., 2014; Bhattacharya, 2003; Iadicola and Shaw, 2004; Otsuka and Wayman, 1999), which will disturb the field-induced martensite reorientation in the long-time actuation of FSMA. To my best knowledge, studies about the effect of phase transformation on the martensite reorientation of FSMA are seldom reported in the literature. This is possibly due to the fact that the stress and magnetic field levels for martensite reorientation are too small to trigger the phase transformation (Haldar et al., 2014; Karaca et al., 2006, 2009), and that the energy dissipation of martensite reorientation per cycle is small (Chen et al., 2013a; Karaca et al., 2006). However, in the high-frequency magnetic loadings (e.g., beyond 100 Hz, such high-frequency working condition is a main advantage of FSMA actuators over the traditional shape memory alloy (SMA) actuators), the small dissipation heat can accumulate and thus generate significant temperature rise (Lai, 2009; Pascan, 2015; Pascan et al., 2015) especially when the ambient heat exchange is weak (e.g., in still air). The effects of ambient heat exchange on the phase transformation and the mechanical deformation of traditional SMAs have been reported in the literature such as (Blanter et al., 2007; Brinson et al., 2004; He and Sun, 2010, 2011; He et al., 2010; Shaw and Kyriakides, 1995). It is predicted that controlling the ambient heat exchange condition can be a solution to the problem of the temperature rise in FSMA under high-frequency magnetic loadings. Therefore, in my study on the long-time high-frequency magnetic actuation of FSMA, ambient airflow of various

velocities is forced to pass through the FSMA specimen so that the specimen can be in different heat exchange conditions. Different stable states were finally reached in the specimen, and we found a non-monotonic dependence of the output strain amplitude on the airflow velocity. Based on such dependence and a heat balance analysis, the thermal effects on the dynamic behaviors of FSMA are revealed for the first time. Further, the critical thermo-magneto-mechanical conditions to achieve a large stable output strain are provided.

It is normally expected that, when the ambient airflow (heat exchange efficiency) is sufficiently strong (of large velocity), the specimen temperature can be kept lower than the phase transformation temperature (such as the Austenite starting temperature As or the martensite finishing temperature M_f) so as to avoid the phase transformation and maintain the large strain amplitude of the field-induced martensite reorientation. However, it is founded in my study that while the phase transformation can be avoided, the output strain amplitude of FSMA was reduced significantly when the steady-state temperature was much lower than A_s or M_f. This is attributed to the fact that the internal friction of martensite reorientation is sensitive to temperature: the frictional twinning stress for the Type I twin boundary increases with decreasing temperature (Heczko and Straka, 2003; Soroka et al., 2018; Sozinov et al., 2017; Straka et al., 2012, 2011a, 2006). Therefore, for the optimal condition of the largest stable cyclic strain in dynamic actuation, the temperature of FSMA should be kept close to (but lower than) the characteristic phase transformation temperature by applying a proper ambient airflow.

On the other hand, if the applied airflow is weak (of low velocity), the FSMA specimen temperature can reach A_s, triggering M-to-A phase transformation. It was

revealed in my current experiments that the phase transformation occurred locally: only part of the specimen underwent M-to-A phase transformation, and the remaining untransformed part (M-phase) still kept the cyclic martensite reorientation under the magnetic actuation. So the output strain depended on the fraction of the remaining martensite. It is a spontaneous self-organization process that the specimen adjusted the fraction of the remaining martensite so as to reach the heat balance between the heat transferred by the airflow and the heat generated from the eddy current and the martensite reorientation of the remaining martensite. It was found in the current study that the stable output strain (corresponding to the fraction of the remaining M-phase) was sensitive to the ambient heat exchange condition (i.e., airflow velocity), while the stable temperature of the specimen was always around M_f. In other words, a special type of long-time FSMA actuator is founded, whose working temperature (steady-state temperature) always keeps constant around M_f and whose output strain amplitude can be controlled by the ambient airflow. The new phenomena revealed in my experiments can be well understood and described by the theoretical analysis based on a heat-transfer model. This experimental and theoretical study is expected to provide fundamental information for understanding and modeling of the thermo-magneto-mechanical coupling in the dynamic actuation of FSMAs.

3.2 Experimental setup and testing procedures

3.2.1 Material properties and experimental setup

A $Ni_{50}Mn_{28}Ga_{22}$ (at. %) single crystal rectangular bar with dimensions in 2×3×15 mm (from ETO Magnetic GmbH) were used in the experiments. The specimen is in the state of 10M martensite phase at room temperature. All faces of the specimen were cut parallel to the {100} planes of the parent cubic austenite (with the derivation of less than 2°). From a DSC (differential scanning calorimetry) test as shown in Fig. 3.1, the material characteristic transformation temperatures M_f, M_s, A_s and A_f were obtained as 35.5 °C, 36.5 °C, 41.5 °C and 42.2 °C, respectively. The specimen was installed into a magneto-mechanical loading system as shown in Fig. 2.1. A high-frequency magnetic field (with magnetic flux density $\boldsymbol{B}$ cyclically varying between ±0.78 Tesla in a triangle waveform) is applied horizontally along the x-direction while a compressive stress is applied vertically by a spring along the y-direction. The deformation of the specimen along y-direction is measured by a laser displacement sensor (Keyence LK-H027) at the top of the upper specimen holder, and the specimen temperature is measured by a thermocouple (K-type, 0.5 mm sheath diameter) attached at the bottom surface of the specimen. A force sensor (Kistler 9301B) under the lower specimen holder measures the compressive stress. In order to reduce the heat conduction from the specimen to the fixtures, the specimen holders at the two ends of the specimen are made of plexiglass with low heat conductivity. Thus, it is assumed that the heat exchange is mostly governed by the heat convection via the specimen surface rather than the heat conduction via the specimen ends. To accurately describe the strain and stress evolutions, the displacement and force sensors are set to acquire 25 data points per cycle.

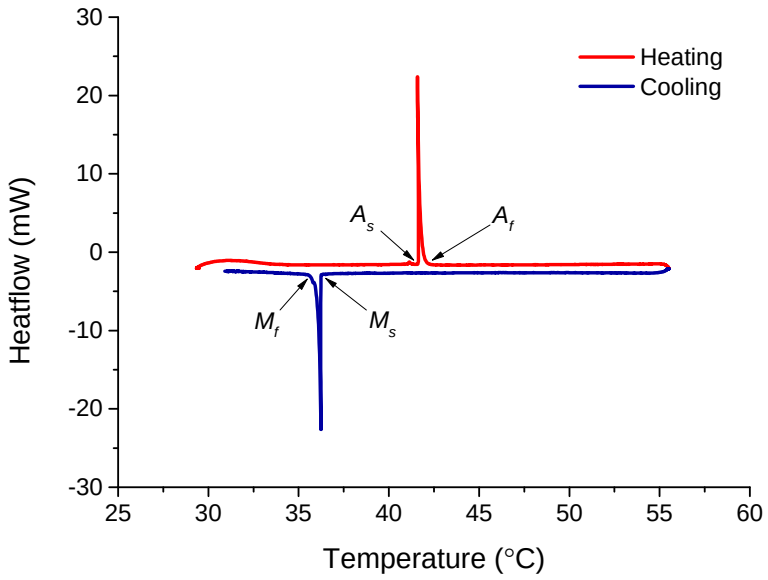

Figure 3.1 DSC curves of the single-crystal Ni-Mn-Ga at the heating/cooling rate of 0.5 °C/min.

For the temperature measurements, the thermocouple is set at the maximum sampling rate of 170 Hz which helps us capture the global temperature variation versus time. During tests, all the deformation, force and temperature data are acquired synchronously (with time accuracy of 10^{-7} s) by using Labview platforms. In addition, during the dynamic actuation, a CMOS camera of 2048×1088 pixels (Basler acA2000-340 km) with Nikkor lens is used to record the specimen surface morphology (in a gauge section of around 5 mm). Then the recorded optical images are processed by Digital Image Correlation (DIC) software Vic-2D (Correlated Solutions) to obtain the local strain fields.

3.2.2 Testing programs

Before each test, the specimen is fully compressed along y-direction to reach the single variant state with the short-axis (c-axis) along y-direction (so-called stress-preferred martensite variant, shown as M1 in Fig. 2.1(b)), which is the reference state (i.e., zero strain) for the calculation of the specimen deformation strain in this chapter. Note that the austenite phase is $L2_1$ cubic with a lattice constant of a_0 and the martensite variants are slightly monoclinic, but here we assume that they are tetragonal with two long axes "a" and one short axis "c" for the simplicity of the analysis. At the beginning of each test, an initial compressive stress σ_{ini} is applied on the specimen by compressing a spring with the aid of a micrometer screw (see Fig. 2.1(a)). Then a magnetic field of certain frequency f_{mag} is applied to drive the cyclic martensite reorientation between M1 and M2 (so-called field preferred variant with the short axis along x-direction) as shown in Fig. 2.1(b). During the martensite reorientation, the specimen length changes, leading to a change in the spring length so that the compressive stress also changes. The interaction between the cyclic magnetic field and the evolving compressive stress eventually leads to the cyclic martensite reorientation between the martensite variants M1 and M2. According to previous literature (Heczko et al., 2002; Murray et al., 2000; Straka et al., 2006), the typical lattice parameters $a \approx 0.595$ nm and $c \approx 0.561$ nm for 10M martensite and $a_0 \approx 0.584$ nm for cubic austenite at room temperature. So the strain along y-direction is around 6% when M1 changes to M2 ($(a - c)/c \approx 6\%$) and around 4% when M1 transforms to cubic austenite ($(a_0 - c)/c \approx 4\%$). It is noted that the lattice parameters are temperature dependent (Glavatska et al., 2002; Pagounis et al., 2014; Straka et al., 2006), so the strain value is temperature dependent also. However, in the current experiments with the small temperature variation (i.e., from

the room temperature ($\approx$ 20 °C) to the martensite start temperature M_s = 36.4 °C), the temperature-induced variations in the martensite reorientation strain and the phase transformation strain can be ignored.

The long-time dynamic tests (duration time $t \geq 100$ s) were first conducted in the normal ambient condition (i.e., still air at room temperature 20 ± 2 °C) to demonstrate the dependence of the output strain on the magnetic-field frequency f_{mag} (50 Hz ~ 200 Hz) and the initial compressive stress σ_{ini} (0.1 MPa ~ 4 MPa). From these tests, the significant difference in the output strain between the short-time actuation ($t \approx$ 10 s) and the long-time actuation ($t \geq 100$ s) was shown. Secondly, some magneto-mechanical loadings of proper f_{mag} and σ_{ini} (which have the potential to provide large strains) were chosen, and the tests were performed in different ambient conditions (with airflow velocity V_{air} varying from 0 m/s to 60 m/s and airflow temperature was around 16 °C) to study the dependence of the steady-state output strain and the steady-state temperature on the heat exchange efficiency, which can be characterized by the characteristic heat-relaxation time t_h (see the details of the t_h measurement in Chapter 2). The t_h is associated with the airflow velocity: for the airflow velocity V_{air} changing from 60 m/s to 0 m/s, t_h changes correspondingly from 2.2 s to 68.9 s in the current system.

3.3 Experimental results

The results of the tests without and with the ambient airflow are reported in the following two subsections emphasizing the long-time actuation influence and the ambient thermal effect on the dynamic magnetic-field-induced deformation respectively.

3.3.1 Effect of long-time actuation

A typical result of the thermo-mechanical responses of the specimen is demonstrated in Fig. 3.2, where the applied magnetic field frequency f_{mag} is 90 Hz and the initial compressive stress σ_{ini} is 0.4 MPa. It should be noted that all the tests in this subsection were conducted in the still air (i.e., $V_{air} = 0$). The observations of the measured output strain, stress and temperature are given below:

(1) The strain changed cyclically with the magnetic field, and its frequency was two times the magnetic-field frequency: $f_{strain} = 2 \cdot f_{mag} = 180$ Hz as shown in Fig. 3.2(b) for the short-time responses at $t \approx 8$ s and Fig. 3.2(c) for the long-time responses at $t \approx 100$ s. The strain amplitude (the difference between the maximum and the minimum output strains in a cycle) of the short-time actuation (< 10 s) was 5.9%, much larger than that (1.0%) of the long-time actuation (> 100 s). A significant reduction in the strain amplitude (so-called strain drop) occurred at $t = 10 \sim 11$ s. After the strain drop, the output strain amplitude $\Delta\varepsilon$ kept constant until the end of the test: the applied magnetic field was turned off at $t \approx 117$ s, from which the strain gradually decreased to 0.8% since the initial compressive stress of 0.4 MPa was not large enough to completely compress M2 back to M1 in the quasi-static condition.

(2) The stress oscillated at the same frequency as the strain. During the strain drop, the stress amplitude $\Delta\sigma$ (the difference between the maximum and minimum stresses) reduced from 2.8 MPa to 0.8 MPa. Due to the nonlinearity in the stress-strain relation of the martensite reorientation and the inertial effect in the high-frequency dynamic deformation (Henry, 2002; Lai et al., 2008; Pascan et al., 2016;

Techapiesancharoenkij et al., 2011, 2009), the shape of the stress oscillation is different from that of the strain oscillation which is close to sinusoidal wave.

(3) The temperature increased rapidly until the strain drop. Then it slightly decreased and finally reached a stable temperature (i.e., steady-state temperature) T_{stable} of 35.8 °C which is close to the martensitic phase transformation temperatures of the specimen (i.e., M_f = 35.5 °C and M_s= 36.5 °C).

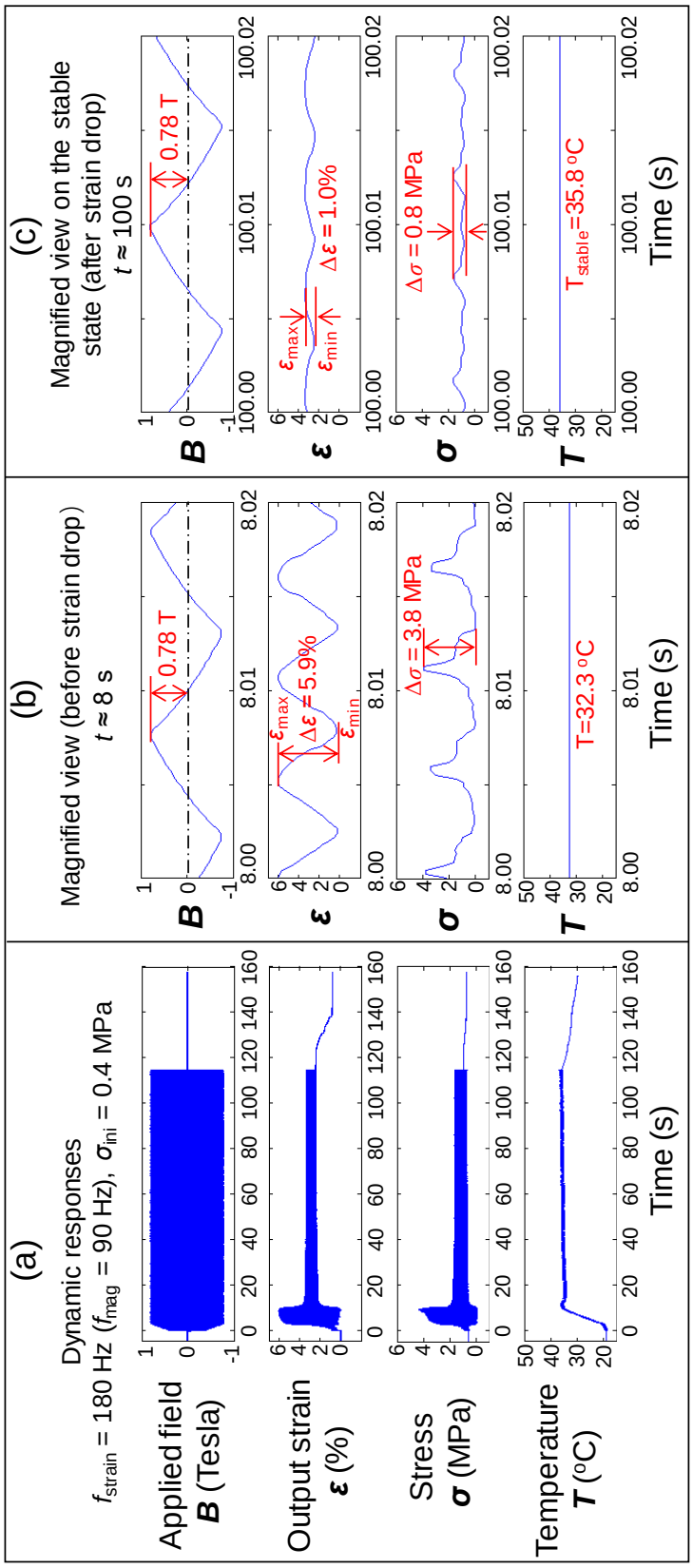

Figure 3.2 Typical responses of strain, stress and temperature of Ni-Mn-Ga specimen under long-time actuation (> 100 s) at the strain frequency f_{strain} = 180 Hz (f_{mag} = 90 Hz): (a) full-time responses, (b) magnified view of the responses before strain drop at $t \approx 8$ s and (c) stable state after the strain drop at $t \approx 100$ s. (d) and (e) are the local-strain fields at the maximum nominal strain ε_{max} and the minimum one ε_{min} for the two typical instants (before and after the strain drop) corresponding to the nominal behaviors shown in (b) and (c), respectively; the strain profiles along the centerline of the specimen are plotted in terms of ε_{yy}-centerline by red lines.

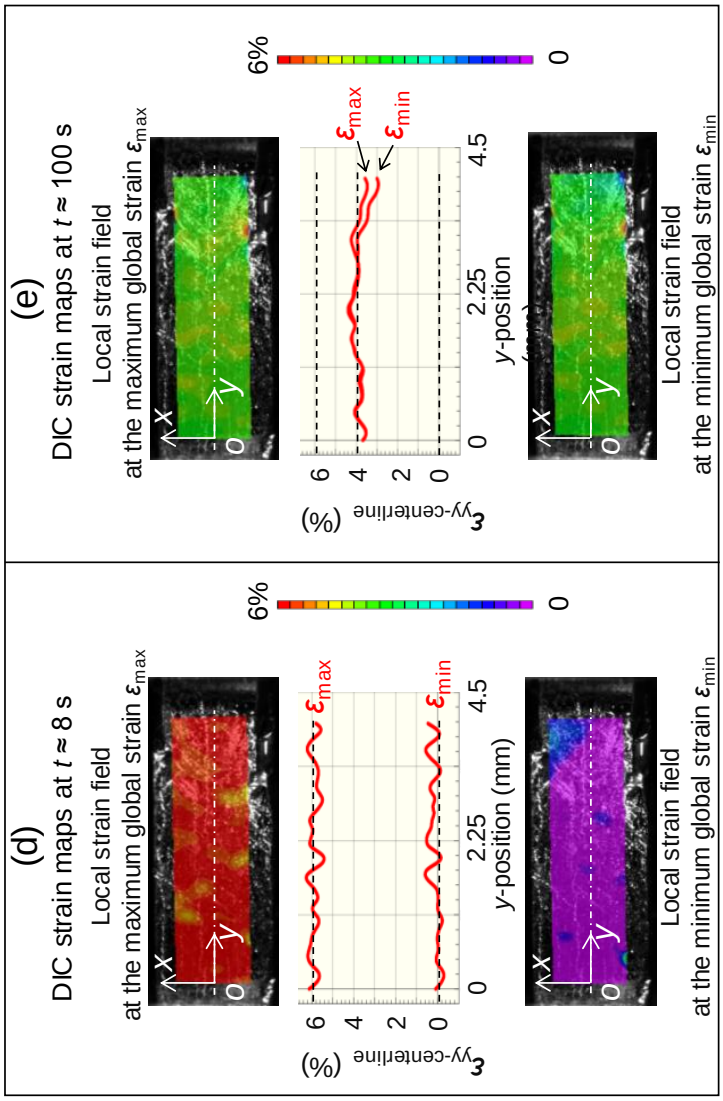

Figure 3.2 Continue.

It is seen from this test that the large temperature increasing rate (around 1.6 °C/s) and the large output strain amplitude ($\Delta\varepsilon$ = 5.9%) during the short-time actuation (< 10 s) cannot be maintained when the temperature increases to a high level at which strain drop takes place. The temperature and the strain amplitude finally reach a steady state (stable for a long time t > 100s), and the steady-state strain amplitude is much smaller than that of the short-time actuation. Such strain drop in the long-time actuation was observed in many tests of various loading conditions such as the ones with different magnetic field frequencies in Fig. 3.3 and the ones with different initial stresses in Fig. 3.4. Table 3.1 summarizes the output strain amplitude $\Delta\varepsilon$ of all the tests (f_{strain} = 100 Hz ~ 400 Hz and σ_{ini} = 0.2 MPa ~ 4 MPa): the values in the small red font are the unstable $\Delta\varepsilon$ before the strain-drop while the values in the big black font are the stable

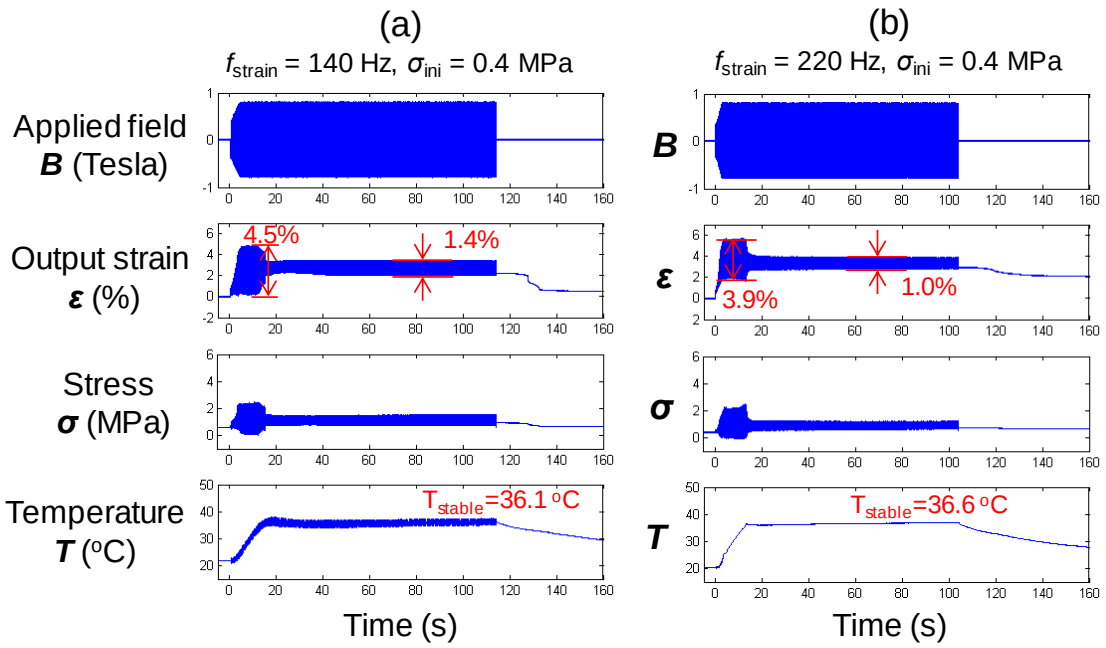

Figure 3.3 Typical responses of the Ni-Mn-Ga specimen under the same initial compressive stress σ_{ini} = 0.4 MPa with different frequency: (a) f_{strain} = 140 Hz (f_{mag} = 70 Hz) and (b) f_{strain} = 220 Hz (f_{mag} = 110 Hz).

$\Delta\varepsilon$ after the strain-drop. The cases with only the values in the big black font show no strain-drop in the actuation. It is seen that almost all the large strain amplitudes (> 1%) are not stable. As an example, the stable and unstable values of $\Delta\varepsilon$ at σ_{ini} = 0.4 MPa in Table 3.1 are plotted in Fig. 3.5. It is confirmed by this figure that in the steady state, only the small strain amplitude (less than 1.5% for cases shown in Fig. 3.5) can be obtained from the current tests conducted in still air (i.e., weak ambient heat exchange). In addition, it's seen from Fig. 3.5 and Table 3.1 that, for a given initial stress, the unstable strain amplitude $\Delta\varepsilon_{unstable}$ depends on the strain frequency non-monotonically (with the maximum strain amplitude at the resonance frequency). This frequency effect in the dynamic actuation of FSMAs has been experimentally observed (Henry, 2002; Lai et al., 2008; Pascan et al., 2016; Techapiesancharoenkij et al., 2011, 2009) and

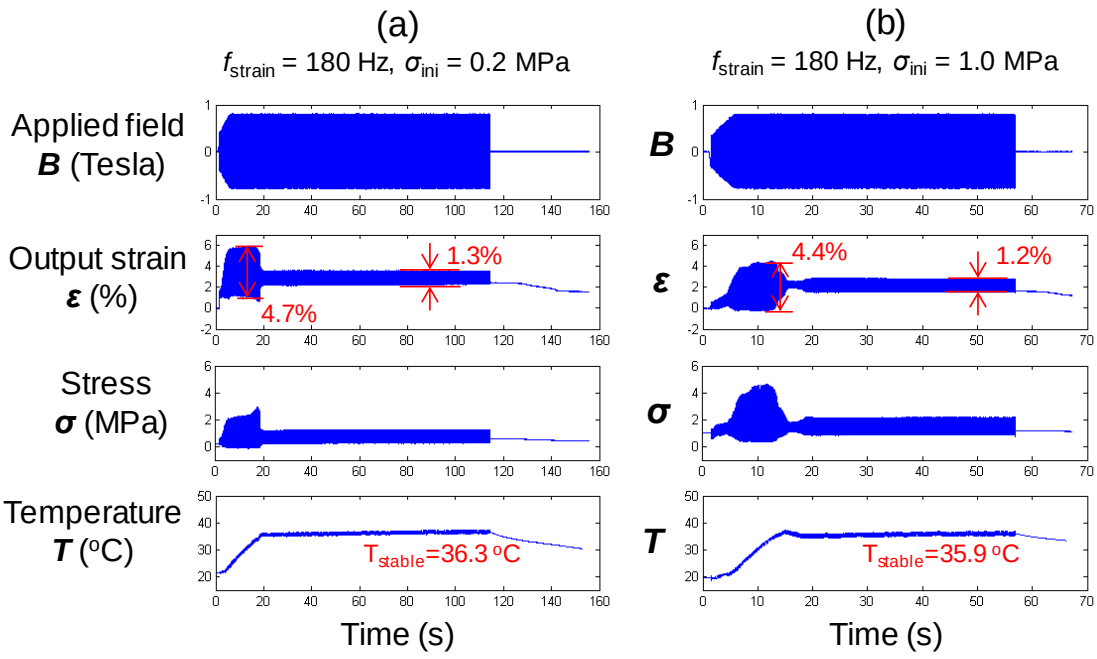

Figure 3.4 Typical responses of Ni-Mn-Ga under the same frequency f_{strain} = 180 Hz (f_{mag} = 90 Hz) with different initial compressive stress: (a) σ_{ini} = 0.2 MPa and (b) σ_{ini} = 1.0 MPa.

Strain amplitude $\Delta\varepsilon$ (%)		Strain frequency f_{strain} (Hz)									
		100	120	140	160	180	200	220	240	300	400
Initial stress σ_{ini} (MPa)	0.2	**2.3**	2.2 ↘ **1.8**	2.6 ↘ **1.5**	4.2 ↘ **1.1**	4.7 ↘ **1.3**	3.7 ↘ **1.2**	3.3 ↘ **1.0**	2.6 ↘ **1.0**	1.1 ↘ **0.4**	1.0 ↘ **0.2**
	0.4	4.2 ↘ **1.3**	4.3 ↘ **1.2**	4.5 ↘ **1.4**	5.2 ↘ **1.2**	5.9 ↘ **1.0**	4.7 ↘ **1.2**	3.9 ↘ **1.0**	2.9 ↘ **1.0**	1.7 ↘ **0.6**	1.1 ↘ **0.4**
	1.0	2.6 ↘ **1.1**	2.8 ↘ **0.8**	3.1 ↘ **0.9**	4.1 ↘ **0.7**	4.4 ↘ **1.2**	5.6 ↘ **0.8**	4.3 ↘ **0.7**	3.8 ↘ **0.6**	2.1 ↘ **0.6**	1.2 ↘ **0.4**
	1.8	**0.8**	**0.8**	**0.5**	**0.5**	**0.5**	**0.6**	**0.6**	**0.5**	0.9 ↘ **0.5**	2.0 ↘ **0.5**
	4.0	**0.2**	**0.2**	**0.1**	**0.2**	**0.3**	**0.1**	**0.1**	**0.1**	**0.2**	**0.2**

Table 3.1 The strain amplitudes of all the tests in the still air ambient at different strain frequencies and initial compressive stresses. The strain amplitudes appearing during the short-time actuation (before the strain drop) are highlighted in red.

theoretically modelled by considering the inertial effect of the dynamic systems (Faran et al., 2017; Faran and Shilo, 2016; Henry, 2002; Sarawate and Dapino, 2008; Tan and Elahinia, 2008).

The stable temperature (steady-state temperature) of all the tests are summarized in Fig. 3.6. It is seen that all the cases with the strain-drop behavior (marked by the red dashed rectangle) have the stable temperatures around the martensitic transformation temperatures (M_s or M_f) while those without the strain-drop behavior have the stable temperatures well below M_f. This implies that the strain-drop is caused by the temperature-induced Martensite-to-Austenite phase transformation. When the temperature at some local positions of the specimen reaches the phase transformation temperature (A_s or A_f), the material transforms from M-phase to A-phase at these positions. Then these positions contribute little to the nominal cyclic strain. The appearance of A-phase during strain-drop can also be confirmed by the local strain field evolution of the specimen based on the in-situ optical observation and the associated DIC strain maps.

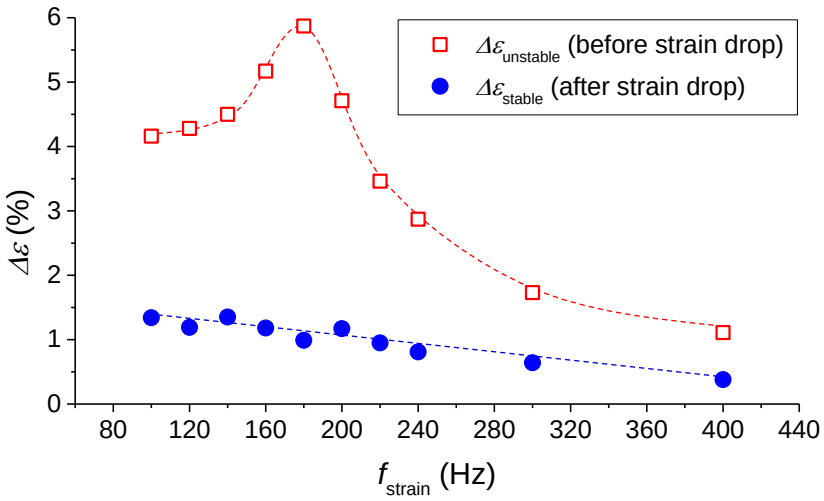

Figure 3.5 The frequency-dependent stable and unstable strain amplitudes of the tests with the initial compressive stress σ_{ini} = 0.4 MPa in still air. $\Delta\varepsilon_{unstable}$ and $\Delta\varepsilon_{stable}$ represent the strain amplitudes of the short-time actuation (before strain drop) and the long-time actuation (after strain drop), respectively. The dashed lines are for guiding eyes.

The local strain fields at two typical instants (before and after the strain drop) are shown in Figs. 3.2(d) and (e), which correspond to the nominal strain oscillations in Figs. 3.2(b) and (c), respectively. It should be noted that all the local strains are calculated with respect to the pre-compressed state (stress-preferred variant M1 with the short axis c along y-direction). It is seen from Fig. 3.2(d) that the local strains of all the material points in the gauge section change to around 6% when the nominal strain reaches ε_{max} (which means that all the material becomes the field-preferred martensite variant M2), and around 0% when the nominal strain reaches ε_{min} (all the material returns to the stress-preferred martensite variant M1). The combination of Figs. 3.2(b) and (d) indicates that a cyclic complete martensite reorientation with the nominal strain 5.9% is achieved in the whole specimen before the strain drop (i.e., all the material points in the specimen are taking cyclic martensite reorientation).

By contrast, the local strain distributions in Fig. 3.2(e) show that almost all the points in the gauge section have a constant local strain around 4% when the specimen responses reach the stable state (after the strain drop as shown in Fig. 3.2(c)). This indicates that the applied cyclic magnetic field cannot drive the martensite reorientation in these zones (non-active zone with constant local strain). Based on the fact that the theoretical strain of the Austenite phase with respect to the Martensite variant M1 is 4% in the specimen as calculated in Section 3.2, it's implied that the material points in the non-active zones (with constant local strain 4%) are in the state of A-phase, thus not sensitive to the applied cyclic magnetic field (contributing little to the nominal cyclic strain). Combining the nominal strain oscillation in Fig. 3.2(c), the local strain distribution in Fig. 3.2(e) and the steady-state temperature around M_s and M_f in Fig. 3.6, we can conclude that the strain-drop behavior is caused by the temperature-rise

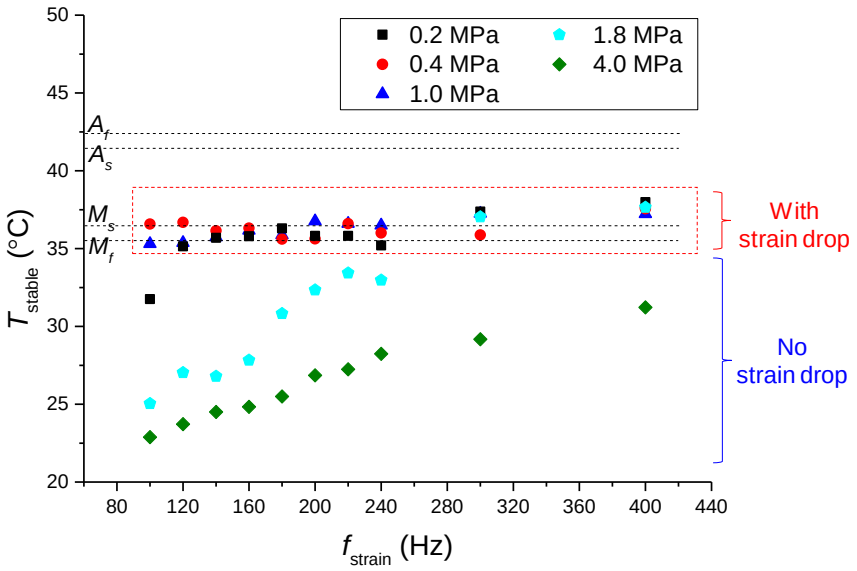

Figure 3.6 Stable temperatures T_{stable} of all tests conducted in still air with different loading conditions (different strain frequencies and initial compressive stresses). The cases with strain drop are marked by the red dashed rectangle.

induced Martensite-to-Austenite phase transformation, and A-phase is non-active under the current weak magnetic field.

3.3.2 Effect of the ambient heat exchange

To avoid the large temperature rise (so as to avoid the strain-drop due to phase transformation), strong ambient airflows were forced to pass through the specimen during the long-time actuation tests shown in Figs. 3.7(a), (b) and (c) (all these tests were conducted at f_{strain} = 180 Hz and σ_{ini} = 0.4 MPa) where the air velocity V_{air} is 60 m/s, 35 m/s and 15 m/s, respectively (the characteristic heat-relaxation time t_h is 2.2 s, 4.2 s and 8.8 s correspondingly). It is seen that their stable temperatures are 18.3 °C, 24.5 °C and 33.8 °C, well below M_f so that there is no phase transformation (no strain-drop process) in these tests. It is also noted that the stable strain amplitude $\Delta\varepsilon_{stable}$ increases from 1.5% to 5.4% when the air velocity V_{air} decreases from 60 m/s to 15 m/s (or when the stable temperature T_{stable} increases from 18.3 °C to 33.8 °C). The reason for such temperature dependence or the airflow dependence will be discussed in Section 3.4.

By contrast, when only a weak airflow was applied, the temperature rise is still high enough to trigger the strain-drop process (the phase transformation) as shown in Figs. 3.7(d), (e) and (f) where $\Delta\varepsilon_{stable}$ = 3.6%, 2.5% and 1.0% with the airflow velocity V_{air} = 8 m/s, 3 m/s and 0 m/s (still air), respectively. The corresponding characteristic heat-relaxation time t_h = 14.0 s, 22.2 s and 68.9 s. It is seen that the stable temperatures of the three cases are 34.9 °C, 35.9 °C and 36.1 °C; all are close to M_f and M_s.

Figure 3.8 summarizes the stable strain amplitude and the stable temperature ($\Delta\varepsilon_{stable}$ and T_{stable}) of the systematic tests at different levels of the ambient airflow

velocity V_{air} (also the corresponding characteristic heat-relaxation time t_h). It is seen that $\Delta\varepsilon_{stable}$ and T_{stable} changes non-monotonically with t_h (or V_{air}). The maximum strain amplitude can be achieved at $t_h^* \approx 8.8$ s for $f_{strain} = 180$ Hz in Fig. 8(a) and at $t_h^* \approx 11.7$ s for $f_{strain} = 220$ Hz in Fig. 3.8(b). For both frequencies, the stable temperature T_{stable} increases with increasing t_h (decreasing V_{air}) and the saturated temperature is at around 36 °C when t_h is large enough (i.e., when the airflow is weak). Two important conclusions can be obtained from Fig. 3.8:

(1) Optimal condition of heat exchange to achieve the largest stable strain amplitude: For a given magneto-mechanical loading of f_{mag} (=$f_{strain}/2$) and σ_{ini}, a proper ambient condition (e.g. with a proper value of t_h (or V_{air})) setting the stable temperature of the specimen close to (but lower than) M_f without triggering the Martensite-to-Austenite phase transformation can lead to the maximum stable strain amplitude of the specimen, e.g., $t_h^* = 8.8$ s in Fig. 3.8(a) and 11.7 s in Fig. 3.8(b).

(2) A special "isothermal" FSMA actuator with tunable output strain amplitude by ambient heat exchange can be developed: In the range of weak ambient heat exchange (i.e., $t_h > 8.8$ s in Fig. 3.8(a) and $t_h > 11.7$ s in Fig. 3.8(b)), the specimen's stable strain amplitude can be adjusted by controlling t_h (or V_{air}) while keeping its stable temperature constant around M_f, e.g., see the red circle points in Figs. 3.8(a) and 3.8(b). The understanding and modeling on these behaviors are discussed in the next section.

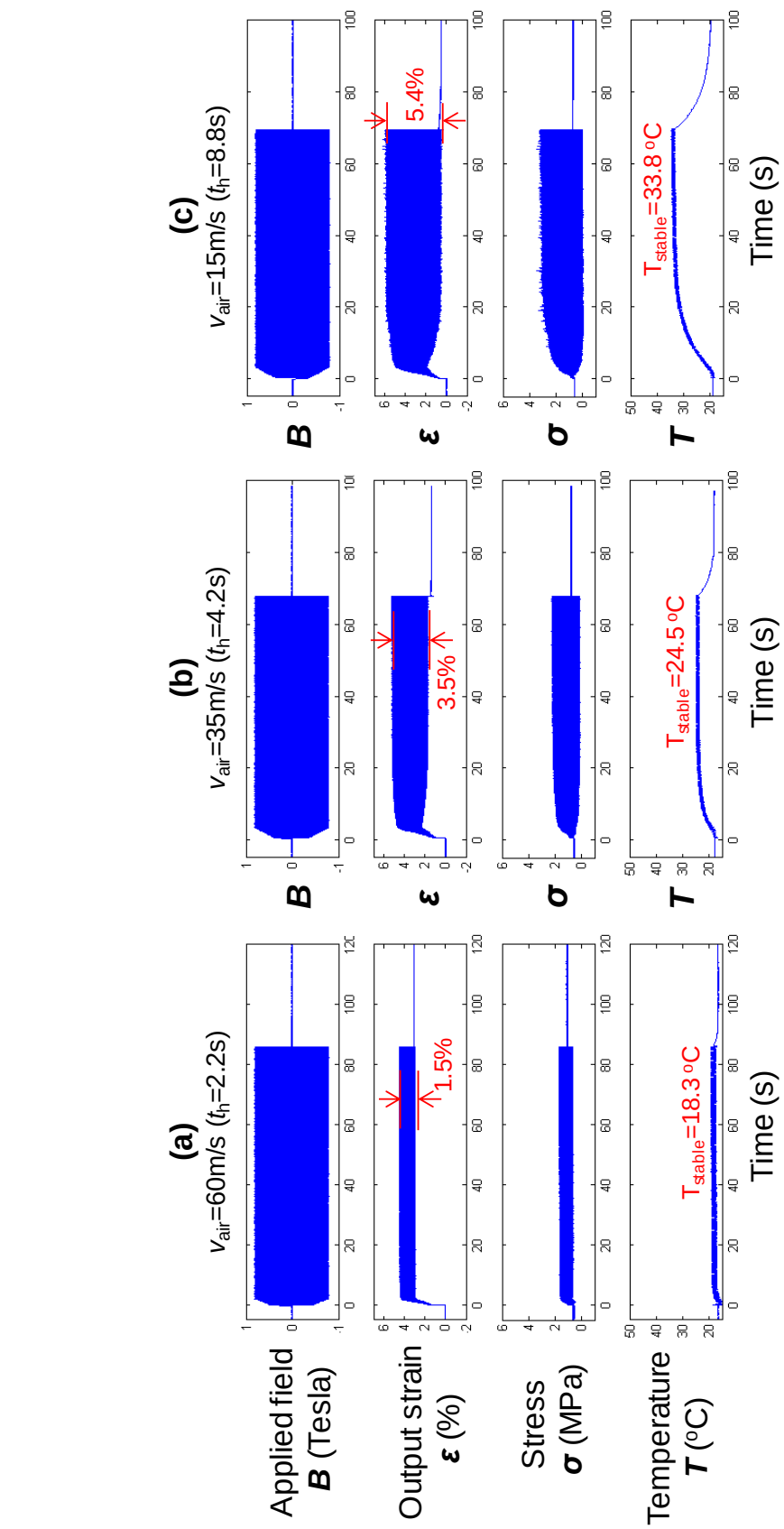

Figure 3.7 The responses of the tests at different levels of ambient airflow velocity: (a) ~ (f) are respectively for the air velocity V_{air} = 60 m/s (t_h = 2.2 s), 35 m/s (t_h = 4.2 s), 15 m/s (t_h = 8.8 s), 8 m/s (t_h = 14.0 s), 3 m/s (t_h = 22.2 s) and 0 m/s (t_h = 68.9 s). All the tests are conducted at the same magneto-mechanical loading conditions of f_{strain} = 180 Hz (f_{mag} = 90 Hz) and σ_{ini} = 0.4 MPa.

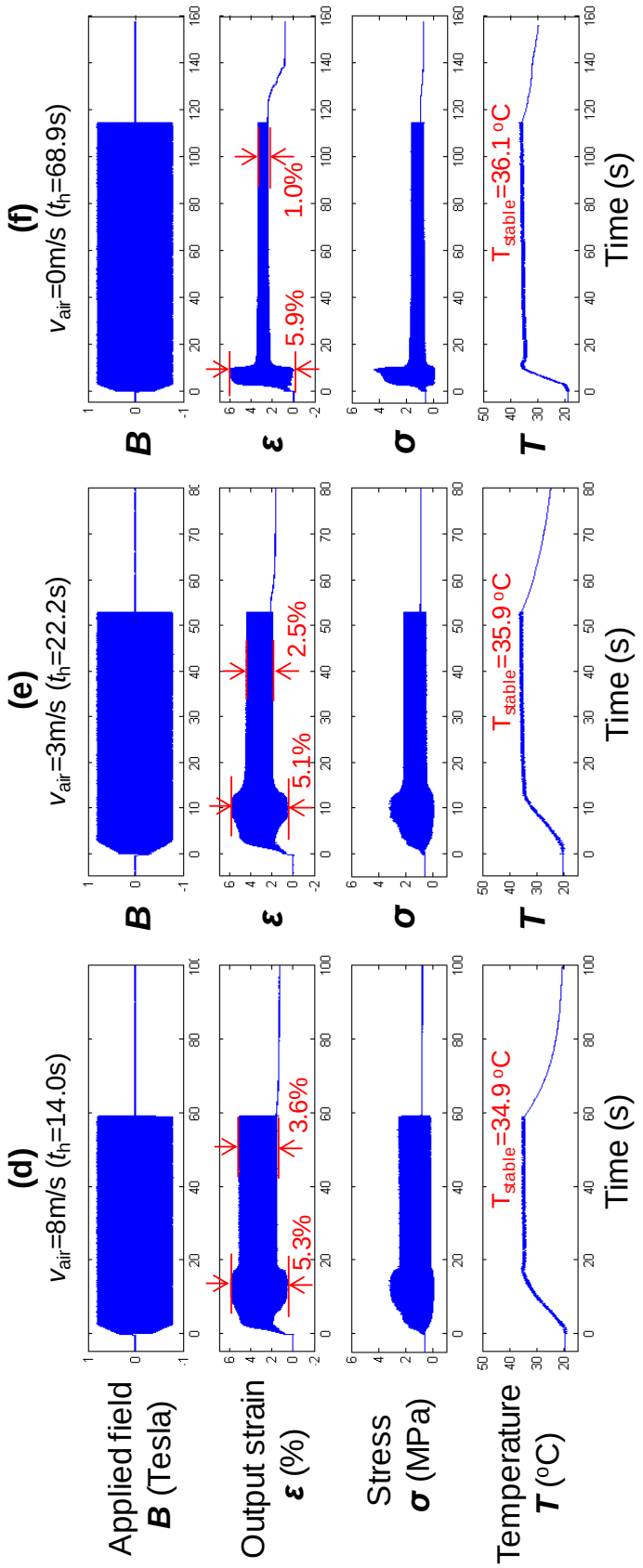

Figure 3.7 Continue.

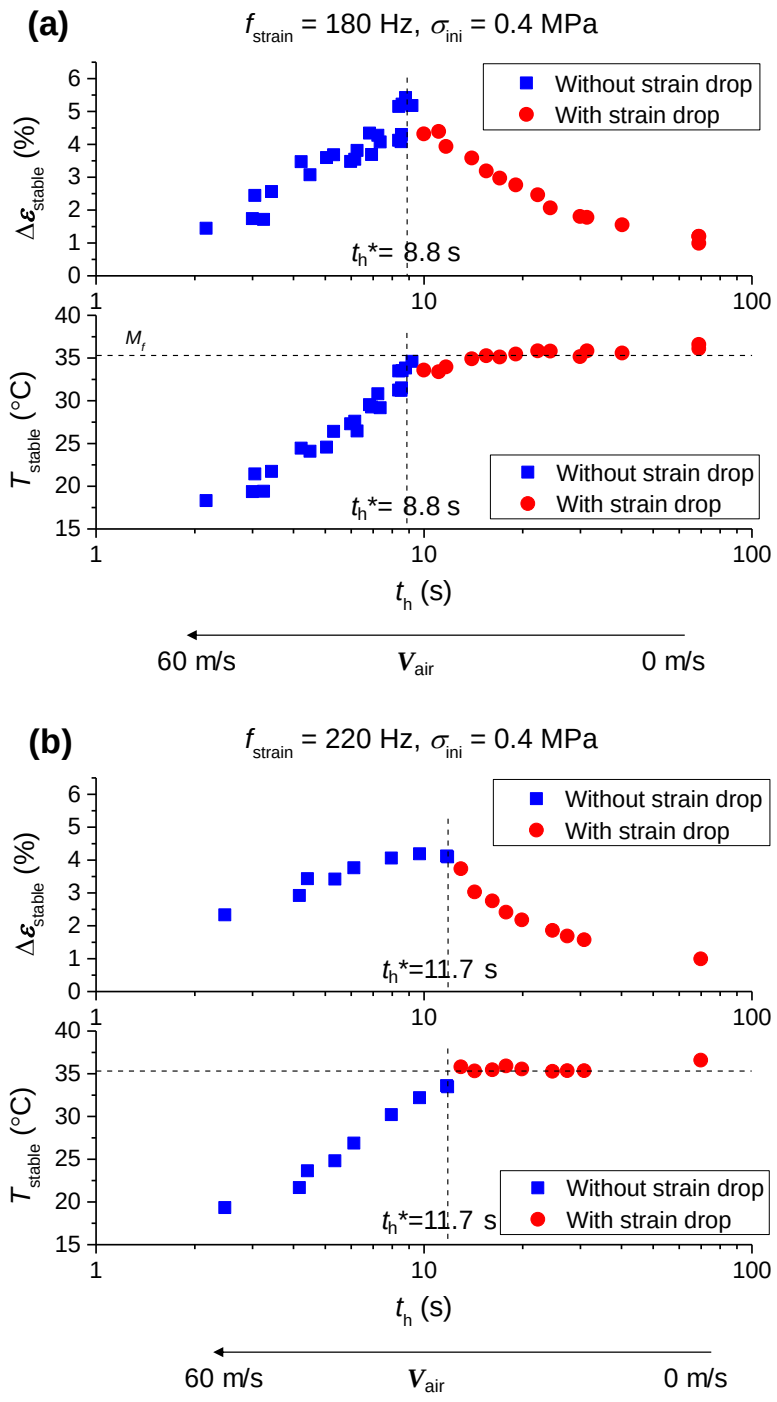

Figure 3.8 Airflow-dependence (t_h-dependence) of the stable strain amplitude $\Delta\varepsilon_{stable}$ and the stable temperature T_{stable} for all the tests with ambient airflow of different velocities for the two typical loading frequencies: (a) f_{strain} = 180 Hz and (b) f_{strain} = 220 Hz.

3.4 Theoretical study on the effect of ambient heat exchange

In this section, we discuss first the mechanisms for the non-monotonic dependence of the output stable strain on the ambient air velocity, and then the optimal conditions to achieve a large stable strain.

3.4.1 Non-monotonic dependence of stable strain amplitude on ambient airflow

Both the $\Delta\varepsilon_{stable} - t_h$ curves and the $T_{stable} - t_h$ curves in Fig. 3.8 can be divided into two regions: the region of strong heat exchange ($t_h < t_h^*$ where there is no strain drop and the stable temperature increases with t_h) and the one of weak heat exchange ($t_h > t_h^*$ where the strain drop takes place and the temperature keeps constant). That means the heat-relaxation time t_h-dependences in these two regions should be governed by different mechanisms, which will be discussed respectively in the following two subsections.

3.4.1.1 Region of strong ambient heat exchange (without phase transformation)

As the heat exchange has important effects on the temperature rise and the stable strain, a heat-transfer model is adopted to facilitate the following analysis and discussion. The FSMA specimen is modeled as a one-dimension (1D) bar shown in Fig. 3.9. The temperature evolution of an elementary length dx of the bar during the cyclic martensite

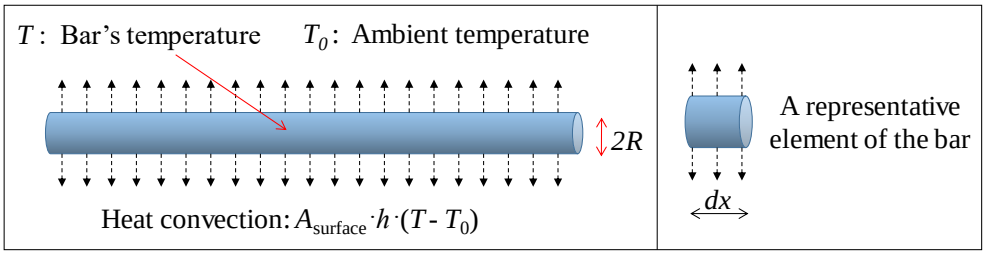

Figure 3.9 One-dimensional heat-transfer model

reorientation can be calculated by the following heat balance equation (Bruno et al., 1995; He and Sun, 2011; Pascan et al., 2015):

$$\lambda \cdot \pi R^2 \cdot dx \cdot dT = q \cdot \pi R^2 \cdot dx \cdot dt - 2\pi R \cdot dx \cdot h \cdot (T - T_0) \cdot dt, \tag{3.1}$$

where the parameters T_0, R, λ, q and h denote the ambient temperature, the radius of the bar, the material heat capacity per unit volume, the heat generation rate and the heat convection coefficient, respectively. The temperature of the bar is assumed to be uniform, only depends on time: $T(t)$. Heat conduction is neglected in Eq. (3.1), and we can further reduce this equation to

$$\frac{dT}{dt} = \frac{q}{\lambda} - \frac{2h}{\lambda \cdot R} \cdot (T - T_0). \tag{3.2}$$

There are two contributions to the heat generation rate q ($\mathrm{J{\cdot}m^{-3}{\cdot}s^{-1}}$): (1) q_{TB} (= $2\sigma_{tw} \cdot \Delta\varepsilon \cdot f_{strain}$) from the martensite reorientation (with σ_{tw} being the twinning stress) and (2) the energy dissipation from the field-induced eddy current inside the specimen q_{eddy}. The details about the measurement on the eddy-current dissipation can be found in the following, where q_{eddy} has a relation with the strain frequency by data fitting:

$q_{eddy} = 2320.7 \cdot f_{strain} - 1.35 \times 10^5$ (J·m^{-3}·s^{-1}) for the current system with the strain frequency f_{strain} in the range of [100 Hz, 400 Hz]. By introducing $q = q_{TB} + q_{eddy}$ into Eq. (3.2), we obtain:

$$\begin{aligned} \frac{dT}{dt} &= \frac{q_{TB} + q_{eddy}}{\lambda} - \frac{2h}{\lambda \cdot R} \cdot (T - T_0) \\ &= \frac{q_{TB} + q_{eddy}}{\lambda} - \frac{1}{t_h} \cdot (T - T_0), \end{aligned} \tag{3.3}$$

where $t_h = \dfrac{R \cdot \lambda}{2h}$ is the characteristic heat-relaxation time, which can be measured by the heat-relaxation experiments as shown in Section 2.2.

- **Measurement of the heat release from eddy current**

  The temperature rise during the dynamic actuation of FSMA is attributed to both the energy dissipation of the frictional twin boundary motion and the eddy current (Henry, 2002; Lai, 2009). In order to quantify and compare the contributions from these two mechanisms separately, we conducted the tests with different initial stresses as shown in Fig. 3.10. When the initial compressive stress σ_{ini} = 0.4 MPa (Fig. 3.10(a)), the strain amplitude is large ($\Delta\varepsilon$ = 5.9% at actuation time t = 0 ~ 10 s) and the temperature increases rapidly (with the increasing rate around 1.6 °C/s). By contrast, when σ_{ini} = 4.0 MPa (which is larger than the so-called "blocking stres" (Heczko et al., 2000)), the output strain amplitude is zero (i.e., no martensite reorientation) as shown in Fig. 3.10(b) where the temperature rise purely induced by the eddy current is very slow. The temperature increasing rate is around 0.04 °C/s at t = 0 ~ 10 s, which is much smaller than that with the large $\Delta\varepsilon$ from martensite reorientation in Fig. 3.10(a).

  Similar to the test in Fig. 3.10(b) showing the eddy-current effect, we did more

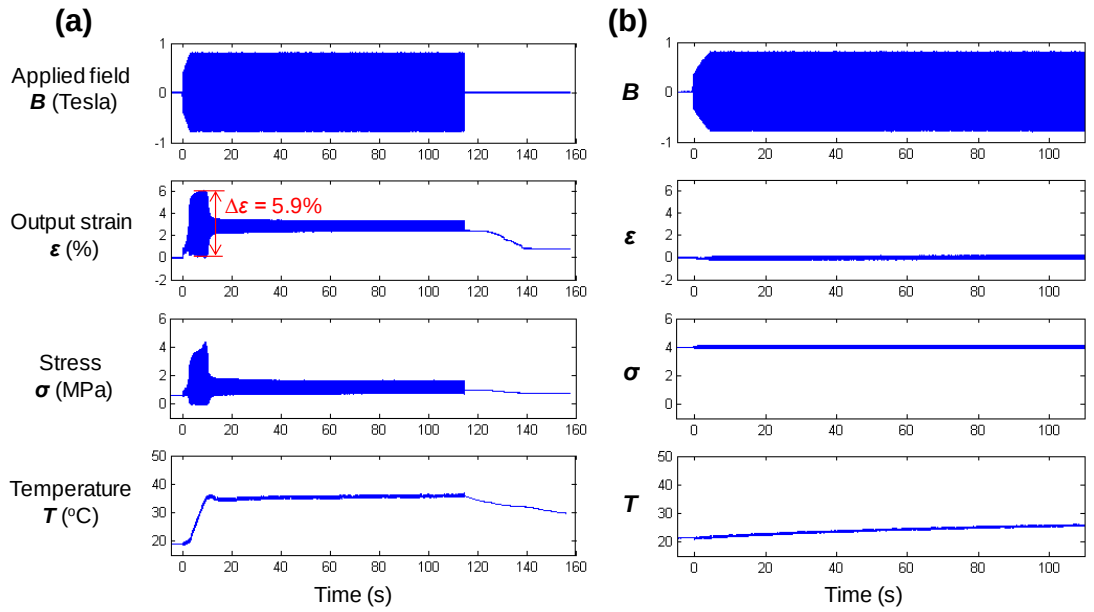

Figure 3.10 Typical tests to compare the temperature rises induced by the martensite-reorientation dissipation and the eddy current at the strain frequency f_{strain} = 180 Hz, with the different initial compressive stresses: (a) 0.4 MPa and (b) 4.0 MPa.

tests of different frequencies with the same initial stress σ_{ini} = 4.0 MPa. The frequency dependence of the eddy-current induced temperature rise after 100 s actuation Δ_{eddy}^{100s} is shown in Fig. 3.11(a). As the material specific heat capacity per unit volume $\lambda = 4 \times 10^6$ J · m^{-3} · K^{-1}, the heat release rate due to the eddy current can be determined (from Eq. (3.5) by setting $q_{TB} = 0$) as

$$q_{eddy} = \frac{\Delta_{eddy}^{100s} \cdot \lambda}{t_h \cdot (1 - e^{-\frac{100}{t_h}})} \quad (\mathrm{J \cdot m^{-3} \cdot s^{-1}}),$$

where the characteristic heat-relaxation time t_h is 68.9 s in the still air. Figure 3.11(b) summarizes the frequency dependence of q_{eddy}, which is approximately fitted by a linear relation $q_{eddy} = 2320.7 \cdot f_{strain} - 1.35 \times 10^5$ (J · m^{-3} · s^{-1}) in the strain frequency range [100 Hz, 400 Hz].

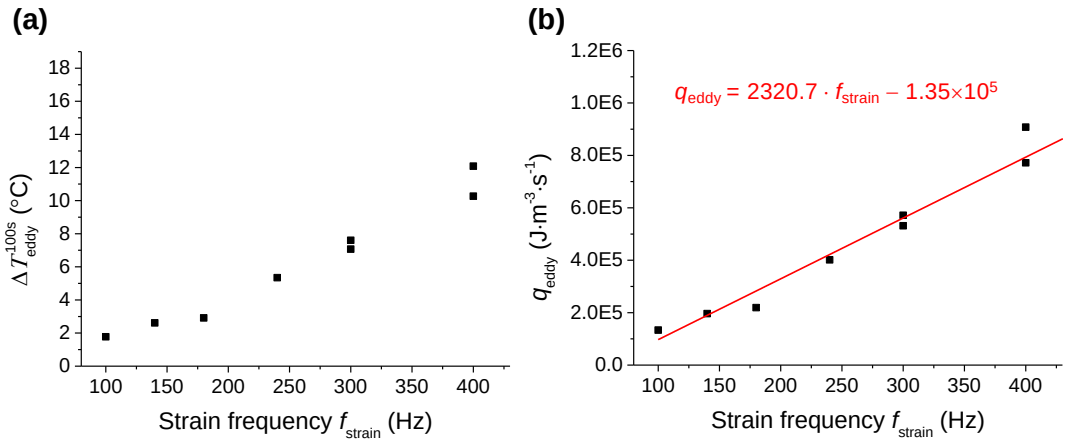

Figure 3.11 The temperature rise due to eddy current after the actuation of 100 s at different strain frequencies f_{strain} are shown in (a) and the corresponding heat generation rate is shown in (b).

The solution to Eq. (3.3) is

$$T = T_0 + \frac{q_{TB} + q_{eddy}}{\lambda} \cdot t_h \cdot (1 - e^{-\frac{t}{t_h}}). \tag{3.4}$$

Then the temperature rise ΔT can be obtained from Eq. (3.4) as:

$$\Delta T = T - T_0 = \frac{q_{TB} + q_{eddy}}{\lambda} \cdot t_h \cdot (1 - e^{-\frac{t}{t_h}}). \tag{3.5}$$

Equation (3.5) can be used to describe the temperature rise observed in the experiments. Taking the test in Fig. 3.7(c) as an example, with $\Delta\varepsilon = 5.4‰$, $t_h = 8.8$ s, $f_{strain} = 180$ Hz, $\sigma_{tw} = 0.35$ MPa and $\lambda = 4 \times 10^6$ J · m^{-3} · K^{-1}, we plot Eq. (3.5) in Fig. 3.12. It's seen that Eq. (3.5) agrees well with the experimental data.

The more important capability of this heat-transfer model is to predict the steady-state responses. By taking t to be infinity in Eq. (3.5), we obtain the stable temperature

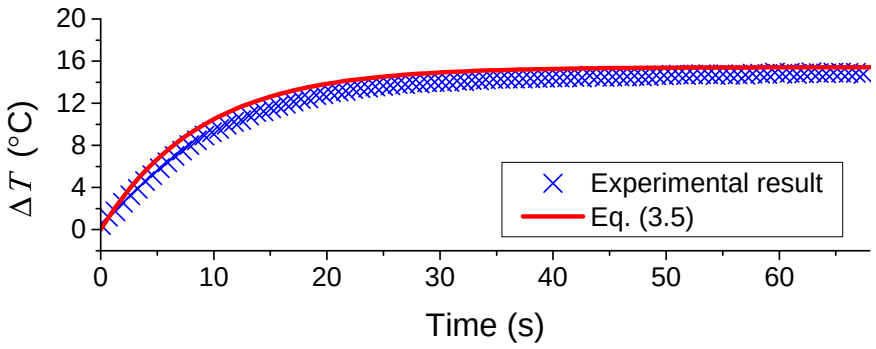

Figure 3.12 Comparison of the temperature rise between Eq. (3.5) and the experimental data from the test of f_{strain} = 180 Hz, σ_{ini} = 0.4 MPa and V_{air} = 15m/s (t_h = 8.8s), whose responses of the strain and the stress can be found in Fig. 3.7(c).

T_{stable} as:

$$\Delta T_{stable} = T_{stable} - T_0 = \frac{t_h \cdot q_{stable}}{\lambda}, \tag{3.6}$$

where $q_{stable} = 2\sigma_{tw} \cdot \Delta\varepsilon_{stable} \cdot f_{strain} + q_{eddy}$. It is seen that the stable temperature is related to the stable strain amplitude. In this equation, only twinning stress cannot be directly measured. The twinning stresses of Type I and Type II twin boundaries are different in value in Ni-Mn-Ga single crystal. Moreover, their temperature dependence are also different, e.g., the two shaded zones in Fig. 3.13 represent the ranges of the experimental measured temperature-dependent twinning stresses in the literature (Heczko and Straka, 2003; Soroka et al., 2018; Sozinov et al., 2017; Straka et al., 2012; Zreihan et al., 2015): the twinning stress of Type II twin boundary is independent of temperature while that of Type I decreases linearly with temperature:

$$\sigma_{tw}^{I} = 0.2 - 0.04 \cdot (T - A_s) \ \text{(MPa)}, \tag{3.7a}$$

$$\sigma_{tw}^{II} = 0.2 \ \ \text{(MPa)}. \tag{3.7b}$$

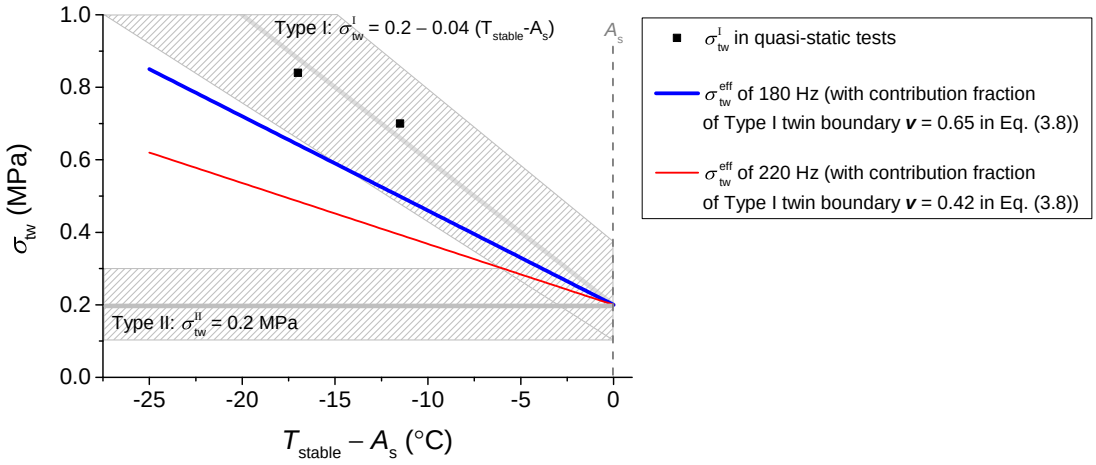

Figure 3.13 The temperature dependence of twinning stress for the twin boundary motion during the magneto-mechanically driven martensite reorientation. The two shaded regions represent the temperature dependence of the twinning stresses of the Type I and Type II twin boundaries, respectively, reported in (Heczko and Straka, 2003; Soroka et al., 2018; Sozinov et al., 2017; Straka et al., 2012; Zreihan et al., 2015). The thick blue and thin red lines (determined by Eq. (3.8) with ν = 0.65 and 0.42 respectively) represent the temperature dependences of the effective twinning stress of the mixed Type I and Type II twin boundaries in the dynamic actuation of f_{strain} = 180 Hz and f_{strain} = 220 Hz, respectively.

In the high-frequency magnetic-field-induced martensite reorientation, both Type I and II twin boundaries can be nucleated (Pascan et al., 2015). Therefore, the effective twinning stress (corresponding to the effective energy dissipation) should include the contributions from both types of twin boundaries:

$$\begin{aligned}\sigma_{tw}^{eff} &= \nu \cdot \sigma_{tw}^{I} + (1-\nu) \cdot \sigma_{tw}^{II} \\ &= \nu \cdot [0.2 - 0.04 \cdot (T - A_s)] + (1-\nu) \cdot 0.2 \\ &= 0.2 - 0.04 \cdot \nu \cdot (T - A_s),\end{aligned} \tag{3.8}$$

where ν denotes the contribution fraction of type I twin boundary. Substituting Eq. (3.8) into Eq. (3.6), we obtain the following relation between the stable temperature and the stable strain amplitude:

$$\begin{aligned}&T_{stable} - T_0 \\ &= \frac{t_h}{\lambda} \cdot \left\{2 \cdot \Delta\varepsilon_{stable} \cdot f_{strain} \cdot [0.2 - 0.04 \cdot \nu \cdot (T_{stable} - A_s)] + q_{eddy}\right\} \\ &= \frac{t_h}{\lambda} \cdot \{2 \cdot \Delta\varepsilon_{stable} \cdot f_{strain} \cdot [0.2 - 0.04 \cdot \nu \cdot (T_{stable} - A_s)] \\ &+ (2320.7 \cdot f_{strain} - 1.35 \times 10^5),\end{aligned} \tag{3.9a}$$

$$\Longrightarrow \Delta\varepsilon_{stable} = \frac{\left[\dfrac{(T_{stable} - T_0) \cdot \lambda}{t_h} - (2320.7 \cdot f_{strain} - 1.35 \times 10^5)\right]}{2 \cdot f_{strain} \cdot [0.2 - 0.04 \cdot \nu \cdot (T_{stable} - A_s)]}. \tag{3.9b}$$

In Eq. (3.9b), only the fraction ν cannot be directly measured; but it can be determined by data fitting of the tests without strain drop ($t_h < t_h^*$). Because the

specimen temperature T_{stable} also depends on t_h for these tests, we first obtain the relation between T_{stable} and t_h by fitting (see inset figures in Figs. 3.14(a) and 3.14(c) for f_{strain} = 180 Hz and 220 Hz respectively). Then the $T_{stable} - t_h$ relation is substituted into Eq. (3.9b) to compare with the experimental data and to further determine the parameter ν. We find that ν = 0.60 and 0.38 respectively for f_{strain} = 180 Hz and 220 Hz can make Eq. (3.9b) best fit with the experimental data in terms of $\Delta\varepsilon_{stable}$ and $(T_{stable} - A_s)$ in Figs. 3.14(a) and 3.14(c). That means the fraction ν of Type I twin boundary depends on the loading frequency. It is true for the current system and the previous study (Pascan et al., 2015) that Type I twin boundary is dominant ($\nu \approx 1$) when the actuation frequency is very low, near the quasi-static case.

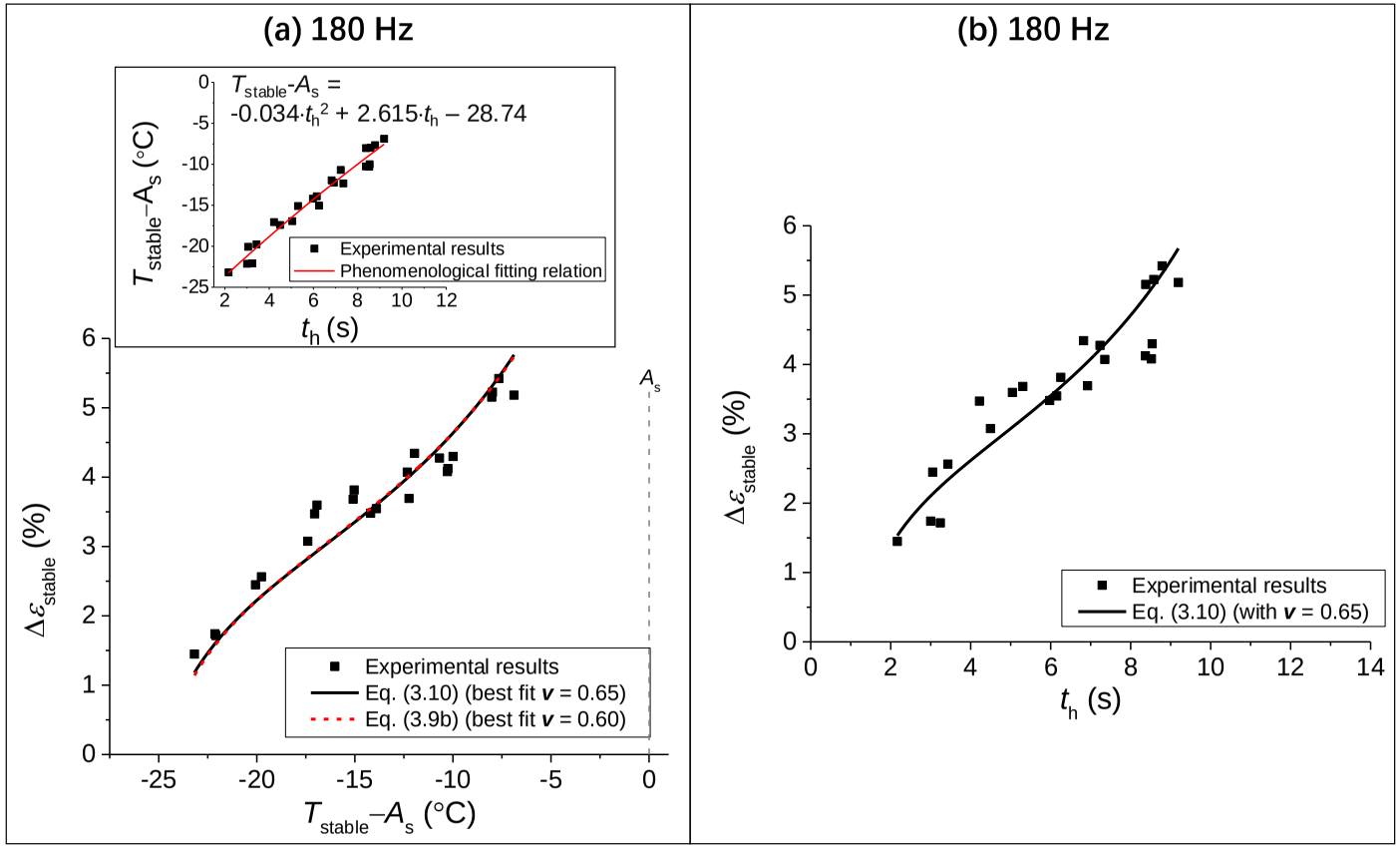

Figure 3.14 Comparison between the experiments (from the tests without strain drop ($t_h < t_h^*$) in Fig. 3.8) and the model (Eq. ((3.9)b) and Eq. (3.10) with and without considering eddy-current effect respectively) to estimate the contribution fraction (ν) of Type I twin boundary during the dynamic martensite reorientation process. (a) and (b) are respectively the dependence of stable strain amplitude $\Delta\varepsilon_{stable}$ on ($T_{stable} - A_s$) and t_h at f_{stain} = 180 Hz; (c) and (d) are respectively the dependence of stable strain amplitude $\Delta\varepsilon_{stable}$ on ($T_{stable} - A_s$) and t_h at f_{stain} = 220 Hz. The relations between ($T_{stable} - A_s$) and t_h are plotted in the insets of (a) and (c).

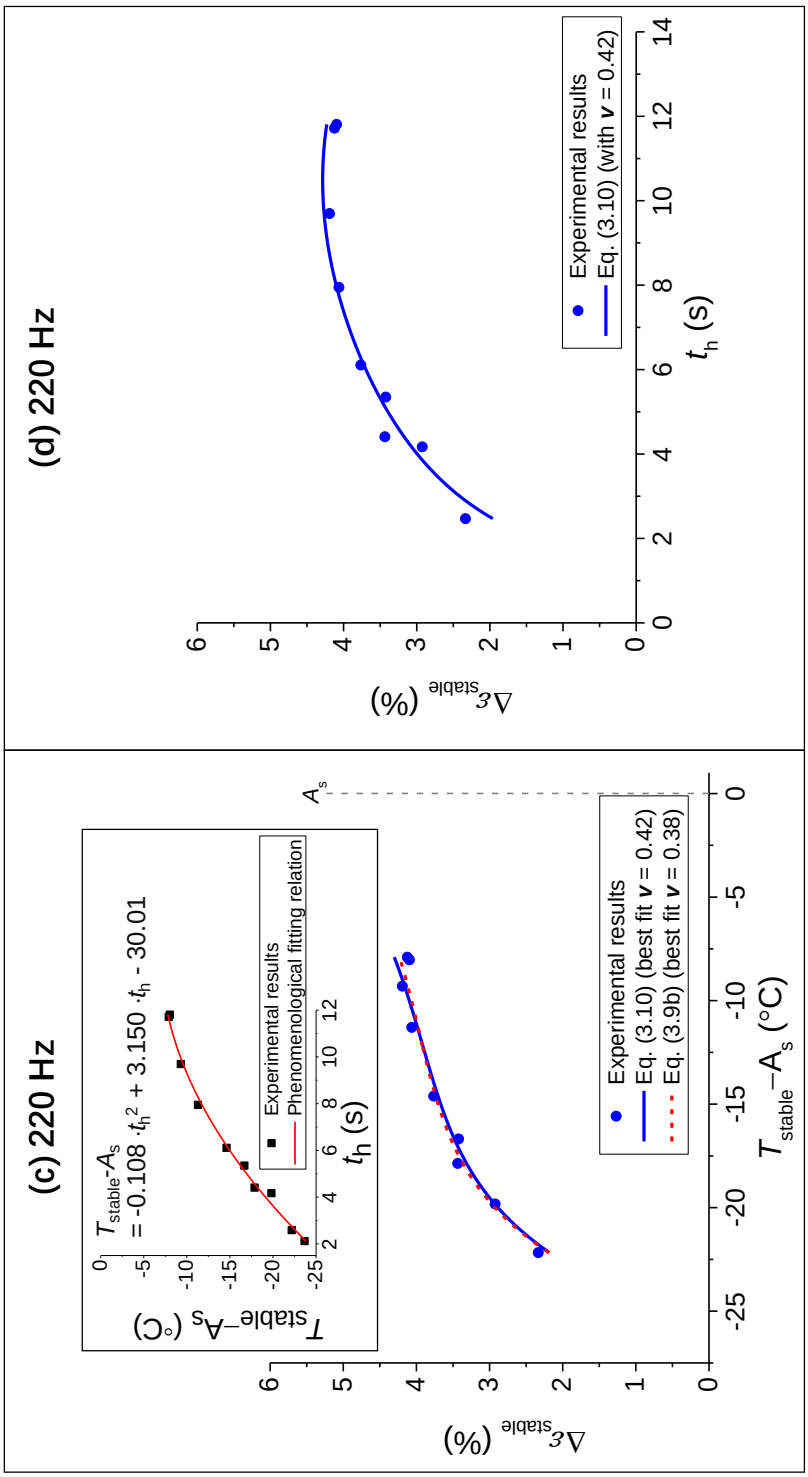

Figure 3.14 Continue.

Figures 3.14(a) and 3.14(c) also indicate that the eddy-current effect is negligible in the tests by the comparison between the best fitting curves of the model including the eddy-current effect (Eq. (3.9b)) and that of the model excluding the eddy-current effect (Eq. (3.10) which can be derived from Eq. (3.9b) by setting $q_{eddy} = 0$). It is seen that the best fitting curves with and without the eddy current overlap and the best fitting values of ν are close to each other. Detailed experimental quantification of the eddy current effect and its comparison with the dissipation of martensite reorientation can be found in Section 3.4.1. Therefore, we ignore the eddy current effect in the following analysis. The best fitting of Eq. (10) with the experimental data in Figs. 3.14(a) and 3.14(c) gives that $\nu = 0.65$ for $f_{strain} = 180Hz$ and $\nu = 0.42$ for $f_{strain} = 220$ Hz.

$$\Delta\varepsilon_{stable} = \frac{\frac{(T_{stable} - T_0) \cdot \lambda}{t_h}}{2 \cdot f_{strain} \cdot [0.2 - 0.04 \cdot \nu \cdot (T_{stable} - A_s)]}. \tag{3.10}$$

It seems in Eq. (3.10) that the stable strain amplitude $\Delta\varepsilon_{stable}$ is inversely proportional to t_h. But T_{stable} also depends on t_h. As a result, the t_h-dependence of strain amplitude is not inversely proportional, as shown by the comparison between Eq. (3.10) (with the obtained value $\nu = 0.65$ and 0.42) and the experimental data in terms of $\Delta\varepsilon_{stable}$ and t_h in Figs. 3.14(b) and 3.14(d) for f_{strain} = 180 Hz and 220 Hz respectively.

In summary, the t_h-dependence of the stable strain amplitude in the tests without strain drop (without phase transformation) can be explained by the heat balance between the ambient heat convection and the temperature-dependent energy dissipation of martensite reorientation. The evolution of the effective twinning stress with temperature can be estimated by Eq. (3.8), in which the fraction ν of Type I twin boundary depends on the loading frequency and can be determined by fitting of Eq. (3.10) with the

experimental data. For current system, lowering the loading frequency may lead to an increase in ν ($\nu = 0.65$ for $f_{strain} = 180$ Hz and $\nu = 0.42$ for $f_{strain} = 220$ Hz). In an extreme case of quasi-static mechanical test on the specimen, we find that almost all the nucleated twin boundaries are of Type I (i.e., fraction $\nu \approx 1$). The measured effective twinning-stress of quasi-static compression at two different temperatures are shown in Fig. 3.13 (see the two data points of squares within the shaded zone of the Type I twin boundary), indicating the significant temperature dependence. The thick blue line and the thin red line in Fig. 3.13 represent the temperature dependence of the effective twinning stress (governed by Eq. (3.8)) in the cases of $f_{strain} = 180$ Hz and 220 Hz respectively. Here it is assumed that the contribution fraction ν of Type I twin boundary relies only on the loading frequency, independent of the temperature or ambient heat-relaxation time t_h.

3.4.1.2 Region of weak ambient heat exchange (with phase transformation)

We can also use Eq. (3.10) derived in the previous subsection to describe the t_h-dependence of stable strain amplitude in the tests with weak ambient heat exchange ($t_h > t_h^*$ in Fig. 3.8) where the stable temperature is always around M_f. In these cases, with the constant stable temperature $T_{stable} = M_f$, Eq. (3.10) reduces to

$$\Delta\varepsilon_{stable} = \frac{(M_f - T_0) \cdot \lambda}{2 \cdot t_h \cdot f_{strain} \cdot \sigma_{tw}^{eff}}, \tag{3.11}$$

where

$$\sigma_{tw}^{eff} = 0.2 - 0.04 \cdot \nu \cdot (M_f - A_s). \tag{3.12}$$

With $M_f - A_s = -6°C$ and $\nu = 0.65$ (0.42) for f_{strain} =180 Hz (220 Hz) (determined in 3.4.1.1), we can determine the effective twinning stress by Eq. (3.12): $\sigma_{tw}^{eff} = 0.36$ MPa (0.30 MPa) at f_{strain} = 180 Hz (220 Hz).

Equation (3.11) shows that the stable strain amplitude is inversely proportional to t_h. The predicted inverse-proportion relation agrees well with the experimental observation in the tests at f_{strain} = 180 Hz and 220 Hz as shown in the Figs. 3.15(a) and 3.15(b), respectively. For a better demonstration on the physical meaning of the model, Eq. (3.11) is normalized as:

$$\Delta\bar{\varepsilon}_{stable} = \bar{t}_{MR}, \tag{3.13}$$

where

$$\Delta\bar{\varepsilon}_{stable} = \frac{\Delta\varepsilon_{stable}}{\Delta\varepsilon^{\text{complete MR}}},$$

$$\bar{t}_{MR} = \frac{t_{MR}}{t_h} = \frac{\left[\dfrac{(M_f - T_0)\cdot\lambda}{2\cdot f_{strain}\cdot\sigma_{tw}^{eff}\cdot\Delta\varepsilon^{\text{complete MR}}}\right]}{t_h}.$$

The parameter $\Delta\varepsilon^{\text{complete MR}}$ represents the theoretical maximum strain amplitude of the complete martensite reorientation in the whole specimen; it is around 6% based on the lattice parameters of 10M Ni-Mn-Ga specimen. The normalized stable strain amplitude $\Delta\bar{\varepsilon}_{stable}$ $(= \frac{\Delta\varepsilon_{stable}}{\Delta\varepsilon^{\text{complete MR}}})$ indicates the fraction of the materials taking martensite reorientation in the specimen. t_{MR} $(= \frac{(M_f - T_0)\cdot\lambda}{2\cdot f_{strain}\cdot\sigma_{tw}^{eff}\cdot\Delta\varepsilon^{\text{complete MR}}})$ is the time needed for the energy dissipation of the cyclic complete martensite reorientation to increase the material temperature from T_0 to M_f without the ambient heat exchange. The normalized time $\bar{t}_{MR}$ $(= \frac{t_{MR}}{t_h})$ is the ratio between the two time scales: t_{MR} and the characteristic heat-relaxation time t_h. The time ratio $\bar{t}_{MR}$ represents the competition between the heat generation from the martensite reorientation and the heat transfer to

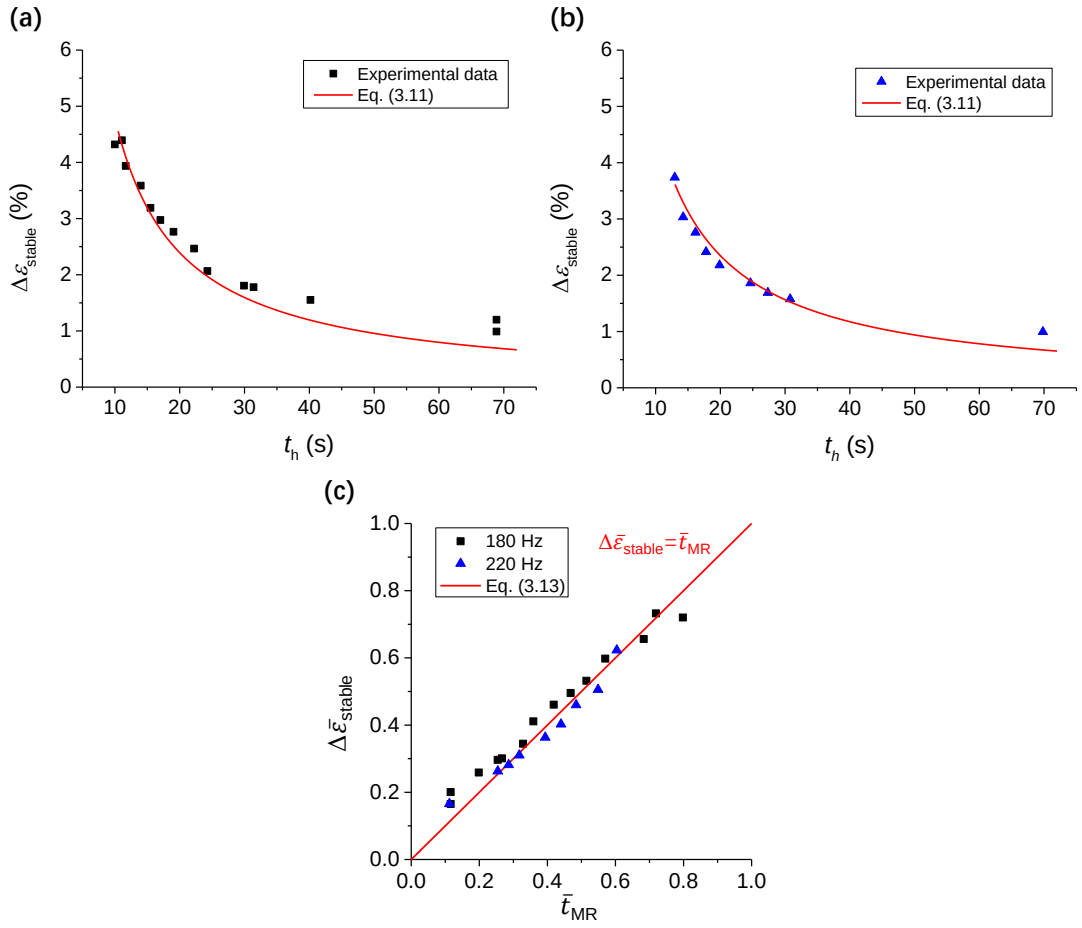

Figure 3.15 The comparison between the theoretical model (Eq. (3.11)) and the experimental data for the tests at f_{strain} = 180 Hz (a) and 220 Hz (b). (c) The comparison between the normalized model (Eq. (3.13)) and the normalized experimental data of f_{strain} = 180 and 220 Hz in terms of $\Delta\bar{\varepsilon}_{stable}$ and $\bar{t}_{MR}$.

the ambient, governing the heat balance in the steady states. It is interesting to see in Eq. (3.13) that the time ratio $\bar{t}_{MR}$ equals to the material fraction taking martensite reorientation in the specimen, i.e., it governs the fraction of the materials transformed into A-phase in the steady state. The normalized model (Eq. (3.13)) agrees well with experiments of both loading frequencies in Fig. 3.15(c).

In summary, the t_h-dependence of the stable strain amplitude in the tests with strain

drop due to phase transformation is governed by a self-organization process of the specimen: the specimen maintains the stable temperature around M_f by adjusting the output strain amplitude (i.e., the fraction of the materials taking martensite reorientation) to keep the balance between the heat generation from martensite reorientation and the heat transfer to the ambient. For the specimen used in the experiments, its characteristic phase transformation temperatures M_f, M_s, A_s and A_f (35.5 °C, 36.5 °C, 41.5 °C and 42.2 °C respectively) are close to each other. Especially, the difference between M_s and M_f is only 1 °C. So the percentage of Martensite can change from 0% to 100% in this narrow temperature range. That is why the working temperature is almost constant while the output strain (reflecting the percentage of the martensite in the specimen) can change significantly with t_h in the tests of the weak ambient airflows ($t_h > t_h^*$) in Fig. 3.8.

3.4.2 Optimal conditions to achieve large stable strain amplitude

The controlled loading conditions in the tests on the FSMA specimen include (1) the magnetic condition (magnetic field frequency f_{mag}), (2) mechanical condition (initial compressive stress σ_{ini}) and (3) thermal condition (the ambient heat convection characterized by the relaxation time t_h). With the systematic data in Table 3.1 of the tests in the still air, the output strain amplitude of the short- and the long-time actuation at different levels of $f_{strain}(= 2f_{mag})$ and σ_{ini} are plotted as contour maps in Figs. 3.16(a) and 3.16(b), respectively. In Fig. 3.16(a), a large $\Delta\varepsilon$ (e.g., $\Delta\varepsilon > 4.5\%$) can be obtained in a proper frequency range, for example, $f_{strain} = 2f_{mag}$ = 140 Hz ~ 220 Hz covering the resonant frequency of the current dynamic system. The resonant frequency depends on the total mass of the specimen and the moving parts of the dynamic system. It also

depends on the stiffness of the spring and the specimen. Detailed studies on the mass and the stiffness effects can be found in the literature (Henry et al., 2002; Lai, 2009; Techapiesancharoenkij et al., 2011, 2009).

A proper level of the initial stress σ_{ini} is also important to achieve a large $\Delta\varepsilon$. When σ_{ini} is too high (such as 4 MPa), the stress-preferred variant (M1) is always stable and the cyclic martensite reorientation can't occur. In this case $\Delta\varepsilon$ is close to 0 (see $\Delta\varepsilon$ at σ_{ini} = 4 MPa in Table 3.1). By contrast, if σ_{ini} is too low, the magnetic-field-preferred variant (M2) is stable and cannot fully transform to M1. In this case, $\Delta\varepsilon$ is also small. An interesting phenomenon was found in the experiments at a low level of σ_{ini}, e.g., σ_{ini} = 0.1 MPa in Fig. 3.17. It's seen that, for a given loading condition, the system does not reach one steady state, but switches between two "quasi-steady" states. For example, in Fig. 3.17(a), $\Delta\varepsilon$ switches between 0.4% and 1.3% and the temperature varies correspondingly between 34.1 °C and 37.8 °C. There seems to be two "stable" states switching to each other cyclically. Although some studies on the meta-stability of dynamic behaviors of the traditional SMAs appeared recently in the literature (see (Xia and Sun, 2017, 2015) and the references therein), such phenomenon in FSMAs is observed for the first time and its origin is still unclear and needs further studies.

After choosing proper magnetic field frequency f_{mag} and initial stress σ_{ini}, we need to control the ambient flow (i.e., the heat-relaxation time t_h) to avoid the strain drop (avoid phase transformation) in the long-time actuation. As discussed in Section 3.4.1, there exists an optimal ambient airflow (optimal t_h^*) at which the stable strain amplitude is maximum and the stable temperature is close to M_f (see Fig. 3.8). From the normalized model of Eq. (3.13), we can estimate the optimal heat-relaxation time t_h^* by allowing 100% materials to take the complete martensite reorientation in the whole

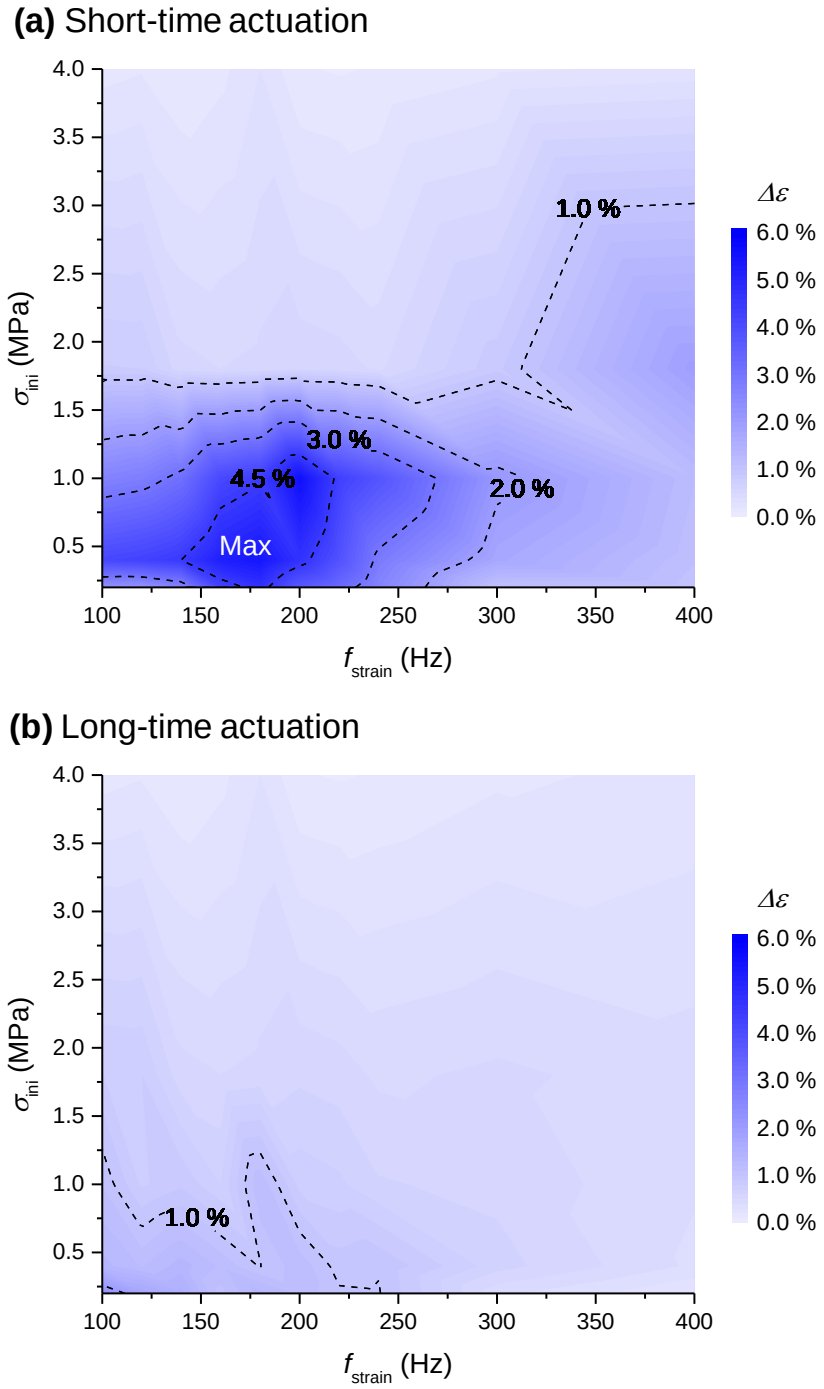

Figure 3.16 Contours of the output strain amplitude $\Delta\varepsilon$ at various frequencies and initial compressive stresses during the short-time actuation (a) and the long-time actuation (b). The data are from Table 3.1 and all the tests are conducted in the still air.

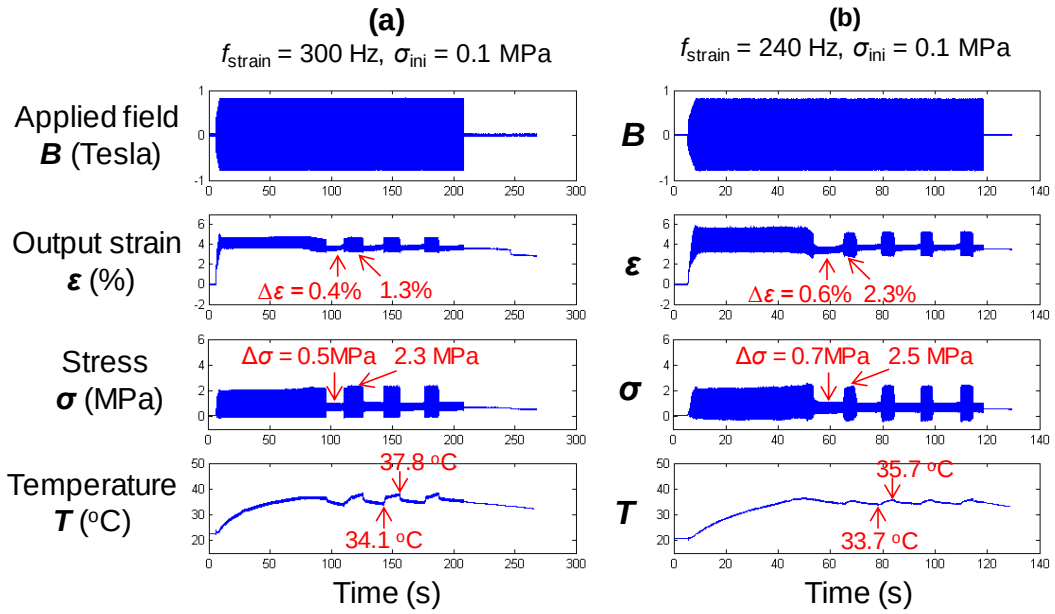

Figure 3.17 Oscillation phenomenon observed in the tests at the low initial compressive stress σ_{ini} = 0.1 MPa: the strain amplitude $\Delta\varepsilon$ and the stress amplitude $\Delta\sigma$ periodically switch between two "stabl" states.

specimen (i.e., $\Delta\bar{\varepsilon}_{stable} = 1$):

$$1 = \Delta\bar{\varepsilon}_{stable} = \bar{t}_{MR} = \frac{t_{MR}}{t_h^*} = \frac{\left[\dfrac{(M_f - T_0)\cdot\lambda}{\Delta\varepsilon^{\text{complete MR}}\cdot 2\cdot f_{strain}\cdot\sigma_{tw}^{eff}}\right]}{t_h^*},$$

$$\Longrightarrow t_h^* = t_{MR} = \frac{(M_f - T_0)\cdot\lambda}{\Delta\varepsilon^{\text{complete MR}}\cdot 2\cdot f_{strain}\cdot\sigma_{tw}^{eff}}. \tag{3.14}$$

Equation (3.14) shows that the stable strain amplitude is maximized when the characteristic heat relaxation time t_h equals the characteristic time scale of martensite reorientation t_{MR}. For the given condition: T_0 = 20 °C, M_f = 35.5 °C, $\lambda = 4\times10^6$ J · m^{-3} · K^{-1}, $\Delta\varepsilon^{\text{completeMR}}$ = 6%, f_{strain} = 180 Hz (220 Hz), and σ_{tw}^{eff} = 0.36 MPa (0.30 MPa) determined by Eq. (3.12) in Section 3.4.1.2, Eq. (3.14) predicts the optimal

heat-relaxation time t_h^{*model} = 8.0 s for 180 Hz (7.8 s for 220 Hz). It's seen that, at f_{strain} = 180 Hz, the predicted t_h^{*model} = 8.0 s agrees well with the experimental observation of t_h^* = 8.8 s in Fig. 3.8(a). But for the case of f_{strain} = 220 Hz, the predicted t_h^{*model} = 7.8 s is not close to the experimental measurement of t_h^* = 11.7 s in Fig. 3.8(b). The reason for this discrepancy is that Eq. (3.14) is derived with the assumption of complete martensite reorientation ($\Delta\varepsilon^{\text{complete MR}}$ = 6%) in the whole specimen. For the case of f_{strain} = 180 Hz which is close to the resonant frequency (see the peak output strain $\Delta\varepsilon_{unstable}$ in Fig. 3.5), the maximum strain amplitude before the strain drop $\Delta\varepsilon_{unstable}$ = 5.9% in Fig. 3.5 is close to that of the complete martensite reorientation $\Delta\varepsilon^{\text{complete MR}}$ = 6%. By contrast, f_{strain} = 220 Hz is far from the resonant frequency (see Fig. 3.5), and its maximum strain amplitude before the strain drop is $\Delta\varepsilon_{unstable}$ = 3.9%, which is obviously lower than $\Delta\varepsilon^{\text{complete MR}}$ = 6%. Therefore, we should use the strain amplitude before the strain drop $\Delta\varepsilon_{unstable}$ to replace $\Delta\varepsilon^{\text{complete MR}}$ in Eq. (3.14) to estimate t_h^* for the cases far from the resonant frequency of the system.

$$t_h^* = \frac{(M_f - T_0)\cdot\lambda}{\Delta\varepsilon_{unstable}\cdot 2\cdot f_{strain}\cdot\sigma_{tw}^{eff}}. \tag{3.15}$$

Substituting $\Delta\varepsilon_{unstable}$ = 5.9% and 3.9% for the cases of f_{strain} = 180 Hz and 220 Hz respectively into Eq. (3.15), the predicted $t_h^{*\text{model}}$ are 8.1 s and 12.0 s, which agree well with the experimentally observed t_h^* = 8.8 s and 11.7 s in Figs. 8(a) and 8(b), respectively. This implies that, Eq. (3.14) can be used to find the optimal heat-relaxation time t_h^* for the complete martensite reorientation in the whole specimen with the loading frequency close to the resonant frequency of the system, while Eq. (3.15) can predict t_h^* for general cases with the reference to the strain amplitude $\Delta\varepsilon_{unstable}$ of the short-time actuation (before the strain drop).

3.5 Summary and conclusions

In this chapter, systematic experiments are performed on the long-time (> 100 s) dynamic behaviors of FSMA under the cyclic magnetic field. The experiments were conducted at various levels of the magnetic field frequency, the initial compressive stress and the ambient airflow velocity. Critical conditions to achieve large stable strain amplitudes in dynamic actuation were derived. A simple 1D heat transfer model is also developed. The analyses from the model well explain the ambient effects on the long-time responses (i.e., the stable strain and the stable temperature) of FSMA observed in the experiments. Furthermore, while the temperature rise caused by the dissipation of the frictional twin boundary motions was generally taken as a negative effect in FSMA actuator applications and should be avoided, we proposed to utilize the temperature rise and the associated heat balance to actively control the stable temperature and the output strain amplitude of FSMA by setting properly the ambient heat exchange condition (i.e., airflow velocity). The important conclusions of the chapter are given below:

(1) Energy dissipation due to the high-frequency cyclic martensite reorientation can cause significant temperature rise. When the temperature increases to the characteristic phase transformation temperature, the Martensite-to-Austenite phase transformation will occur in the FSMA specimen, which makes the strain amplitude suddenly decrease to a much lower level. Therefore, the large strain amplitude of FSMA without a steady-state temperature lower than the phase-transformation temperature is at risk of instability (strain drop) during the long-time actuation.

(2) The stable strain amplitude and the stable temperature of FSMA can be controlled by the ambient heat exchange efficiency (corresponding to airflow velocity). The

stable strain amplitude depends on the airflow velocity non-monotonically. With the decrease of the airflow velocity (the corresponding heat exchange efficiency decreases), the strain amplitude first increases due to the temperature-dependence of the effective twinning stress and then decreases due to the temperature-induced phase transformation which disturbs the magnetic-field-induced martensite reorientation. The maximum stable strain amplitude is obtained at the critical heat-relaxation time t_h^* which makes the stable temperature close to (but lower than) the phase-transformation temperature.

(3) A special "isothermal" FSMA actuator with tunable output strain is proposed by taking advantage of the interaction between the temperature-induced phase transformation and the magnetic-field-induced martensite reorientation. The strain amplitude of this actuator changes monotonically with the ambient airflow velocity due to the balance between the heat generated from the martensite reorientation of the untransformed martensite region (related to the strain amplitude) and the heat transferred to the ambient (related to the airflow velocity), while its working temperature is almost constant (close to the phase-transformation temperature) and independent of the strain amplitude. That means, the self-adjustment of the forward and reverse martensitic phase transformations can significantly change the volume fraction of martensite in the specimen (i.e., a significant change of the strain amplitude) within a narrow phase-transformation temperature range.

Chapter 4

Coexistence and compatibility of martensite reorientation and phase transformation

High-frequency magnetic-field-induced martensite reorientation (MR) is one of the most important advantages of ferromagnetic shape memory alloys (FSMAs), but its stability is threatened by dissipation heat accumulation ("self-heating") of cyclic frictional twin-boundary motion, which can cause temperature-induced phase transformation (PT) and reduce the output-strain amplitude significantly. In this chapter, the interaction of the temperature-induced PT and the magnetic-field-induced MR during high-frequency magnetic actuation on FSMA is studied with in-situ observations of local-strain evolution in conjunction with microstructure-compatibility analysis. Based on the nominal strain and temperature responses and the corresponding local-strain maps, it is revealed that, when the temperature-induced PT takes place during the high-frequency field-

induced MR, the specimen is divided into three zones: non-active austenite zone (with a constant deformation), active martensite zone (with cyclic deformations of MR) and buffering needle-zone (interfacial zone) with a fine-needle-twin structure which plays an important role in maintaining the compatibility between austenite and martensite zones with different cyclic deformations during the dynamic loading. A novel mechanism is revealed that, under the magnetic actuation with changing ambient airflow, the "self-heating" temperature-driven phase boundary motion and the magnetic-field-driven twin boundary motion can coexist, because the specimen needs to self-organize the different phases/variants to satisfy all the thermo-magneto-mechanical boundary conditions. Taking advantage of this mechanism, the volume fractions of austenite and martensite zones can be adjusted with changing ambient-airflow velocity, which provides an effective way to tune the nominal output-strain amplitude (from 1% to 6% in the current study) while the working temperature is kept almost constant (around M_s and M_f).

4.1 Introduction

Ni-Mn-Ga single crystal is a typical Ferromagnetic Shape Memory Alloy (FSMA) which has potential applications such as magneto-caloric refrigerators (Basso, 2011; Li et al., 2014; Singh et al., 2014; Sokolovskiy et al., 2014) and high-frequency large-stroke actuators (Henry, 2002; Lai et al., 2008; Smith et al., 2014; Techapiesancharoenkij et al., 2009; Yin et al., 2016) based on the field-induced martensitic phase transformation (transformation between martensite phase and austenite phase) and the field-induced martensite reorientations (transition among the variants of the martensite phase), respec-

tively. It was reported in the literature that the levels (magnitudes) of the magnetic fields required to drive the Phase Transformation (PT) and the Martensite Reorientation (MR) are significantly different: several Teslas for the phase transformation while less than 1 Tesla for the martensite reorientation (Bruno et al., 2017; Gabdullin and Khan, 2015; Haldar et al., 2014; Karaca et al., 2006, 2009, 2007). So most of the existing research work studied phase transformation and martensite reorientation separately (Arndt et al., 2006; Auricchio et al., 2014; Haldar et al., 2014; Karaca et al., 2006, 2007; Lai et al., 2008; Pinneker et al., 2014; Rogovoy and Stolbova, 2016; Sehitoglu et al., 2012; Zou et al., 2018) , without considering their interactions.

While the magnetic-field-driven phase transformation needs a very strong magnetic field (which is not easy to obtain), temperature-induced phase transformation can be easily triggered in FSMA by external heat sources (Pinneker et al., 2014) or the self-heating due to the intrinsic dissipation of the cyclic martensite reorientation (Henry, 2002; Jugo et al., 2018; Lai, 2009; Pascan et al., 2015; Zhang et al., 2018b). Particularly, in a high-frequency FSMA actuator, the dissipation heat of the cyclic frictional twin boundary motion during the martensite reorientation can be accumulated quickly to increase the specimen temperature (Henry, 2002; Jugo et al., 2018; Lai, 2009; Pascan et al., 2015; Zhang et al., 2018b) to a level comparable with the material characteristic phase-transformation temperatures where the Martensite-to-Austenite (M-to-A) phase transformation can take place (Jugo et al., 2018; Pascan, 2015; Zhang et al., 2018b). The phase transformation disturbs the process of the field-induced martensite reorientation, leading to a significant drop in the output strain amplitude of the FSMA actuators (Jugo et al., 2018; Pascan, 2015; Zhang et al., 2018b). This instability problem is obviously harmful in developing high-frequency large-stroke FSMA actuators.

Recently, a method of changing the ambient airflow (governing the heat exchange efficiency) to control the specimen working temperature was proposed in Chapter 3 (Zhang et al., 2018b) to overcome this difficulty and to achieve a large output stain in the high-frequency actuation as shown in Fig. 2.1, where the combination of the orthogonal mechanical force and the cyclic magnetic field leads to the cyclic switching between the two different martensite variants (so-called "stress-preferred variant" and "field-preferred variant" M_2). It was shown that the output strain amplitude depended on the controlled ambient airflow velocity. Particularly, when the temperature-induced phase transformation and the field-induced martensite reorientation coexist, the working temperature of the specimen consisting of different phases and variants was kept almost constant (close to the material characteristic phase transformation temperatures) while the output strain amplitude changed significantly from 6% (complete martensite reorientation) to less than 1% (only little martensite reorientation), depending on the airflow velocity. One possible explanation for this phenomenon is that the specimen could self-organize its volume fractions of the martensite phase (M-phase) and the austenite phase (A-phase) to satisfy the thermal balance between the martensite reorientation dissipation heat and the heat transfer to the ambient (controlled by the airflow velocity) (Zhang et al., 2018b). To verify this conjecture, a high-frequency magnetic actuation on Ni_2MnGa single crystal is performed under an ambient airflow with stepped changing velocities (to change the heat-exchange efficiency), and in-situ Digital Image Correlation (DIC) observation on local strain distributions and evolutions is conducted in this chapter (Zhang et al., 2018a). It is found that the temperature-induced M-to-A phase transformation makes the specimen form non-active austenite zone (A-phase with a constant strain) and active martensite zone (M-phase with 6% strain oscillation due to cyclic martensite reorientation) during the magnetic actuation, and the volume

fractions of the non-active and active zones change significantly under the different ambient airflow velocities. This reveals a novel mechanism that both the temperature-driven phase-boundary motion and the magnetic-field-driven twin-boundary motion can be activated simultaneously during the high-frequency magnetic actuation on FSMA, which enables the specimen self-organize the different phases/variants to satisfy all the thermo-magneto-mechanical boundary conditions and provides an effective option to tune the high-frequency output strain amplitude of FSMAs (from 1% to 6% in the current study).

Moreover, the in-situ observations on the local strain evolution demonstrate how the active zone (with the strain oscillation of the cyclic martensite reorientation) is compatible with the non-active zone (with a constant strain of the A-phase). The compatibility between different phases (and different variants) in shape memory alloys has been widely studied (Bhattacharya, 2003; Seiner et al., 2011; Stupkiewicz et al., 2007); the compatibility analyses are based on the principle of the energy minimization studying the static configurations: only some discrete phase/variants fractions satisfy the compatibility. In other words, the phase/variants fractions can't continuously change in the compatible configurations. (Note: some special materials satisfying so-called "co-factor condition" might allow a continuous change in the compatible phase fractions (Chen et al., 2013b; Song et al., 2013)). To my best knowledge, the currently-observed compatibility between the active martensite zone of strain oscillation (with the cyclic and continuous change in the volume fractions of the two martensite variants (M_1 and M_2)) and the non-active austenite zone of a static strain has never been explained in the literature. In this chapter, based on the observations of the distributions of the phases/variants and the microstructure compatibility analysis, it is revealed that, for the compatibility between the active martensite zone and non-active austenite zone, the

interface between the two zones is not a sharp habit plane, but a buffering zone with needle-like fine twins where the third martensite variant M_3 (which doesn't participate in the cyclic martensite reorientation) might be generated during the self-organizing process of the simultaneous field-induced martensite reorientation and the temperature-induced phase transformation.

The remaining of this chapter is organized as follows: Section 2 introduces the material properties and the experimental setup. Section 3 reports the experimental results of the macroscopic responses (the output strain and the specimen temperature evolution) and the local strain evolution (the DIC strain maps) under various ambient conditions (i.e., airflows of different velocities). The compatibility analysis and its comparison with the experimentally observed strain patterns are performed in Section 4. Finally, the summary and conclusions are provided in Section 5.

4.2 Material properties and experimental setup

The experiment in is chapter are conducted with the same experiment system of magnetic actuation and on the same rectangular bar of $Ni_{50}Mn_{28}Ga_{22}$ (at. %) single crystal as used in Chapter 3 (with dimensions in 2×3×15 mm, as shown in Fig. 2.1). The material is in the state of 10M martensite phase at room temperature and the martensite variants are slightly monoclinic ($\gamma = 90.37°$). For the simplicity of the analysis here, we assume that the martensite variants are tetragonal with two long axes "a" and one short axis "c" (as adopted in various researches (Haldar et al., 2014; Karaca et al., 2006, 2007; Pinneker et al., 2014, 2013; Zhang et al., 2018b)).

Before the test, the specimen is fully compressed along y-direction to obtain the single variant state with the short-axis (c-axis) along y-direction (so-called stress-preferred variant, shown as M_1 in Fig. 2.1(b)), which is the reference state for the calculation of the specimen deformation strain in this chapter. At the beginning of the test, an initial compressive stress $\sigma_{ini} = 0.4$ MPa is applied on the specimen along y-direction by a compressed spring (of stiffness 5.5 kN/m). Then a magnetic field (with magnetic flux density B cyclically varying between ±0.78 Tesla as shown in Fig. 2.1(b)) of frequency $f_{mag} = 90$ Hz is applied horizontally along x-direction to drive the martensite reorientation from M_1 to M_2 (so-called field-preferred variant with the short axis c along x-direction) as shown in Fig. 2.1(b). The martensite reorientation makes the specimen length L_y change, which leads to a change in the compressive stress applied by the spring. The competition between the cyclic magnetic field and the evolving compressive stress eventually drives the cyclic martensite reorientation between the variants M_1 and M_2, which produces cyclic strain along y-direction. Theoretically, the strain along y-direction is around 6% for the martensite reorientation from M_1 to M_2 ($(a-c)/c \approx 6\%$), and around 4% for the phase transformation from M_1 to the cubic austenite ($(a_0-c)/c \approx 4\%$). Similar to that in Chapter 3, the temperature dependence of lattice parameters (Glavatska et al., 2002; Pagounis et al., 2014; Straka et al., 2006) are ignored in the current experiments with the small temperature variation (i.e., from the room temperature ($\approx 18°$C) to the martensite start temperature Ms = 36.5°C). During the test, the ambient heat-exchange condition is controlled by forcing ambient airflow (around the room temperature) of velocity V_{air} changing from 0 m/s to 16 m/s to pass through the specimen (see Fig. 4.1(a)). The specimen temperature is monitored by a thermocouple (K-type, 0.5 mm sheath diameter) at the bottom end of the specimen. During the whole dynamic actuation, a CMOS camera of 2048×1088 pixels (Basler

acA2000-340 km) with Nikkor lens is used to record the optical images of the specimen surface (in a gage section of around 4 mm), which are processed by Digital Image Correlation (DIC) software Vic-2D (Correlated Solutions) to obtain the in-situ local strain distributions and evolutions under different airflow velocities.

4.3 Local strain evolution under high-frequency magnetic loading

Figure 4.1(a) shows the loading conditions (the cyclic magnetic field between ±0.78 Tesla and the changing airflow velocity (V_{air} = 0 m/s ~ 16 m/s)) and the responses of the nominal output strain and the specimen temperature, while Fig. 4.1(b) shows the zoomed nominal strain curves and the local strain distributions (DIC strain maps) of the corresponding responses at several typical time slots ($t_1 \sim t_7$). It is seen that at each increase in the airflow velocity, the amplitude $\Delta\varepsilon$ of the strain oscillation increases correspondingly (see the strain amplitude change at the time $t \approx$ 100 s, 155 s, 220 s, 275 s, and 330 s in Fig. 4.1(a) and the zoomed nominal strain curves at different time slots in Fig. 4.1(b)). However, a strain amplitude drop from 5.8% to 1.0% is observed at $t \approx$ 15 s even though the ambient airflow didn't change (keeping still air, V_{air} = 0 m/s).

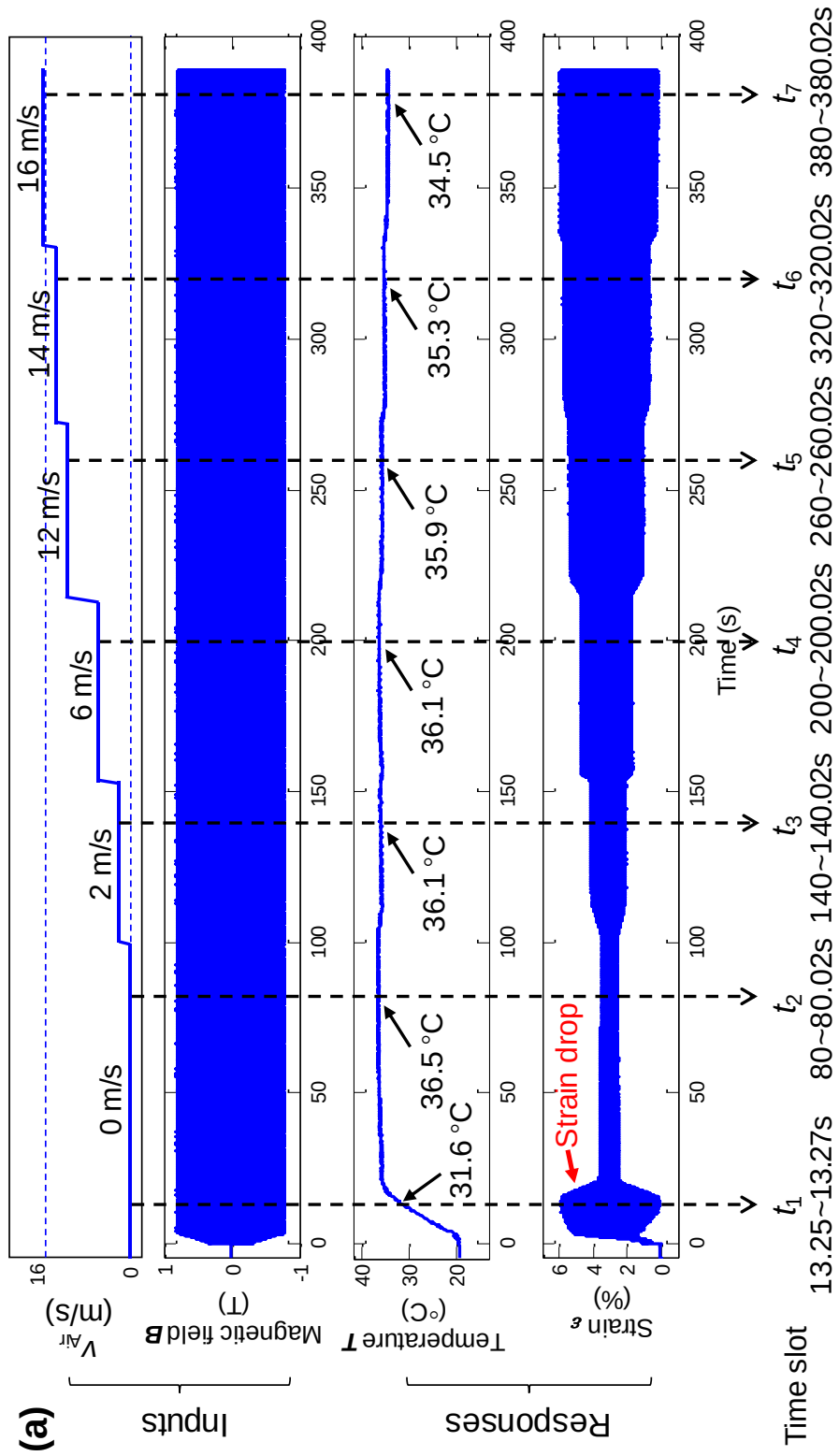

Figure 4.1 (a) The global responses of FSMA-actuator under the same magnetic loading (the cyclic magnetic field between ±0.78 Tesla) but the changing airflow velocity (V_{air} = 0 m/s ~ 16 m/s). (b) The zoomed nominal strain curves, the DIC local strain maps and the corresponding local strain profiles (the red and black lines represent the local strains at the maximum and minimum nominal strain states respectively) along the centerline at the typical time slots marked in (a).

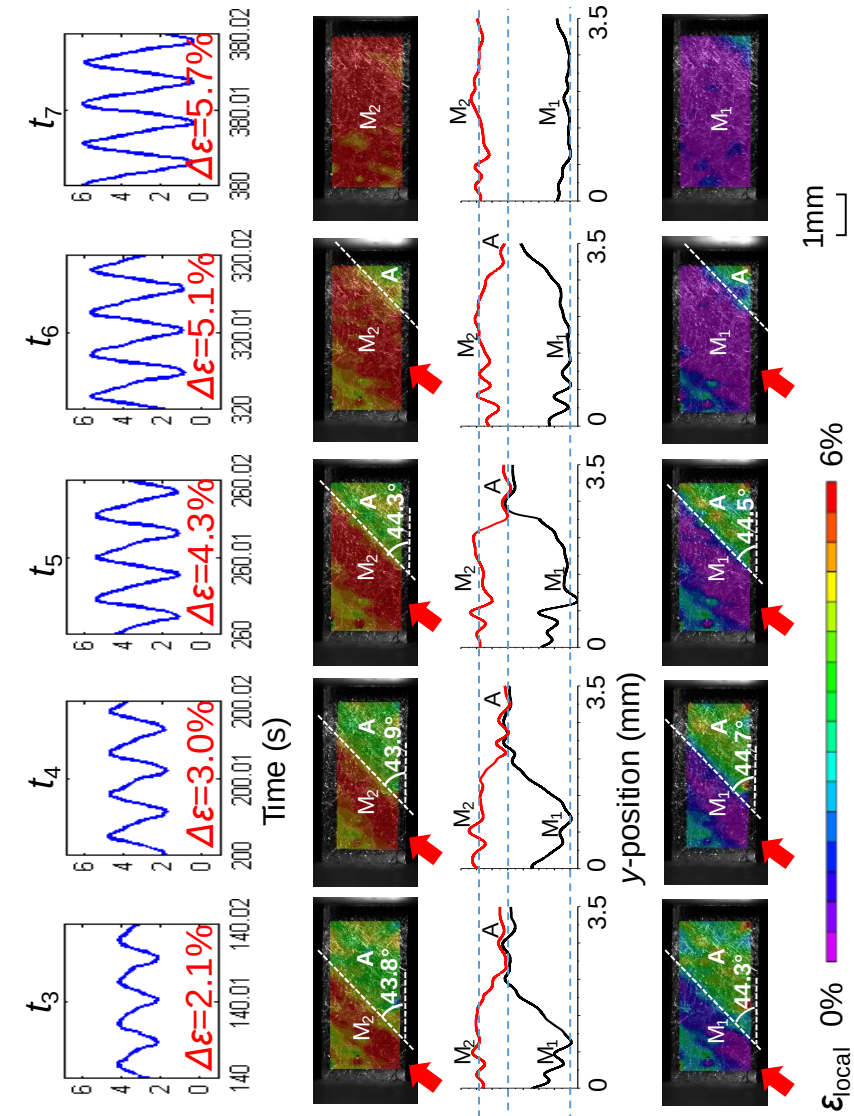

Figure 4.1 Continue.

With the start of the dynamic test in still air (V_{air} = 0 m/s at t = 0 in Fig. 4.1(a)), the output strain amplitude increased rapidly to be close to the strain (6%) of a complete martensite reorientation while the specimen temperature T increased slowly from the room temperature, for example, T increased to 31.6 °C at t = 13.25 s in Fig. 4.1(a). The corresponding DIC strain maps at the time slot t_1 (13.25 s ~ 13.27 s) in Fig. 4.1(b) show that the optically observed gauge section of the specimen had the local strains of around 0% (with the violet color) and around 6% (with the red color) when the nominal output strain (the global strain of the whole specimen) reached the minimum and maximum levels, respectively. That means a complete martensite reorientation cycle can be achieved at that time. The local strain evolution of a typical cycle at the time slot t_1 is shown in Fig. 4.2 where the twin boundary (interface between the two martensite variants) of an angle of 44.7° at the x-y plane (the observed specimen surface) can be identified. It should be noted that, during the magnetic loading, many fine twins can be generated and the motion of numerous twin boundaries can be activated (Chmielus et al., 2008; Lai et al., 2008). In the current test, the detailed microstructures of such fine twins cannot be resolved due to the limited resolution of the optical camera. So the fine-twin regions are just denoted by M_1+M_2 domains whose strain can continuously change between 0% and 6% as shown in the local strain profiles along the center line of the gauge section in Fig. 4.2.

The observation above clearly demonstrates that a complete martensite reorientation cycle with 6% strain amplitude can be achieved under the current magnetic actuation. But the specimen temperature T kept increasing at t_1 as shown in Fig. 4.1(a), which indicates that the system had not yet reached a steady state. When the specimen temperature became higher than 36 °C (close to the material characteristic phase transformation temperatures), the output strain amplitude $\Delta\varepsilon$ dropped to around 1% at

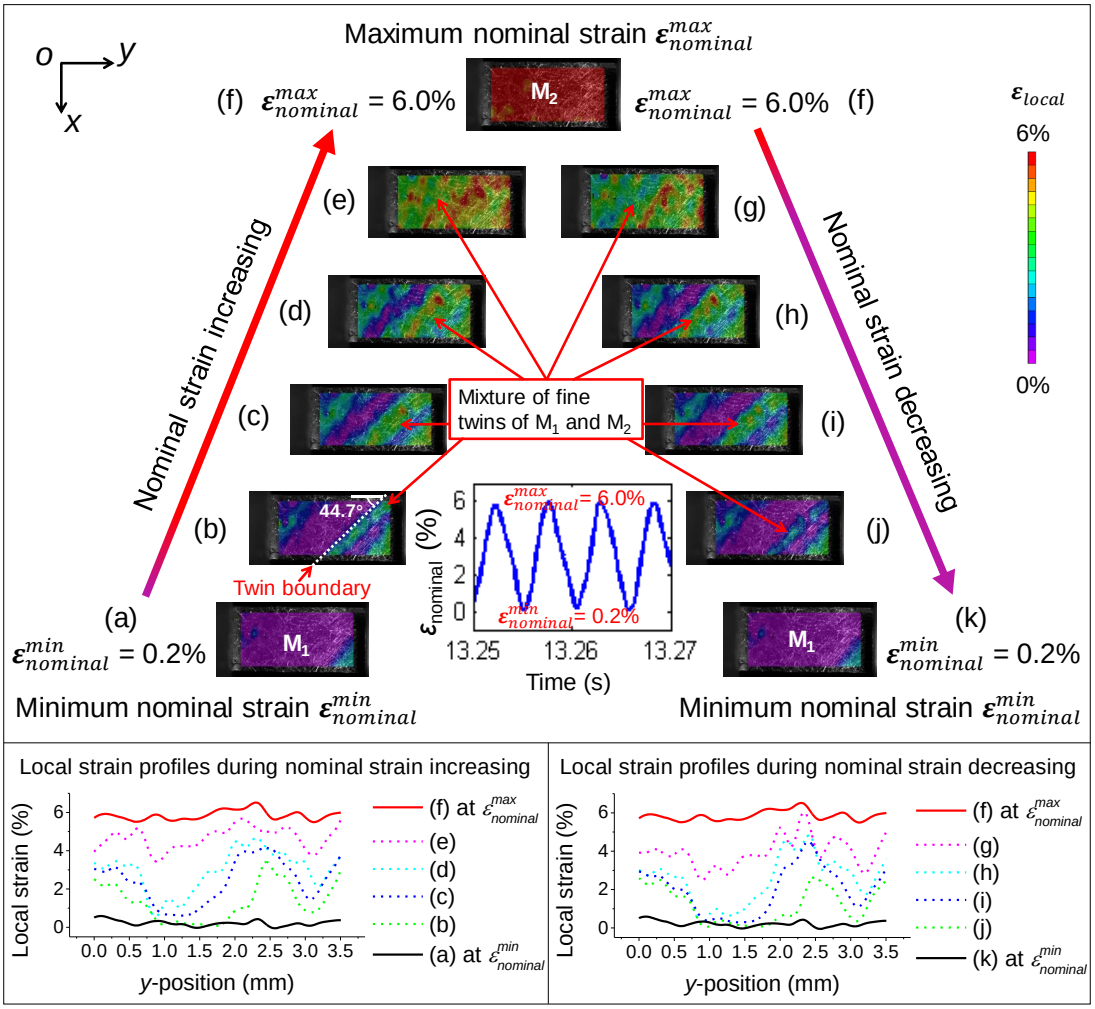

Figure 4.2 DIC local strain evolutions in a typical cycle of the martensite reorientation process before the occurrence of the strain drop phenomenon (pure martensite phase) at the time slot t_1.

$t \approx 20$ s in Fig. 4.1(a). After the strain drop, the system reached a steady state—both the strain amplitude and temperature were kept almost constant ($\Delta\varepsilon$ = 1.0% and T = 36.5°C). The typical local strain fields at this stage (time slot t_2 of 80 s ~ 80.02 s in Fig. 4.1(b)) show almost the same strain level of around 4% (represented by the green color) in the observed region of the specimen for both the minimum and maximum nominal strain of the cycle. This indicates that the observed gauge section of the

specimen contributes little to the output strain during the cyclic magnetic loading. The green region is occupied by the austenite phase (A-phase) for the following facts: (a) the theoretical strain of the cubic A-phase with respect to the martensite variant M_1 is around 4% for the material, (b) the green region is not sensitive to such low level of magnetic field (< 1 Tesla), and (c) the green region appears when the specimen temperature was increased to the material characteristic phase transformation temperatures. Thus, the field-induced deformation of martensite reorientation was significantly suppressed due to the "self-heating" temperature-induced phase transformation.

When the ambient airflow velocity was increased to 2 m/s, the temperature decreased slightly from 36.5 °C to 36.1 °C; but the nominal output strain amplitude increased significantly from 1.0% to 2.1%, as shown in Fig. 4.1(a) and the zoomed nominal strain curve at t_3 (140 s ~ 140.02 s) in Fig. 4.1(b). The corresponding DIC strain maps at t_3 in Fig. 4.1(b) demonstrate that, in the observed gauge section, the martensite zone (M-zone) of cyclic martensite reorientation (where the local strain oscillated between 0% and 6%, as marked by red arrows) appeared again and the volume of the A-phase (A-zone, as shown in green) was reduced. The interface between the A-zone and the M-zone (A-M phase boundary) with an angle near 45° can be identified (see dashed lines in Fig. 4.1(b)). Further increasing the airflow velocity made the nominal output strain amplitude increase and the volume of the A-phase decrease (through the phase boundary propagation) as shown by the nominal output strain evolution ($\Delta\varepsilon$ = 2.1%, 3.0%, 4.3% and 5.1%) and the DIC strain maps at $t_3 \sim t_6$ in the Fig. 4.1(b). It is seen from the local strain filed evolutions from t_3 to t_6 that the phase boundary between A- and M-zones propagated with the increasing airflow velocity and kept the same angle (near 45°), which means that changing the ambient heat-exchange efficiency (by changing airflow velocity) can drive the A-M phase boundary motion to adjust the volume fractions

of A- and M-zones. Figure 4.3 shows a typical cycle of the local strain evolution for the time slot t_6. By comparing the DIC strain maps at the minimum nominal strain ($\varepsilon^{min}_{nominal} = 0.6\%$) and the maximum nominal strain ($\varepsilon^{max}_{nominal} = 5.7\%$), we can identify the active zone (i.e., M-zone with cyclic strain due to martensite reorientation between M_1 and M_2) and the non-active zone (i.e., A-phase with constant local strain). It is interesting to note that the A-M phase boundary (represented by dashed lines) between the active M-zone and the non-active A-zone is nearly parallel to the twin boundary (represented by dotted lines) at the observed surface (x-y plane), and both of them have an angle of around 45°. It is further noted that the A-M phase boundary is fixed while the twin boundaries cyclically move in the active M-zone in the magnetic loading cycle.

At the time slot t_6, the output strain $\Delta\varepsilon$ was 5.1% and there still existed A-phase (non-active zone) in the specimen. In order to improve the output strain, the airflow was further increased to 16 m/s where $\Delta\varepsilon$ increased to 5.7% as shown by the strain response and the DIC strain maps in the time slot t_7 (380 s ~ 380.02 s) in Fig. 4.1(b). It is seen that, in the observed gauge section, the non-active zone (A-phase) disappeared; the whole gauge section took a cyclic complete martensite reorientation between martensite M_1 and M_2.

In summary, the temperature-induced Martensite-to-Austenite (M-to-A) phase transformation occurred to disturb the field-induced deformation of the martensite reorientation, leading to a significant strain drop, when the specimen temperature increased to the material characteristic phase transformation temperature due to the frictional twin boundary motion. The evolution of the DIC local strain maps reveals that the volume fraction of the A-phase (non-active zone contributing little to the cyclic output strain) in the specimen significantly changed with the ambient airflow velocity. That's to say, the

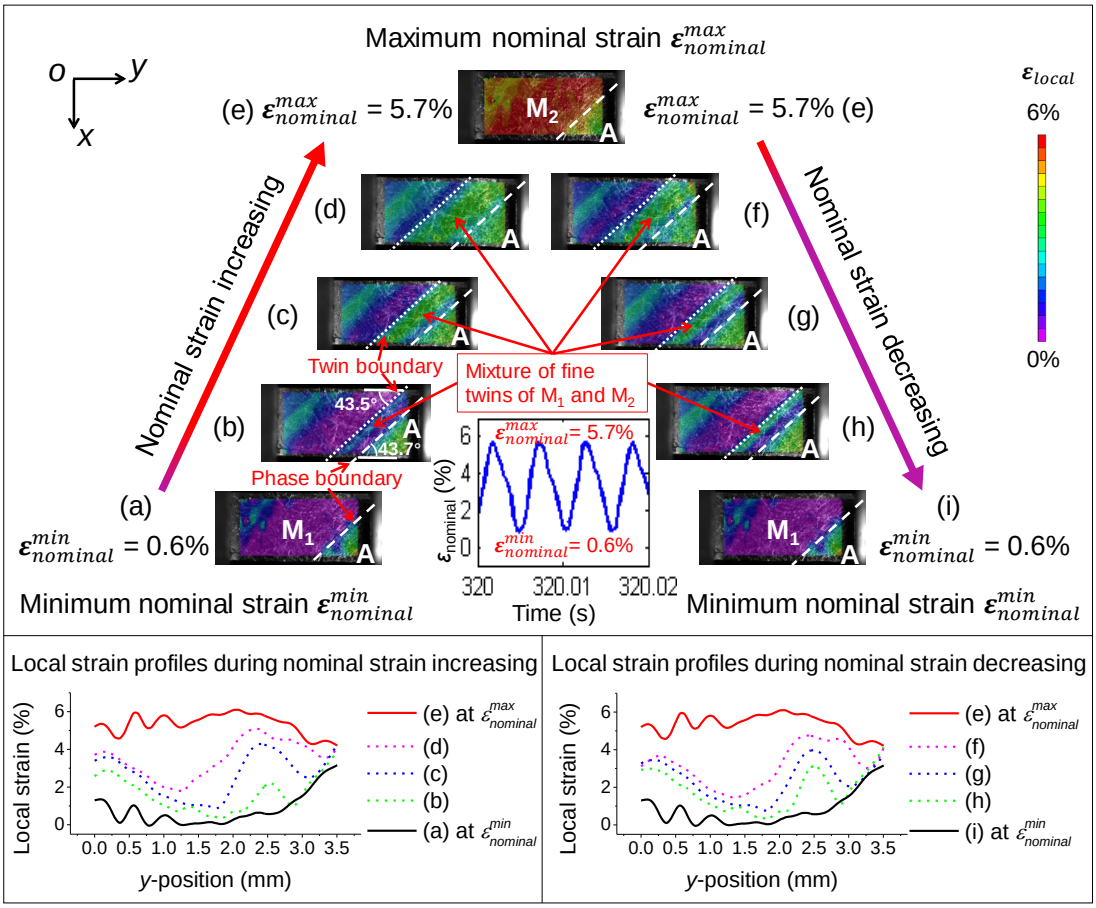

Figure 4.3 DIC local strain evolutions in a typical cycle of the martensite reorientation process with the existence of the non-active A-phase (the green region of A-phase (at lower right corner in each DIC map) has a constant local strain around 4%) at the time slot t_6.

coexistence of the temperature-driven phase-boundary motion (phase transformation) and the magnetic-field-driven twin-boundary motion (martensite reorientation) is possible by controlling the external magnetic field and the ambient airflow simultaneously. This new phenomenon poses some critical questions in theoretical understanding:

(1) As the M-to-A phase transformation is triggered by the temperature rise, it is normally expected that the stable working temperature during the coexistence

of the field-induced martensite reorientation and the temperature-induced phase transformation should be close to A_s and A_f. However, both the previous study (Zhang et al., 2018b) and the current experiment (Fig. 4.1(a)) show that the stable working temperature is around M_s and M_f. It is noted that the measured temperature at a single point in the current test can only roughly describe the global temperature evolution of the specimen. To reveal the local temperature distribution (particularly near the twin/phase boundaries) during the actuation, precise full-field temperature measurement and delicate dynamic modeling are needed.

(2) The cyclic local strain evolutions (Figs. 4.2 and 4.3) show that the non-active A-zone (A-phase with constant deformation) can be compatible with the active M-zone (with cyclic deformation and varying fractions of martensite variants). Such compatibility is not expected because normally the A-phase (cubic phase) can only be compatible with martensite (tetragonal phase) twins of some specified variant fractions which satisfy the energy minimization, i.e., A-phase cannot be compatible with a single martensite variant or martensite twins with continuously changing fractions (Bhattacharya, 2003; Seiner et al., 2011; Stupkiewicz et al., 2007). To solve this inconsistency, some compatibility analyses are performed in the following section.

4.4 Compatibility analysis and discussions

Here, the compatibility analysis is focused on the twin boundary and the A-M interface (phase boundary), i.e., the coherent interfaces between the cubic austenite phase and the tetragonal martensite variants. Strictly speaking, the 10M martensite phase of the

ferromagnetic shape memory alloy Ni-Mn-Ga are slightly monoclinic: its characteristic angle $\gamma = 90.37°$ is not exactly equal to 90° of a tetragonal lattice (Chulist et al., 2013; Heczko et al., 2013; Sozinov et al., 2011; Straka et al., 2011b). To simplify the analysis, the austenite-to-10M martensite transition in Ni-Mn-Ga is approximated by a cubic-to-tetragonal transition. Three tetragonal martensite variants (M_1, M_2 and M_3 with short axis c along y, x and z directions respectively) can be formed and their corresponding Bain matrices (Bhattacharya, 2003) are:

$$\mathbf{U}_1 = \begin{pmatrix} \alpha & 0 & 0 \\ 0 & \beta & 0 \\ 0 & 0 & \alpha \end{pmatrix}, \quad \mathbf{U}_2 = \begin{pmatrix} \beta & 0 & 0 \\ 0 & \alpha & 0 \\ 0 & 0 & \alpha \end{pmatrix}, \quad \mathbf{U}_3 = \begin{pmatrix} \alpha & 0 & 0 \\ 0 & \alpha & 0 \\ 0 & 0 & \beta \end{pmatrix}. \tag{4.1}$$

where $\alpha = \dfrac{a}{a_0} = 1.0188$ and $\beta = \dfrac{c}{a_0} = 0.9606$ for the material (where a_0, a and c are the lattice parameters).

Firstly, we check the formation of the compatible twin boundaries among the three variants: M_1, M_2 and M_3. The kinematic compatibility condition between two unstressed, but possibly rotated, martensite variants can be formulated into a twinning equation (Bhattacharya, 2003):

$$\mathbf{R}\mathbf{U}_I - \mathbf{U}_J = \boldsymbol{a} \otimes \boldsymbol{n}, \tag{4.2}$$

where $\mathbf{U}_I$ and $\mathbf{U}_J$ are the Bain matrices of the I^{th} and the J^{th} martensite variants; R belonging to a 3D rotation group ($SO(3)$) represents the rotation of the variant $\mathbf{U}_I$ with respect to the variant $\mathbf{U}_J$ when the twin is formed; $\boldsymbol{a} \otimes \boldsymbol{n}$ is a dyadic product of a non-zero vector $\boldsymbol{a}$ and a unit vector $\boldsymbol{n}$; the vector $\boldsymbol{n}$ represents the normal of the twinning plane

in the reference cubic coordinate system while the vector $\boldsymbol{a}$ is the so-called shearing vector.

Following the standard solving method (Bhattacharya, 2003), the solution to the twinning equation Eq. (4.2) with the Bain matrices in Eq. (4.1) can be found. There are three types of twins: (1) the twin boundaries (planes) between the variant-pair M_1:M_2 have the normal vector $\boldsymbol{n} = [\pm 1, \ \pm 1, \ 0]$, cutting the x-y plane (the experimentally observed specimen surface) by an angle 45° as shown in Fig. 4.4, where the observed surface in x-y plane is highlighted in light blue and dark blue schematically representing the two variants observed in the surface; (2) the twin boundaries between the variant-pair M_2:M_3 have the normal vector $\boldsymbol{n} = [\pm 1, \ 0, \ \pm 1]$, cutting the x-y plane with a horizontal line (Fig. 4.4); (3) the twin boundaries between the variant-pair M_1:M_3 have the normal vector $\boldsymbol{n} = [0, \ \pm 1, \ \pm 1]$, cutting the x-y plane with a vertical line (Fig. 4.4).

Based on the comparison between the above theoretically predicted twin boundaries (Fig. 4.4) and the experimentally observed twin boundary in Fig. 4.2 whose twin plane cuts the x-y plane (the observed specimen surface) by the angle 44.7°, it is easy to confirm that the martensite reorientation under the magnetic field (along x-direction) and the compressive force (along y-direction) in the dynamic tests (Fig. 2.1) is the cyclic transition between the variant-pair M_1:M_2.

Then, we check whether the twin (M_1:M_2) can be compatible with the cubic A-phase via the habit plane equation for the austenite-martensite (A-M) interface (Bhattacharya, 2003):

$$\mathbf{R}'(f\mathbf{R}\mathbf{U}_I + (1-f)\mathbf{U}_J) - \mathbf{I} = \boldsymbol{b} \otimes \boldsymbol{m}, \tag{4.3}$$

where $\mathbf{I}$ is an identity second-order tensor representing the Bain matrix of the A-phase;

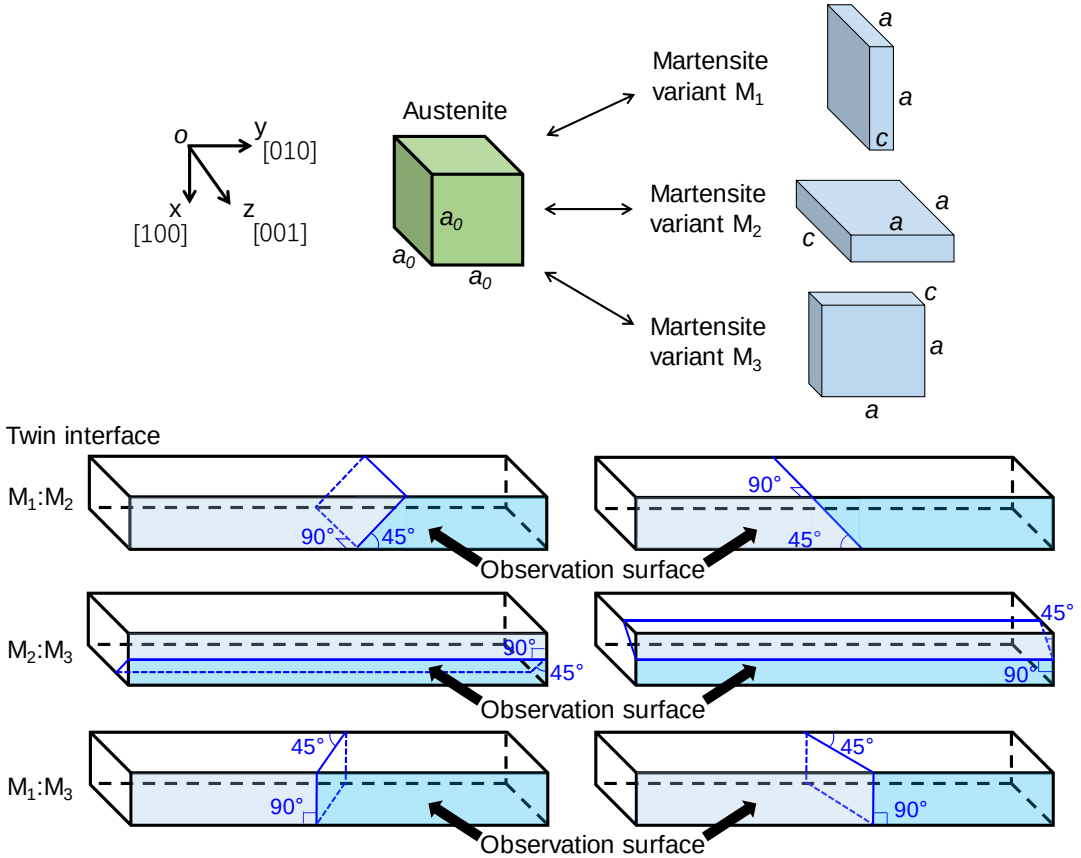

Figure 4.4 Twin boundaries of the tetragonal martensite variants of Ni-Mn-Ga. The x-y plane (the experimentally observed surface) is shown in color in each 3D schematic, where different colors represent different variants.

$\boldsymbol{m}$ is the normal of the A-M interface while the vector $\boldsymbol{b}$ is the shear vector; $\mathbf{R'}$ represents the rotation of the martensite twin (consisting of the I^{th} and the J^{th} martensite variants) with respect to the A-phase; f and $1-f$ are the fractions of the I^{th} and the J^{th} martensite variants in the twin, respectively. Equation (4.3) represents the kinematic compatibility between undeformed austenite and a martensite twin.

Solving Eq. (4.3) with the twin M_1:M_2, we can obtain the normal of the compatible A-M interface (the vector $\boldsymbol{m}$) and the corresponding volume fraction f of variant M_1 in

the twin as listed in Table 4.1. The normal of the compatible A-M interface has several possibilities for the material:

$$\boldsymbol{m}^{\pm} = \frac{1}{1.4518}[\pm 1.0519,\ \pm 0.0367,\ 1],\ \text{ or }\ \boldsymbol{m}^{\pm} = \frac{1}{1.4518}[\pm 0.0367,\ \pm 1.0519,\ 1]. \tag{4.4}$$

It is seen from Eq. (4.4) that one of the absolute values of the components of the normal is 0.0367, which is much smaller than those of the other two components (1.0519 and 1), and the two components (1.0519 and 1) are very close to each other. So, the orientation of the A-M interface can be approximated as

$$\boldsymbol{m} = (1/\sqrt{2})[\pm 1,\ 0,\ 1],\ \text{ or }\ \boldsymbol{m}^{\pm} = (1/\sqrt{2})[0,\ \pm 1,\ 1]. \tag{4.5}$$

The A-M interface with the normal $\boldsymbol{m}$ in Eq. (4.5) can cut the x-y plane (the experimentally observed surface) by a horizontal line or a vertical line, depending on the volume fraction f as shown in Figs. 4.5(a) and 4.5(b). Such theoretical prediction doesn't agree with the experimental observation in Fig. 4.1(b) where the A-M interface cuts the x-y plane by an angle close to 45°.

In order to find out the reason for this inconsistency, we also solve the habit-plane equation (Eq. (4.3)) between A-phase and other kinds of twins to determine other possible A-M interfaces, i.e., the compatible interface between A-phase and other martensite twins such as the twins M_1:M_3 and M_2:M_3. Following the similar solving procedures, all the possible A-M interfaces are determined and listed in Table 4.2, and the corresponding traces in the observed surface (i.e., the intersection line of the A-M interface in the x-y plane) are shown in Figs. 4.5(a) ~ 4.5(f). It is seen that the traces of the A-M interfaces in Figs. 4.5(d) and 4.5(f) have the angle 45°. So the twin

Martensite variant-pair	f (fraction of M_1)	$\boldsymbol{n}$ (normal of fine-twins)	$\boldsymbol{m}$ (normal of A-M interface)
M_1:M_2	0.32	[1 1 0]	1/1.4518 [-1.0519 0.0367 1]
			1/1.4518 [1.0519 -0.0367 1]
		[-1 1 0]	1/1.4518 [1.0519 0.0367 1]
			1/1.4518 [-1.0519 -0.0367 1]
	0.68	[1 1 0]	1/1.4518 [0.0367 -1.0519 1]
			1/1.4518 [-0.0367 1.0519 1]
		[-1 1 0]	1/1.4518 [0.0367 1.0519 1]
			1/1.4518 [-0.0367 -1.0519 1]

Table 4.1 Theoretical prediction on the compatible interfaces between the austenite phase and the martensite twins M_1:M_2.

M_1:M_3 (with the fixed volume fractions 68% : 32%) and the twin M_2:M_3 (with the fixed volume fractions 68% : 32%) can have a compatible A-M interface with the trace in x-y plane agreeing with the experimental observation (of 45° angle).

Combining the calculations above and the observations in the experiments, we can conjecture that the interface between the active M-zone (M-phase of the cyclic switching between variants M_1 and M_2) and the non-active A-zone (A-phase) is not a simple sharp interface, but a transitional layer containing the twins M_1:M_3 or M_2:M_3. The situations about the transitional layer at the interfacial zone were studied in the literature to explain the coexistence of different phases; for example, some needle twin structures have been observed in similar materials (Cu-Al-Ni and Ni-Al) (Boullay et al.,

Martensite variant-pair M_I:M_J	f (fraction of M_I)	$\boldsymbol{n}$ (normal of fine-twin)	$\boldsymbol{m}$ (normal of A-M interface)	Trace of A-M interface (on observation surface)
M_1:M_2	32%	[1 1 0]	$1/\sqrt{2}$ [$\pm$1 0 1]	horizontal (Fig. 4.5(a))
		[-1 1 0]	$1/\sqrt{2}$ [$\pm$1 0 1]	
	68%	[1 1 0]	$1/\sqrt{2}$ [0 $\pm$1 1]	vertical (Fig. 4.5(b))
		[-1 1 0]	$1/\sqrt{2}$ [0 $\pm$1 1]	
M_1:M_3	32%	[0 1 1]	$1/\sqrt{2}$ [1 0 $\pm$1]	horizontal (Fig. 4.5(c))
		[0 -1 1]	$1/\sqrt{2}$ [1 0 $\pm$1]	
	68%	[0 1 1]	$1/\sqrt{2}$ [1 $\pm$1 0]	45° (Fig. 4.5(d))
		[0 -1 1]	$1/\sqrt{2}$ [1 $\pm$1 0]	
M_2:M_3	32%	[1 0 1]	$1/\sqrt{2}$ [0 1 $\pm$1]	vertical (Fig. 4.5(e))
		[1 0 -1]	$1/\sqrt{2}$ [0 1 $\pm$1]	
	68%	[1 0 1]	$1/\sqrt{2}$ [$\pm$1 1 0]	45° (Fig. 4.5(f))
		[1 0 -1]	$1/\sqrt{2}$ [$\pm$1 1 0]	

Table 4.2 Theoretical prediction on the compatible interfaces between the austenite phase and the martensite twins, whose schematic microstructure patterns are given in Fig. 4.5.

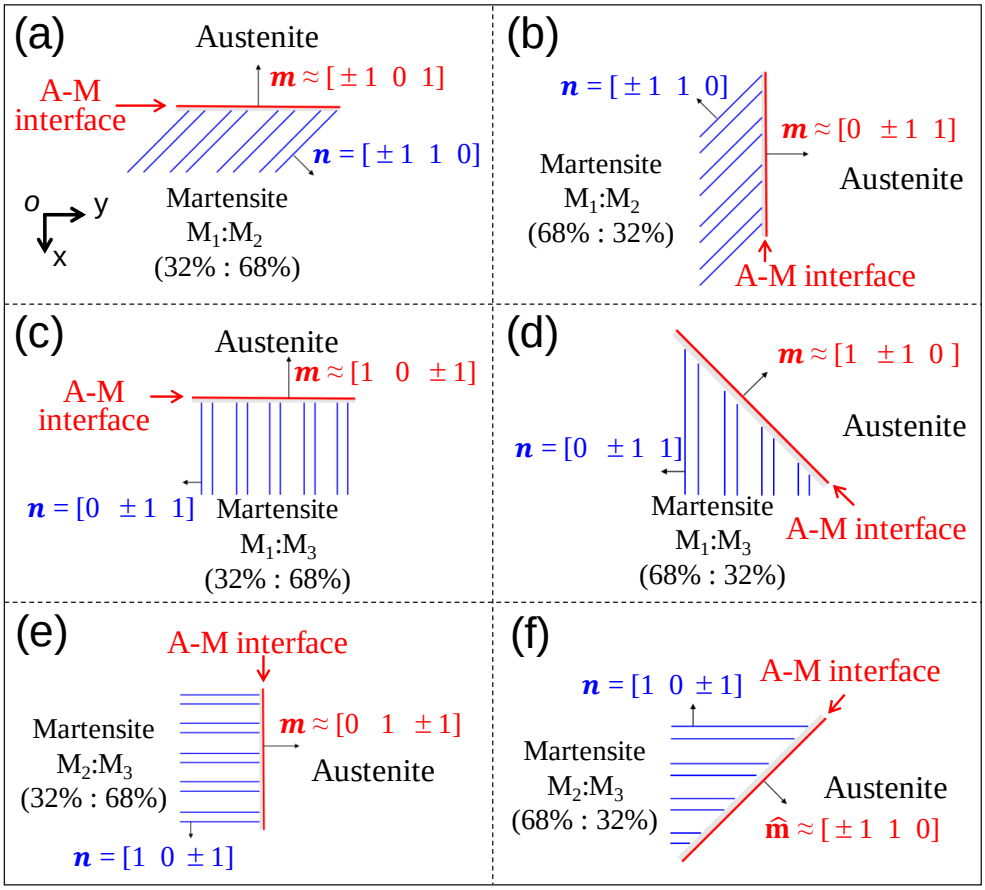

Figure 4.5 Theoretical predictions of all the possible patterns of A-M interface and martensite fine-twins (projections on x-y plane). The patterns in (a) and (b) are formed by fine twins of M_1:M_2, (c) and (d) are formed by fine twins of M_1:M_3, (e) and (f) are formed by fine twins of M_2:M_3.

2001; Chu, 1993; James et al., 1995; Li, 2001; Schryvers et al., 2002; Seiner et al., 2011; Zárubová et al., 2010), where the gradually tapering needle twins are reported to serve as a compatible transition layer between A-phase and M-phase (no matter single variant state or twinned martensite). Inspired by such needle twin microstructure, the compatible interfacial zone between the active M-zone and the non-active A-zone can be schematically drawn in Fig. 4.6(a) ~ (c), where Fig. 4.6(a) shows the 3D schematic and Fig. 4.6(b) and 4.6(c) show the unfolded views of the possible horizontal and

vertical needle twin structures of the martensite variant M_3, respectively.

In order to clarify the microstructure of the interfacial zone in the current specimen (details of the interfacial zone cannot be resolved in the high-frequency actuation due to the limited resolution), we performed a simple test: by quasi-static mechanical compressions along y and x directions, we created twins consisting M_1 and M_2 in the specimen (with the same orientation as that in the dynamic case of the high-frequency magneto-mechanical loading); then, a hot airflow was forced to pass through the specimen to increase the specimen temperature, and an optical microscope with a polarized light (Olympus AX70) was used to observe the specimen surface (x-y plane) as shown in Fig. 4.6(d) where there is a horizontal needle zone (the interfacial zone) separating the martensite zone (45° twins between M_1 and M_2) from the A-phase, which is similar to the previously reported needle patterns observed in Cu-Al-Ni and Ni-Al (Boullay et al., 2001; Chu, 1993; James et al., 1995; Li, 2001; Schryvers et al., 2002; Seiner et al., 2011; Zárubová et al., 2010). Moreover, it is noted that the A-M interface is parallel to the twin boundaries at the observed specimen surface in Fig. 4.6(d), which is consistent with that in the dynamic experiment as shown in Fig. 4.3. Therefore, the experimentally observed compatible A-M interface in the dynamic experiment in Fig. 4.3 can be due to the occurrence of the transition needles of the variant M_3 (horizontal needles in Fig. 4.6(b) or vertical ones in Fig. 4.6(c)). It means, to reach the compatibility between austenite and martensite zones, the third martensite variant M_3 must be nucleated besides the original martensite variants M_1 and M_2 taking part in the cyclic martensite reorientation during the dynamic loading. Further higher resolution observation on the fine twin structures at the interfacial zone may help better understand the dynamic behaviors.

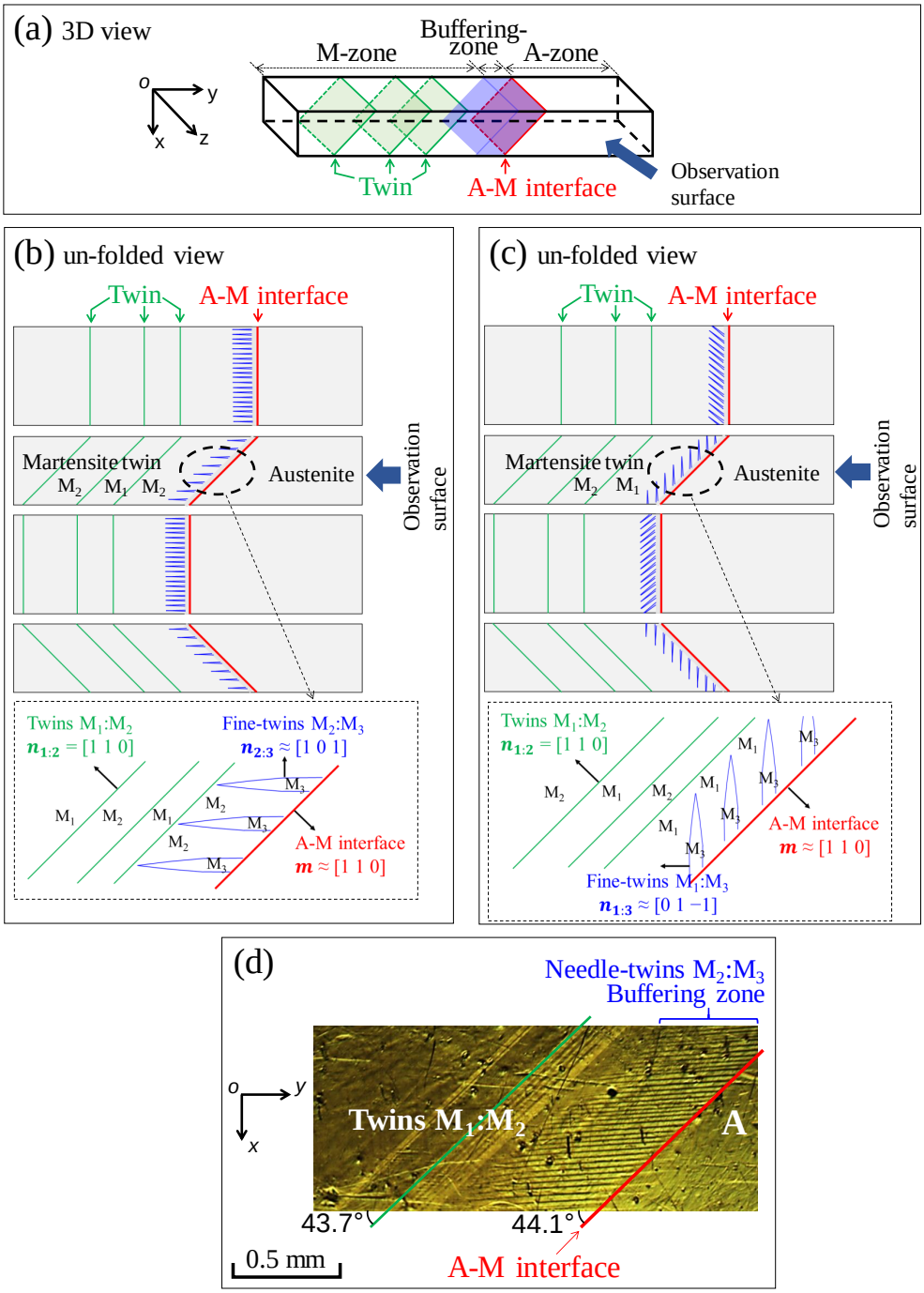

Figure 4.6 The 3D and unfolded schematics and of the compatible microstructures with the coexistence of non-active austenite zone, buffering needle zone and active martensite zone in (a) ~ (c); (d) The optical observation of the needle fine-twins jointly generated with A-M interface in a quasi-static thermo-mechanical test.

Based on the experimental observations and the theoretical analyses, the physical mechanism of the tunable strain amplitude of FSMA by changing heat-exchange can be understood as follows. For cases with A-zone in the specimen (such as schematically shown in Fig. 4.7(a) to 4.7(c)), under cyclic magneto-mechanical loading: A-zone has no reversible strain (local strain keeps constant at around 4%); M-zone has 6% strain amplitude (MR between M_1 and M_2); while the buffering zone is constrained (by the compatibilities with A-M interfaces at one side and martensite variants M_1 and M_2 at the other side) to have a transition strain between austenite and active martensite. In the still air (weak heat-exchange), when the austenite band is nucleated by temperature rise, the left martensite band can be freely driven to martensite reorientation by high-frequency magneto-mechanical loading, while the A-phase is non-active (as shown in Fig. 4.7(a)). The fraction of martensite phase in the specimen determines the output strain, thus determines the heat-generation rate, which should be balanced with the heat-transfer rate. On the other hand, the heat-transfer rate is governed by the heat-exchange efficiency. For a system at steady state (with steady output strain and steady temperature at around phase transformation temperatures) with coexistence of A-M two phases (such as in Fig. 4.7(a)), when the heat-transfer rate is increased by increasing the heat-exchange efficiency (as in Fig. 4.7(b) and 4.7(c)), the specimen temperature will first start to decrease because the heat-transfer rate is larger than the heat-generation rate. It should be noted that the A-M phase fractions of single crystal material is very sensitive to the temperature change (100% phase transformation can be completed within a very small temperature range ($M_s - M_f = 1°\mathrm{C}$)) when the specimen temperature is in the range of phase transformation temperatures. So when the specimen temperature starts to decrease slightly due to the increasing heat-exchange, a large fraction of material will transform from A- to M-phase (through A-M phase boundary motion, comparing Fig.

4.7(a), 4.7(b) and 4.7(c)), which induces more M-phase can be driven to perform cyclic MR and increases the heat generation rate. So the heat generation can compensate the heat transfer induced by the increasing heat-exchange, to restrain the decreasing specimen temperature. The fractions of M-phase will increase until the heat balance is reached between the heat transfer and the heat generation, where the system reaches the steady state of the working temperature and the output strain amplitude (the fraction of martensite). This self-organization mechanism makes the FSMA-actuator like a smart temperature self-compensation control system. The fractions of M-phase will keep increasing with increasing heat-exchange efficiency (airflow velocity) until all the A-phase has been transformed to M-phase (100% M-phase as shown in Fig. 4.7(d)).

In summary, when the temperature-induced phase transformation occurs during the high-frequency field-induced martensite reorientation, the specimen is divided into three zones as schematically shown in Fig. 4.7(a): the non-active austenite zone (A-zone with the constant local strain), the active martensite zone (M-zone of the cyclic switching between the variants M_1 and M_2) and the buffering needle zone (interfacial zone) with the fine transition needles of the variant M_3 which helps maintain the compatibility between A-zone with constant deformation and M-zone with cyclic martensite reorientation during the dynamic loading. When the ambient airflow increases, the non-active A-zone shrinks and the active M-zone expands through the propagation of the A-M phase boundary (see Figs. 4.7(a) ~ 4.7(c)); if the airflow is strong enough to keep the specimen temperature lower than the phase-transformation temperature, the specimen would be fully occupied by the active martensite zone and the output strain reach maximum value (around 6% in current system).

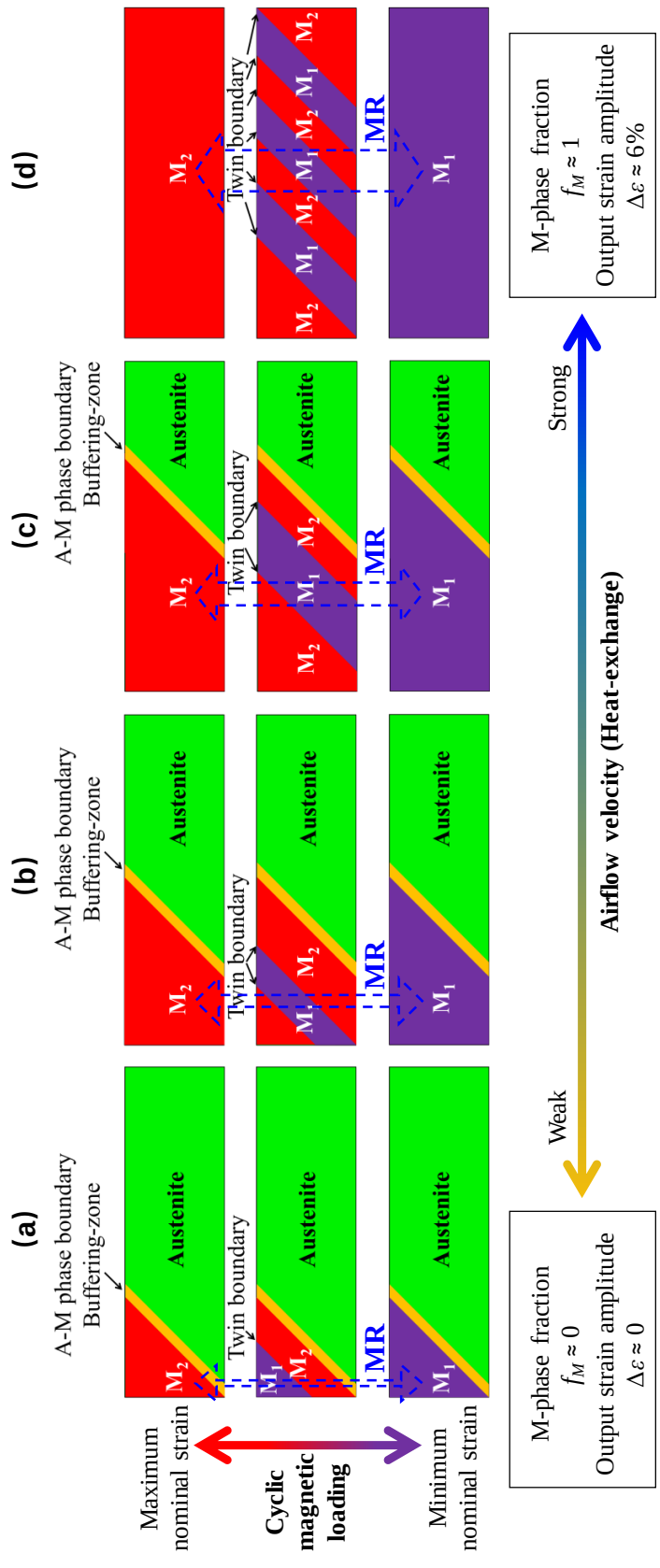

Figure 4.7 Schematic of the martensite reorientation (with twin boundary motion) between M_1 and M_2 driven by cyclic magneto-mechanical loading (see the vertical evolution, marked by vertical dashed double-headed arrows) and the phase transformation (with A-M phase boundary motion) driven by changing heat-exchange efficiency (see the horizontal evolution from (a) to (d)). The buffering-zone can be compatible with both the austenite phase and martensite phase (no matter single variant or twins of M_1 and M_2).

4.5 Summary and conclusions

In this chapter, we report a test of the high-frequency magnetic-field-induced martensite reorientation in Ni-Mn-Ga ferromagnetic shape memory alloy under stepped changing ambient airflows with the in-situ optical observation on the specimen surface, from which the local strain evolution (DIC strain maps) and the associated transformation/reorientation among the various phases/variants in the thermo-magneto-mechanical situations are demonstrated. It is shown that the high-frequency frictional martensite reorientation causes a significant temperature rise leading to the temperature-induced Martensite-to-Austenite phase transformation; i.e., some part of the specimen becomes austenite phase which doesn't contribute any cyclic deformation in current low-level magnetic loading so that the global field-induced deformation is significantly reduced. Increasing heat transfer to ambient by controlling the ambient airflow is demonstrated to be an effective way to reduce the influence of the austenite phase: the volume size of austenite phase reduces with increasing the ambient airflow. That presents a novel mechanism: the temperature-induced phase transformation (phase boundary motion) and the field-induced martensite reorientation (twin boundary motion) coexist in the magnetic actuation with changing ambient airflow, as the specimen needs to self-organize the different phases/variants to satisfy all the thermo-magneto-mechanical boundary conditions. The self-organized microstructure of the different phases/variants can be understood by compatibility analysis. The main conclusions can be drawn:

(1) The coexistence of the temperature-induced phase transformation and the field-induced martensite reorientation divides the specimen into three zones: the **non-active Austenite zone** (A-zone, not sensitive to the applied low-level magnetic field), the

active Martensite zone (M-zone, taking cyclic martensite reorientation to provide strain oscillation) and the **buffering zone** (the interfacial zone with needle twins between the A- and M-zones). To be compatible with both the active zone and the non-active zone, the interfacial zone might need the needle twin structure formation composed of the third martensite variant which doesn't participate in the martensite reorientation; i.e., some martensite variant doesn't exist originally in the field-induced deformation can be generated due to the requirement of the compatibility between the active martensite zone and the non-active austenite zone.

(2) By controlling the ambient heat-transfer efficiency (changing ambient airflow velocity), the volume fractions of the active martensite zone and non-active austenite zone in the specimen under the low-level magnetic field loading can be self-organized to maintain the heat balance. Therefore, the global output strain amplitude can be significantly tuned (from $\sim 1\%$ to $\sim 6\%$ in the current study) while the working temperature keeps almost constant at the material characteristic phase-transformation temperature M_s and M_f.

Chapter 5

Conclusions and perspectives

5.1 Conclusions

In this thesis, we performed systematically multi-scale experimental and theoretical investigations on the high-frequency magnetic field-induced martensite reorientation of Ferromagnetic Shape Memory Alloy (FSMA) Ni-Mn-Ga single crystal. The experiments were conducted at various levels of the magnetic field frequency, the initial compressive stress and the ambient airflow velocity. In-situ Digital Image Correlation (DIC) method was used to observe the local strain evolution during the high-frequency deformation driven by the cyclic magnetic field. Combining the experimental observations and theoretical analysis, the physical mechanism of the high-frequency nominal responses at different conditions were well understood and the critical conditions to achieve large stable strain oscillation amplitudes in dynamic actuation were derived. The important conclusions of the thesis can be drawn as follows:

(1) Energy dissipation due to the frictional twin boundary motion in the high-frequency martensite reorientation can cause significant temperature rise of the FSMA specimen. When the temperature increases to the characteristic phase transformation temperature, the Martensite-to-Austenite phase transformation will take place in the FSMA material, which makes the output strain amplitude suddenly decrease to a much lower level. Therefore, the large strain amplitude of FSMA without a steady-state temperature lower than the phase-transformation temperature is at the risk of instability (strain drop) during the long-time actuation.

(2) The stable strain amplitude and the stable temperature of FSMA can be controlled by the ambient heat-exchange efficiency. The stable strain amplitude depends on the heat-exchange efficiency non-monotonically. With the decrease of the heat-exchange efficiency, the strain amplitude first increases due to the temperature-dependence of the effective twinning stress and then decreases due to the temperature-induced phase transformation which disturbs the magnetic-field-induced martensite reorientation. The maximum stable strain amplitude is obtained at the critical heat-relaxation time t_h^* which makes the stable temperature close to (but lower than) the phase-transformation temperature.

(3) The temperature-induced phase transformation at weak heat-exchange efficiency divides the specimen into three zones: the **non-active Austenite zone** (A-zone, insensitive to the applied low-level magnetic field), the **active Martensite zone** (M-zone, taking cyclic martensite reorientation to provide strain oscillation) and the **buffering zone** (the interfacial zone with needle twins between the A- and M-zones). To be compatible with both the active zone and the non-active zone, the interfacial zone needs the needle twin structure formation composed by the third

martensite variant which doesn't participate in the martensite reorientation; i.e., the martensite variant doesn't exist originally in the field-induced deformation can be generated due to the requirement of the compatibility between the active Martensite zone and the non-active Austenite zone.

(4) By controlling the ambient heat-transfer efficiency, the volume fractions of the active Martensite zone and non-active Austenite zone in the specimen can be self-organized to maintain the heat balance and thus the nominal output strain can be changed (which is governed by the varying martensite fraction). That presents a novel mechanism in FSMA: the magnetic field-driven twin boundary motion and the temperature-driven phase boundary motion can be activated and compatible at the same time in the magnetic actuation with changing heat-exchange efficiency, as the specimen need to self-organize the different phases/variants to satisfy all the thermo-magneto-mechanical boundary conditions.

(5) A special "isothermal" FSMA actuator with tunable output strain can be designed by taking advantage of the interaction between the temperature-induced phase transformation and the magnetic-field-induced martensite reorientation. The output strain amplitude of this actuator changes monotonically with the ambient heat-exchange efficiency due to the balance between the heat generated from the martensite reorientation of the untransformed martensite region (related to the strain amplitude) and the heat transferred to the ambient (related to the airflow velocity), while its working temperature is almost constant (close to the phase-transformation temperature M_s and M_f) and independent of the strain amplitude.

5.2 Perspectives

Various phenomena have been revealed by the systematic experiments in this work. While the main results have been analyzed in this thesis, some phenomena still lack deep understanding and their underlying physical mechanisms are not yet revealed. For example, the frequency dependences of output strain amplitude and twinning stress of FSMA are shown experimentally, but the microscopic mechanism still needs to be further investigated. In-situ observations with higher resolution are required in the future work to discover the relation between the actuation frequency and the nucleation/propagation of the twin boundaries (Type I and Type II). Moreover, for the cases with working temperature lower than the phase transformation temperatures (without phase transformation), the temperature effect on the output strain amplitude is primarily attributed to the temperature dependence of the effective twinning stress, but more experimental and theoretical understandings are required to further clarify the relation between the temperature-dependent output strain and the temperature-dependent twining/detwining process. In addition, the phenomenon discovered in Chapter 3 that, the FSMA can have two "meta-stable" states during the magnetic actuation, poses a challenging problem for applications of FSMA-actuator and needs further investigations.

On the other hand, it is noted that the commercialization of Ni-Mn-Ga single crystal based FSMA-actuator is still limited by some of its material properties (such as brittleness) and high costs of synthesis. Therefore, better FSMA materials and structures should be developed, possibly by changing alloy compositions and/or improving the synthesis methods. Moreover, 3D printing of FSMA materials with delicate and/or programmable properties and structures is a new topic in this field; both experimental and

theoretical approaches on the design and the optimization of the multi-scale structures of these FSMA materials will be an interesting and challenging issue.

Bibliography

Aaltio, I., Lahelin, M., Söderberg, O., Heczko, O., Löfgren, B., Ge, Y., Seppälä, J., and Hannula, S.-P. (2008). Temperature dependence of the damping properties of Ni-Mn-Ga alloys. *Materials Science and Engineering: A*, 481:314–317.

Adachi, Y., Ogi, Y., Kobayashi, N., Hayasaka, Y., Kanomata, T., Umetsu, R. Y., Xu, X., and Kainuma, R. (2017). Temperature dependences of the electrical resistivity on the heusler alloy system $Ni_2MnGa_{1-x}Fe_x$. *Metals*, 7(10):413.

Arndt, M., Griebel, M., Novák, V., Roubíček, T., and Šittner, P. (2006). Martensitic transformation in NiMnGa single crystals: Numerical simulation and experiments. *International Journal of Plasticity*, 22(10):1943–1961.

Asua, E., García-Arribas, A., Etxebarria, V., and Feuchtwanger, J. (2014). Pulsed-mode operation and performance of a ferromagnetic shape memory alloy actuator. *Smart Materials and Structures*, 23(2):025023.

Auricchio, F., Bonetti, E., Scalet, G., and Ubertini, F. (2014). Theoretical and numerical modeling of shape memory alloys accounting for multiple phase transformations and martensite reorientation. *International Journal of Plasticity*, 59:30–54.

Basaran, B. (2009). *Magnetic Field-Induced Phase Transformation and Power Harvesting Capabilities in Magnetic Shape Memory Alloys*. PhD thesis, Texas A&M University, USA.

Basso, V. (2011). The magnetocaloric effect at the first-order magneto-elastic phase transition. *Journal of Physics: Condensed Matter*, 23(22):226004.

Bhattacharya, K. (2003). *Microstructure of martensite: why it forms and how it gives rise to the shape-memory effect*. Oxford University Press.

Blanter, M. S., Golovinm, I. S., Neuhauser, H., and Sinning, H. R. (2007). *Internal friction in metallic materials : a handbook*. Springer, Berlin Heidelberg.

Boullay, P., Schryvers, D., and Kohn, R. (2001). Bending martensite needles in $Ni_{65}Al_{35}$ investigated by two-dimensional elasticity and high-resolution transmission electron microscopy. *Physical Review B*, 64(14):144105.

Brinson, L. C., Schmidt, I., and Lammering, R. (2004). Stress-induced transformation behavior of a polycrystalline NiTi shape memory alloy: micro and macromechanical investigations via in situ optical microscopy. *Journal of the Mechanics and Physics of Solids*, 52(7):1549–1571.

Bruno, N., Wang, S., Karaman, I., and Chumlyakov, Y. (2017). Reversible martensitic transformation under low magnetic fields in magnetic shape memory alloys. *Scientific reports*, 7:40434.

Bruno, O., Leo, P., and Reitich, F. (1995). Free boundary conditions at austenite-martensite interfaces. *Physical review letters*, 74(5):746.

Chen, X., He, Y., and Moumni, Z. (2013a). Twin boundary motion in NiMnGa single crystals under biaxial compression. *Materials Letters*, 90:72–75.

Chen, X., Moumni, Z., He, Y., and Zhang, W. (2014). A three-dimensional model of magneto-mechanical behaviors of martensite reorientation in ferromagnetic shape memory alloys. *Journal of the Mechanics and Physics of Solids*, 64:249–286.

Chen, X., Srivastava, V., Dabade, V., and James, R. D. (2013b). Study of the cofactor conditions: conditions of supercompatibility between phases. *Journal of the Mechanics and Physics of Solids*, 61(12):2566–2587.

Chmielus, M., Chernenko, V. A., Knowlton, W. B., Kostorz, G., and Müllner, P. (2008). Training, constraints, and high-cycle magneto-mechanical properties of Ni-Mn-Ga magnetic shape-memory alloys. *The European Physical Journal Special Topics*, 158(1):79–85.

Chmielus, M., Glavatskyy, I., Hoffmann, J.-U., Chernenko, V. A., Schneider, R., and Müllner, P. (2011). Influence of constraints and twinning stress on magnetic field-induced strain of magnetic shape-memory alloys. *Scripta Materialia*, 64(9):888–891.

Chu, C.-H. (1993). *Hysteresis and microstructures : a study of biaxial loading on compound twins of copper-aluminum-nickel single crystals*. PhD thesis, University of Minnesota, USA.

Chulist, R., Böhm, A., Oertel, C. G., and Skrotzki, W. (2014). Self-accommodation in polycrystalline 10M Ni-Mn-Ga martensite. *Journal of Materials Science*, 49(11):3951–3955.

Chulist, R., Straka, L., Lanska, N., Soroka, A., Sozinov, A., and Skrotzki, W. (2013). Characterization of mobile type I and type II twin boundaries in 10M modulated Ni-Mn-Ga martensite by electron backscatter diffraction. *Acta Materialia*, 61(6):1913–1920.

Cisse, C., Zaki, W., and Zineb, T. B. (2016). A review of constitutive models and modeling techniques for shape memory alloys. *International Journal of Plasticity*, 76:244–284.

Cui, Y., Li, Y., Wang, Z., Lei, Q., Koizumi, Y., and Chiba, A. (2017). Regulating twin boundary mobility by annealing in magnesium and its alloys. *International Journal of Plasticity*, 99:1–18.

Dai, Y., Hou, L., Fautrelle, Y., Li, Z., Esling, C., Ren, Z., and Li, X. (2018). Detwinning process of martensite in $Ni_{58}Mn_25Ga_{17}$ as a high temperature shape memory alloy under uniaxial compression. *International Journal of Plasticity*, 103:203–213.

Faran, E., Riccardi, L., and Shilo, D. (2017). Inertia-controlled twinning in Ni-Mn-Ga actuators: A discrete twin-boundary dynamics study. *Shape Memory and Superelasticity*, 3(3):206–217.

Faran, E. and Shilo, D. (2016). A discrete twin-boundary approach for simulating the magneto-mechanical response of Ni-Mn-Ga. *Smart Materials and Structures*, 25(9):095020.

Franco, V. and Conde, A. (2012). Magnetic refrigerants with continuous phase transitions: Amorphous and nanostructured materials. *Scripta Materialia*, 67(6):594–599.

Fukuda, T., Yamamoto, M., Yamaguchi, T., and Kakeshita, T. (2014). Magnetocrystalline anisotropy and magnetic field-induced strain of three martensites in Fe_3Pt ferromagnetic shape memory alloys. *Acta Materialia*, 62(1):182–187.

Gabdullin, N. and Khan, S. (2015). Review of properties of magnetic shape memory (MSM) alloys and MSM actuator designs. In *Journal of Physics: Conference Series*, volume 588, page 012052. IOP Publishing.

Gaitzsch, U., Pötschke, M., Roth, S., Rellinghaus, B., and Schultz, L. (2007). Mechanical training of polycrystalline 7M $Ni_{50}Mn_{30}Ga_{20}$ magnetic shape memory alloy. *Scripta Materialia*, 57(6):493–495.

Glavatska, N., Mogylny, G., Glavatskiy, I., and Gavriljuk, V. (2002). Temperature stability of martensite and magnetic field induced strain in Ni-Mn-Ga. *Scripta Materialia*, 46(8):605–610.

Haldar, K., Lagoudas, D. C., and Karaman, I. (2014). Magnetic field-induced martensitic phase transformation in magnetic shape memory alloys: modeling and experiments. *Journal of the Mechanics and Physics of Solids*, 69:33–66.

He, Y. and Sun, Q. (2010). Rate-dependent domain spacing in a stretched NiTi strip. *International Journal of Solids and Structures*, 47(20):2775–2783.

He, Y., Yin, H., Zhou, R., and Sun, Q. (2010). Ambient effect on damping peak of NiTi shape memory alloy. *Materials Letters*, 64(13):1483–1486.

He, Y. J., Chen, X., and Moumni, Z. (2011). Two-dimensional analysis to improve the output stress in ferromagnetic shape memory alloys. *Journal of Applied Physics*, 110(6):063905.

He, Y. J., Chen, X., and Moumni, Z. (2012). Reversible-strain criteria of ferromagnetic shape memory alloys under cyclic 3D magneto-mechanical loadings. *Journal of Applied Physics*, 112(3):033902.

He, Y. J. and Sun, Q. (2011). On non-monotonic rate dependence of stress hysteresis of superelastic shape memory alloy bars. *International Journal of Solids and Structures*, 48(11-12):1688–1695.

Heczko, O., Cejpek, P., Drahokoupil, J., and Holỳ, V. (2016). Structure and microstructure of Ni-Mn-Ga single crystal exhibiting magnetic shape memory effect analysed by high resolution X-ray diffraction. *Acta Materialia*, 115:250–258.

Heczko, O., Lanska, N., Soderberg, O., and Ullakko, K. (2002). Temperature variation of structure and magnetic properties of Ni-Mn-Ga magnetic shape memory alloys. *Journal of magnetism and magnetic materials*, 242:1446–1449.

Heczko, O., Seiner, H., Stoklasová, P., Sedlák, P., Sermeus, J., Glorieux, C., Backen, A., Fähler, S., and Landa, M. (2017). Temperature dependence of elastic properties in austenite and martensite of Ni-Mn-Ga epitaxial films. *Acta Materialia*.

Heczko, O., Sozinov, A., and Ullakko, K. (2000). Giant field-induced reversible strain in magnetic shape memory nimnga alloy. *IEEE Transactions on Magnetics*, 36(5):3266–3268.

Heczko, O. and Straka, L. (2003). Temperature dependence and temperature limits of magnetic shape memory effect. *Journal of Applied Physics*, 94(11):7139–7143.

Heczko, O. and Straka, L. (2004). Compositional dependence of structure, magnetization and magnetic anisotropy in Ni-Mn-Ga magnetic shape memory alloys. *Journal of Magnetism and Magnetic Materials*, 272:2045–2046.

Heczko, O., Straka, L., and Seiner, H. (2013). Different microstructures of mobile twin boundaries in 10M modulated Ni-Mn-Ga martensite. *Acta Materialia*, 61(2):622–631.

Henry, C., Bono, D., Feuchtwanger, J., Allen, S., and O'Handley, R. (2002). AC field-induced actuation of single crystal Ni-Mn-Ga. *Journal of Applied Physics*, 91(10):7810–7811.

Henry, C. P. (2002). *Dynamic actuation properties of Ni-Mn-Ga ferromagnetic shape memory alloys*. PhD thesis, Massachusetts Institute of Technology.

Hobza, A., Patrick, C. L., Ullakko, K., Rafla, N., Lindquist, P., and Müllner, P. (2018). Sensing strain with Ni-Mn-Ga. *Sensors and Actuators A: Physical*, 269:137–144.

Huang, Y. J., Hu, Q. D., Bruno, N., Karaman, I., and Li, J. G. (2014). Influence of grain boundary on pseudoelasticity in highly-oriented polycrystalline $Ni_{52}Fe_{17}Ga_{27}Co_4$ ferromagnetic shape memory alloy. *Materials Letters*, 114:11–14.

Iadicola, M. A. and Shaw, J. A. (2004). Rate and thermal sensitivities of unstable transformation behavior in a shape memory alloy. *International Journal of Plasticity*, 20(4-5):577–605.

James, R. D., Kohn, R. V., and Shield, T. (1995). Modeling of branched needle microstructures at the edge of a martensite laminate. *Le Journal de Physique IV*, 5(C8):C8–253.

James, R. D. and Wuttig, M. (1998). Magnetostriction of martensite. *Philosophical Magazine A*, 77(5):1273–1299.

Jugo, J., Feuchtwanger, J., Corres, J., and Etxebarria, V. (2018). Analysis of temperature effects in high accuracy Ferromagnetic Shape Memory Alloy actuators. *Sensors and Actuators A: Physical*.

Kainuma, R., Imano, Y., Ito, W., Sutou, Y., Morito, H., Okamoto, S., Kitakami, O., Oikawa, K., Fujita, A., Kanomata, T., et al. (2006). Magnetic-field-induced shape recovery by reverse phase transformation. *Nature*, 439(7079):957.

Karaca, H. E., Karaman, I., Basaran, B., Chumlyakov, Y. I., and Maier, H. (2006). Magnetic field and stress induced martensite reorientation in nimnga ferromagnetic shape memory alloy single crystals. *Acta materialia*, 54(1):233–245.

Karaca, H. E., Karaman, I., Basaran, B., Lagoudas, D., Chumlyakov, Y. I., and Maier, H. (2007). On the stress-assisted magnetic-field-induced phase transformation in Ni_2MnGa ferromagnetic shape memory alloys. *Acta materialia*, 55(13):4253–4269.

Karaca, H. E., Karaman, I., Basaran, B., Ren, Y., Chumlyakov, Y. I., and Maier, H. J. (2009). Magnetic field-induced phase transformation in NiMnCoIn magnetic shape-memory alloys—a new actuation mechanism with large work output. *Advanced Functional Materials*, 19(7):983–998.

Kiefer, B. and Lagoudas, D. C. (2004). Phenomenological modeling of ferromagnetic shape memory alloys. In *Smart Structures and Materials 2004: Active Materials: Behavior and Mechanics*, volume 5387, pages 164–177. International Society for Optics and Photonics.

Kiefer, B. and Lagoudas, D. C. (2005). Modeling of the magnetic field-induced martensitic variant reorientation and the associated magnetic shape memory effect in MSMAs. In *Smart Structures and Materials 2005: Active Materials: Behavior and Mechanics*, volume 5761, pages 454–466. International Society for Optics and Photonics.

Lai, Y. W. (2009). *Magnetic Microstructure and Actuation Dynamics of NiMnGa Magnetic Shape Memory Materials*. PhD thesis, Technische Universität Dresden, Germany.

Lai, Y.-W., Schäfer, R., Schultz, L., and McCord, J. (2008). Direct observation of AC field-induced twin-boundary dynamics in bulk NiMnGa. *Acta Materialia*, 56(18):5130–5137.

Lawrence, T., Lindquist, P., Ullakko, K., and Müllner, P. (2016). Fatigue life and fracture mechanics of unconstrained Ni-Mn-Ga single crystals in a rotating magnetic field. *Materials Science and Engineering A*, 654:221–227.

Li, Z. (2001). Computations of needle-like microstructures. *Applied numerical mathematics*, 39(1):1–15.

Li, Z., Yang, B., Zou, N., Zhang, Y., Esling, C., Gan, W., Zhao, X., and Zuo, L. (2017). Crystallographic characterization on polycrystalline Ni-Mn-Ga alloys with strong preferred orientation. *Materials*, 10(5):1–20.

Li, Z., Zhang, Y., Sánchez-Valdés, C., Sánchez Llamazares, J., Esling, C., Zhao, X., and Zuo, L. (2014). Giant magnetocaloric effect in melt-spun Ni-Mn-Ga ribbons with magneto-multistructural transformation. *Applied Physics Letters*, 104(4):044101.

Liu, Y., Karaman, I., Wang, H., and Zhang, X. (2014). Two types of martensitic phase transformations in magnetic shape memory alloys by in-situ nanoindentation studies. *Advanced Materials*, 26(23):3893–3898.

Liu, Y. and Xie, Z. (2003). Twinning and detwinning of <0 1 1> type II twin in shape memory alloy. *Acta materialia*, 51(18):5529–5543.

Liu, Y., Zhang, X., Liu, J., Xing, D., Shen, H., Chen, D., and Sun, J. (2015). Superelasticity in polycrystalline Ni-Mn-Ga-Fe microwires fabricated by melt-extraction. *Materials Research*, 18:61–65.

Majewska, K., Żak, A., and Ostachowicz, W. (2010). Vibration control of a rotor by magnetic shape memory actuators—an experimental work. *Smart Materials and Structures*, 19(8):085004.

Martynov, V. and Kokorin, V. (1992). The crystal structure of thermally-and stress-induced martensites in Ni_2MnGa single crystals. *Journal de Physique III*, 2(5):739–749.

Molnar, P., Sittner, P., Lukas, P., Hannula, S., and Heczko, O. (2008). Stress-induced martensite variant reorientation in magnetic shape memory Ni-Mn-Ga single crystal studied by neutron diffraction. *Smart Materials and Structures*, 17(3):035014.

Morito, H., Fujita, A., Fukamichi, K., Kainuma, R., Ishida, K., and Oikawa, K. (2002). Magnetocrystalline anisotropy in single-crystal Co-Ni-Al ferromagnetic shape-memory alloy. *Applied Physics Letters*, 81(9):1657–1659.

Morito, H., Oikawa, K., Fujita, A., Fukamichi, K., Kainuma, R., and Ishida, K. (2009). Stress-assisted large magnetic-field-induced strain in single-variant Co-Ni-Ga ferromagnetic shape memory alloy. *Journal of Physics: Condensed Matter*, 21(25):256002.

Morito, H., Oikawa, K., Fujita, A., Fukamichi, K., Kainuma, R., and Ishida, K. (2010). Large magnetic-field-induced strain in Co-Ni-Al single-variant ferromagnetic shape memory alloy. *Scripta Materialia*, 63(4):379–382.

Murray, S. J., Marioni, M., Allen, S., O'handley, R., and Lograsso, T. A. (2000). 6% magnetic-field-induced strain by twin-boundary motion in ferromagnetic Ni-Mn-Ga. *Applied Physics Letters*, 77(6):886–888.

Neudert, A., Lai, Y. W., Schäfer, R., Kustov, M., Schultz, L., and McCord, J. (2012). Magnetic domains and twin boundary movement of NiMnGa magnetic shape memory crystals. *Advanced Engineering Materials*, 14(8):601–613.

Oikawa, K., Wulff, L., Iijima, T., Gejima, F., Ohmori, T., Fujita, A., Fukamichi, K., Kainuma, R., and Ishida, K. (2001). Promising ferromagnetic Ni-Co-Al shape memory alloy system. *Applied Physics Letters*, 79(20):3290–3292.

Okamoto, N., Fukuda, T., and Kakeshita, T. (2008). Temperature dependence of rearrangement of martensite variants by magnetic field in 10m, 14m and 2m martensites of Ni-Mn-Ga alloys. *Materials Science and Engineering: A*, 481:306–309.

Otsuka, K. and Wayman, C. M. (1999). *Shape memory materials*. Cambridge university press.

O'Handley, R. C., Murray, S., Marioni, M., Nembach, H., and Allen, S. (2000). Phenomenology of giant magnetic-field-induced strain in ferromagnetic shape-memory materials. *Journal of Applied Physics*, 87(9):4712–4717.

Pagounis, E., Chulist, R., Szczerba, M., and Laufenberg, M. (2014). Over 7% magnetic field-induced strain in a Ni-Mn-Ga five-layered martensite. *Applied Physics Letters*, 105(5):052405.

Pascan, O.-Z. (2015). *Dynamic behaviors of Ferromagnetic Shape Memory Alloys*. PhD thesis, ENSTA-ParisTech, France.

Pascan, O.-Z., He, Y., Moumni, Z., and Zhang, W. (2015). Temperature rise of high-frequency martensite reorientation via Type II twin boundary motion in NiMnGa ferromagnetic shape memory alloy. *Scripta Materialia*, 104:71–74.

Pascan, O.-Z., He, Y., Moumni, Z., and Zhang, W. (2016). High-frequency performance of ferromagnetic shape memory alloys. *Annals of Solid and Structural Mechanics*, 8(1-2):17–25.

Pinneker, V., Gueltig, M., Sozinov, A., and Kohl, M. (2014). Single phase boundary actuation of a ferromagnetic shape memory foil. *Acta Materialia*, 64:179–187.

Pinneker, V., Yin, R., Eberl, C., Sozinov, A., Ezer, Y., and Kohl, M. (2013). Evolution of local strain bands of different orientation in single crystalline Ni-Mn-Ga foils under tension. *Journal of Alloys and Compounds*, 577:S358–S361.

Qian, M., Zhang, X., Witherspoon, C., Sun, J., and Müllner, P. (2013). Superelasticity and shape memory effects in polycrystalline Ni-Mn-Ga microwires. *Journal of Alloys and Compounds*, 577:S296–S299.

Qu, Y., Cong, D., Sun, X., Nie, Z., Gui, W., Li, R., Ren, Y., and Wang, Y. (2017). Giant and reversible room-temperature magnetocaloric effect in Ti-doped Ni-Co-Mn-Sn magnetic shape memory alloys. *Acta Materialia*, 134:236–248.

Rogovoy, A. and Stolbova, O. (2016). Modeling the magnetic field control of phase transition in ferromagnetic shape memory alloys. *International Journal of Plasticity*, 85:130–155.

Sakamoto, T., Fukuda, T., Kakeshita, T., Takeuchi, T., and Kishio, K. (2003). Magnetic field-induced strain in iron-based ferromagnetic shape memory alloys. *Journal of Applied Physics*, 93(10):8647–8649.

Sarawate, N. and Dapino, M. (2006). Experimental characterization of the sensor effect in ferromagnetic shape memory Ni-Mn-Ga. *Applied Physics Letters*, 88(12):121923.

Sarawate, N. and Dapino, M. (2008). Frequency dependent strain-field hysteresis model for ferromagnetic shape memory Ni-Mn-Ga. *IEEE Transactions on Magnetics*, 44(5):566–575.

Saren, A., Musiienko, D., Smith, A., Tellinen, J., and Ullakko, K. (2015). Modeling and design of a vibration energy harvester using the magnetic shape memory effect. *Smart Materials and Structures*, 24(9):095002.

Sayyaadi, H. and Farsangi, M. A. A. (2015). Frequency-dependent energy harvesting via magnetic shape memory alloys. *Smart Materials and Structures*, 24(11):115022.

Schryvers, D., Boullay, P., Potapov, P. L., Kohn, R. V., and Ball, J. M. (2002). Microstructures and interfaces in Ni-Al martensite: comparing HRTEM observations with continuum theories. *International journal of solids and structures*, 39(13-14):3543–3554.

Sehitoglu, H., Wang, J., and Maier, H. (2012). Transformation and slip behavior of Ni_2FeGa. *International Journal of Plasticity*, 39:61–74.

Seiner, H., Glatz, O., and Landa, M. (2011). A finite element analysis of the morphology of the twinned-to-detwinned interface observed in microstructure of the Cu-Al-Ni shape memory alloy. *International Journal of Solids and Structures*, 48(13):2005–2014.

Shaw, J. A. and Kyriakides, S. (1995). Thermomechanical aspects of NiTi. *Journal of the Mechanics and Physics of Solids*, 43(8):1243–1281.

Singh, S., D'Souza, S., Mukherjee, K., Kushwaha, P., Barman, S., Agarwal, S., Mukhopadhyay, P., Chakrabarti, A., and Sampathkumaran, E. (2014). Magnetic properties and magnetocaloric effect in Pt doped Ni-Mn-Ga. *Applied Physics Letters*, 104(23):231909.

Smith, A. R., Tellinen, J., and Ullakko, K. (2014). Rapid actuation and response of Ni-Mn-Ga to magnetic-field-induced stress. *Acta Materialia*, 80:373–379.

Sokolovskiy, V., Grünebohm, A., Buchelnikov, V., and Entel, P. (2014). Ab initio and monte carlo approaches for the magnetocaloric effect in Co- and In-doped Ni-Mn-Ga Heusler alloys. *Entropy*, 16(9):4992–5019.

Song, Y., Chen, X., Dabade, V., Shield, T. W., and James, R. D. (2013). Enhanced reversibility and unusual microstructure of a phase-transforming material. *Nature*, 502(7469):85.

Soroka, A., Sozinov, A., Lanska, N., Rameš, M., Straka, L., and Ullakko, K. (2018). Composition and temperature dependence of twinning stress in non-modulated martensite of Ni-Mn-Ga-Co-Cu magnetic shape memory alloys. *Scripta Materialia*, 144:52–55.

Sozinov, A., Lanska, N., Soroka, A., and Straka, L. (2011). Highly mobile type II twin boundary in Ni-Mn-Ga five-layered martensite. *Applied Physics Letters*, 99(12):124103.

Sozinov, A., Soroka, A., Lanska, N., Rameš, M., Straka, L., and Ullakko, K. (2017). Temperature dependence of twinning and magnetic stresses in $Ni_{46}Mn_{24}Ga_{22}Co_4Cu_4$ alloy with giant 12% magnetic field-induced strain. *Scripta Materialia*, 131:33–36.

Stephan, J. M., Pagounis, E., Laufenberg, M., Paul, O., and Ruther, P. (2011). A novel concept for strain sensing based on the ferromagnetic shape memory alloy nimnga. *IEEE Sensors Journal*, 11(11):2683–2689.

Straka, L., Drahokoupil, J., Pacherová, O., Fabiánová, K., Kopeckỳ, V., Seiner, H., Hänninen, H., and Heczko, O. (2015). The relation between lattice parameters and very low twinning stress in $Ni_{50}Mn_{25+x}Ga_{25-x}$ magnetic shape memory alloys. *Smart Materials and Structures*, 25(2):025001.

Straka, L., Hänninen, H., and Heczko, O. (2011a). Temperature dependence of single twin boundary motion in Ni-Mn-Ga martensite. *Applied Physics Letters*, 98(14):141902.

Straka, L., Heczko, O., and Hannula, S.-P. (2006). Temperature dependence of reversible field-induced strain in Ni-Mn-Ga single crystal. *Scripta Materialia*, 54(8):1497–1500.

Straka, L., Heczko, O., Seiner, H., Lanska, N., Drahokoupil, J., Soroka, A., Fähler, S., Hänninen, H., and Sozinov, A. (2011b). Highly mobile twinned interface in 10 m modulated Ni-Mn-Ga martensite: Analysis beyond the tetragonal approximation of lattice. *Acta Materialia*, 59(20):7450–7463.

Straka, L., Soroka, A., Seiner, H., Hänninen, H., and Sozinov, A. (2012). Temperature dependence of twinning stress of Type I and Type II twins in 10m modulated Ni-Mn-Ga martensite. *Scripta materialia*, 67(1):25–28.

Stupkiewicz, S., Maciejewski, G., and Petryk, H. (2007). Low-energy morphology of the interface layer between austenite and twinned martensite. *Acta Materialia*, 55(18):6292–6306.

Sutou, Y., Imano, Y., Koeda, N., Omori, T., Kainuma, R., Ishida, K., and Oikawa, K. (2004). Magnetic and martensitic transformations of NiMnX (X= In, Sn, Sb) ferromagnetic shape memory alloys. *Applied Physics Letters*, 85(19):4358–4360.

Tan, H. and Elahinia, M. (2008). A nonlinear model for ferromagnetic shape memory alloy actuators. *Communications in Nonlinear Science and Numerical Simulation*, 13(9):1917–1928.

Techapiesancharoenkij, R., Kostamo, J., Allen, S. M., and O'Handley, R. C. (2011). The effect of magnetic stress and stiffness modulus on resonant characteristics of Ni-Mn-Ga ferromagnetic shape memory alloy actuators. *Journal of Magnetism and Magnetic Materials*, 323(23):3109–3116.

Techapiesancharoenkij, R., Kostamo, J., Allen, S. M., and O'Handley, R. C. (2009). Frequency response of acoustic-assisted Ni-Mn-Ga ferromagnetic-shape-memory-alloy actuator. *Journal of Applied Physics*, 105(9):093923.

Ullakko, K., Huang, J. K., Kantner, C., O'Handley, R. C., and Kokorin, V. V. (1996). Large magnetic-field-induced strains in Ni_2MnGa single crystals. *Applied Physics Letters*, 69(13):1966–1968.

Vronka, M., Seiner, H., and Heczko, O. (2017). Temperature dependence of twinning stress–analogy between Cu-Ni-Al and Ni-Mn-Ga shape memory single crystals. *Philosophical Magazine*, 97(18):1479–1497.

Webster, P., Ziebeck, K., Town, S., and Peak, M. (1984). Magnetic order and phase transformation in Ni_2MnGa. *Philosophical Magazine B*, 49(3):295–310.

Wuttig, M., Li, J., and Craciunescu, C. (2001). A new ferromagnetic shape memory alloy system. *Scripta materialia*, 44(10):2393–2397.

Xia, M. and Sun, Q. (2015). Jump phenomena of rotational angle and temperature of NiTi wire in nonlinear torsional vibration. *International Journal of Solids and Structures*, 56:220–234.

Xia, M. and Sun, Q. (2017). Thermomechanical responses of nonlinear torsional vibration with NiTi shape memory alloy–alternative stable states and their jumps. *Journal of the Mechanics and Physics of Solids*, 102:257–276.

Yin, R., Wendler, F., Krevet, B., and Kohl, M. (2016). A magnetic shape memory microactuator with intrinsic position sensing. *Sensors and Actuators A: Physical*, 246:48–57.

Yu, C., Kang, G., Song, D., and Kan, Q. (2015). Effect of martensite reorientation and reorientation-induced plasticity on multiaxial transformation ratchetting of super-elastic NiTi shape memory alloy: new consideration in constitutive model. *International Journal of Plasticity*, 67:69–101.

Zárubová, N., Gemperlová, J., Gemperle, A., Dlabáček, Z., Šittner, P., and Novák, V. (2010). In situ TEM observation of stress-induced martensitic transformations and twinning processes in CuAlNi single crystals. *Acta Materialia*, 58(15):5109–5119.

Zhang, S., Chen, X., Moumni, Z., and He, Y. (2018a). Coexistence and compatibility of martensite reorientation and phase transformation in high-frequency magnetic-field-induced deformation of Ni-Mn-Ga single crystal. *International Journal of Plasticity*, Accpeted.

Zhang, S., Chen, X., Moumni, Z., and He, Y. (2018b). Thermal effects on high-frequency magnetic-field-induced martensite reorientation in ferromagnetic shape memory alloys: An experimental and theoretical investigation. *International Journal of Plasticity*, Accpeted.

Zhao, D., Liu, J., Chen, X., Sun, W., Li, Y., Zhang, M., Shao, Y., Zhang, H., and Yan, A. (2017). Giant caloric effect of low-hysteresis metamagnetic shape memory alloys with exceptional cyclic functionality. *Acta Materialia*, 133:217–223.

Zou, N., Li, Z., Zhang, Y., Yang, B., Zhao, X., Esling, C., and Zuo, L. (2018). Plastic deformation of Ni-Mn-Ga 7M modulated martensite by twinning & detwinning and intermartensitic transformation. *International Journal of Plasticity*, 100:1–13.

Zreihan, N., Faran, E., and Shilo, D. (2015). The effects of temperature on the lattice barrier for twin wall motion. *Applied Physics Letters*, 107(4):041605.

Titre : Analyse de la réponse dynamique à haute fréquence des matériaux à mémoire de forme magnétiques

Mots clés : alliage à mémoire de forme ferromagnétique, déformation à haute fréquence, réorientation de la martensite induite par un champ magnétique, transformation de phase induite par la température, compatibilité de la microstructure, couplage thermo-magnéto-mécanique.

Résumé : Dans cette thèse, des analyses expérimentales et théoriques multi-échelles des performances des FSMAs soumis à un champ magnétique de longue durée et à haute fréquence sont réalisées. Tout d'abord, des expériences systématiques d'actionnement magnétique de longue durée (> 100 secondes) sur une éprouvette en monocristal Ni-Mn-Ga sont effectuées à différents niveaux de la fréquence du champ magnétique, de la contrainte de compression initiale et du flux d'air ambiant (échange de chaleur) afin d'étudier leur influence sur la réponse des FSMAs. Par ailleurs, un modèle unidimensionnel de transfert de chaleur a été est développé permettant d'interpréter les nouveaux phénomènes liés aux effets thermiques mises en lumière expérimentalement. Ainsi, les conditions nécessaires à l'obtention d'une réponse dynamique stable ont été déduites. De plus, afin de comprendre la dépendance de la déformation nominale induite par le champ magnétique par rapport aux échanges thermiques à partir d'une analyse microscopique, la distribution/évolution de la déformation locale ainsi que la transformation/réorientation associée parmi les différentes phases/variantes au cours de l'actionnement à haute fréquence sous divers conditions d'échange de chaleur sont analysées via des observations in-situ à l'aide la corrélation d'images numériques (DIC). Un nouveau mécanisme est ainsi révélé : le mouvement des interphases induit par la variation de température (transformation de phase) et le mouvement des variantes de martensite induit par le champ magnétique (réorientation de martensite) peuvent être activés simultanément, sous l'actionnement magnéto-thermique-mécanique dans la mesure où le matériau peut auto-organiser les fractions volumiques des différentes phases/variantes afin de satisfaire toutes les conditions aux limites thermo-magnéto-mécaniques. En outre, la morphologie des bandes de déformations et des différentes phases/variantes auto-organisées est révélée et expliquée à l'échelle microscopique à l'aide des conditions de compatibilité géométrique.

Title: High frequency magnetic field-induced strain of ferromagnetic shape memory alloys

Keywords: ferromagnetic shape memory alloy, high-frequency strain, magnetic field-induced martensite reorientation, temperature-induced phase transformation, microstructure compatibility, thermo-magneto-mechanical coupling.

Abstract: In this thesis, multi-scale experimental and theoretical analyses of the long-time performance of FSMA under high-frequency magnetic actuation are performed. Systematic experiments of the long-time magnetic actuation (> 100 seconds) on a Ni-Mn-Ga single crystal bar are conducted at various levels of magnetic field frequency, initial compressive stress and ambient airflow (ambient heat-exchange efficiency) to investigate their influences on the stable state of the high-frequency FSMA-actuator. A one-dimensional heat-transfer model is developed and the new experimental phenomena of the thermal effects are well understood. Based on the experimental results and theoretical analysis, critical conditions to achieve the large and stable output strain amplitude in the high-frequency actuation are derived. Moreover, to understand the heat-exchange dependence of the output nominal-strain from a microscopic view, the local strain distribution/evolution and the associated transformation/reorientation among the different phases/variants during the high-frequency actuation under various heat-exchange efficiencies are demonstrated via the in-situ Digital Image Correlation observations. A novel mechanism is revealed: the temperature-driven phase boundary motion (phase transformation) and the magnetic field-driven twin boundary motion (martensite reorientation) can be activated at the same time under the magneto-thermal-mechanical actuation as the material can self-organize its volume fractions of the different phases/variants to satisfy all the thermo-magneto-mechanical boundary conditions. Further, the self-organized morphology/pattern composed of various variants and phases during cyclic deformation (with the moving habit plane and twin boundaries) can be explained by microstructure compatibility analyses.

Université Paris-Saclay
Espace Technologique / Immeuble Discovery
Route de l'Orme aux Merisiers RD 128 / 91190 Saint-Aubin, France